A PROCESS DESIGN FOR THE PURIFICATION OF CARBON CONTAMINATED WITH CU-BI ALLOY FROM CATALYTIC METHANE DECOMPOSITION

BY

DANA RAQUEL PITTMAN

THESIS

Submitted in partial fulfillment of the requirements

for the degree of Master of Science in Chemical Engineering

in the Faculty of Graduate Studies of

Lakehead University

August 2025

Thunder Bay, Ontario, Canada

Advisor:

Dr. Lionel Catalan, PhD, PEng

ABSTRACT

Low-carbon hydrogen production by catalytic methane decomposition ($CH_4 \rightarrow H_{2(g)} + C_{(s)}$) has demonstrated potential to significantly decarbonize industrial sectors. Previous research has proposed carrying out the reaction in a liquid metal bubble reactor containing catalytic molten metal alloys such as $Cu_{0.45}Bi_{0.55}$ to allow hydrogen bubbles to exit through the top while the solid carbon product floats to the top of the melt to be skimmed or removed by other mechanical means. Metal lost in the process of carbon removal can impact the plant profitability because it will need to be continually replenished. Additionally, metal contaminants in the carbon product pose limitations on its ability to be sold as carbon black, and on its ability to be stored permanently due to the risk of metal contaminants in the environment. In this work, the process design methodology for the purification of carbon contaminated with copper and bismuth from catalytic methane decomposition is presented along with the capital costs of carbon processing equipment. Bismuth has a relatively high vapour pressure, so it is removed by vacuum distillation. A mass transfer model is applied to a lift-spray apparatus wherein the molten mixture of copper, bismuth, and carbon is sprayed up through a riser into a vacuum chamber where the bismuth vapours can be condensed and recovered. The spray creates smaller droplets which help increase the amount of surface area available for bismuth to evaporate. Copper is removed by leaching in a sulfuric acid solution by $Cu_{(s)} + 2H^+ + 0.5O_2 \rightarrow Cu^{2+} + H_2O$. The carbon product is then filtered and rinsed from the leaching solution before being dried in a rotary dryer. Copper is precipitated from the filtrate solution using scrap iron, a metal higher in the electromotive series, in a process called cementation. Copper particles can be filtered from the solution and then sold as lower grade copper due to some iron contamination in the copper. The final carbon product is 98.9 wt% carbon on a dry basis, which meets the specifications for rubber-grade carbon black. The cost of carbon processing equipment per tonne of hydrogen produced is estimated at \$257/tonne H_2, a value that is relatively small compared to the market price of hydrogen which ranges from \$1500-8000 USD/tonne H_2. This work creates a pathway to recover metal catalyst lost in the process of carbon removal from methane decomposition in a liquid metal bubble reactor. The purified carbon product can be sold on the carbon black market or safely stored underground.

ACKNOWLEDGEMENTS

I am sincerely grateful to my thesis advisor, Dr. Lionel Catalan, for his dedicated mentorship throughout this process. You have provided me with every opportunity for my academic and professional growth. As I move into the next stage of my journey, I am inspired to extend the same generosity and guidance to others that you have so kindly shown to me.

I am also very thankful to my thesis committee members Dr. Ebrahim Rezaei and Dr. Francisco Ramos-Pallares for their insightful comments and suggestions, and to Dr. Jan Nesset and Dr. Phillip Mackey for sharing their expertise in mineral processing and metallurgy.

TABLE OF CONTENTS

LIST OF TABLES

LIST OF FIGURES

1. Introduction

1.1.Hydrogen Production and the Need for Lower Carbon Alternatives

As the global commitment to net-zero emissions intensifies, interest in low-emissions hydrogen is gaining momentum. Low-emissions hydrogen is the key to decarbonizing sectors such as heavy industry, shipping, and aviation where emissions are hard to abate and alternative options are limited (International Energy Agency, 2024). Innovation in low-emissions hydrogen is critical to ensure market uptake by developing technologies with lower equipment costs and improved efficiency.

Low-emissions hydrogen production technologies are categorized in the 2024 Global Hydrogen Review by their level of technology readiness from lowest to highest by small prototype, large prototype, demonstration, market uptake, and mature (International Energy Agency, 2024). Currently, low-emissions hydrogen from electrolysis using proton exchange membrane (PEM) and alkaline electrolysers are ranked the highest due to their uptake in the market. However, innovation is still required to minimise the use of expensive platinum group metal components in catalysts (International Energy Agency, 2024). Solid oxide electrolysers (SOEC's) achieve the highest efficiency among electrolyser designs but require an external heat source for steam generation and have a limited lifetime of around 2 years (International Energy Agency, 2024). Innovation in other low-emissions hydrogen production technologies could bring them up from lower levels of technology readiness up to market uptake, thus increasing their competitiveness with electrolysis for investment.

Catalytic methane pyrolysis recently moved up from the Large Prototype stage to the Demonstration stage due to progress made in the last year (International Energy Agency, 2024). In January 2024, Hazer announced the startup of its commercial demonstration plant using thermo-catalytic pyrolysis to produce 100 tpa of Hydrogen in Australia (International Energy Agency, 2024). In September 2024 Hycamite

opened a thermo-catalytic methane pyrolysis demonstration plant in Finland with a capacity of 2000 tpa H_2 (International Energy Agency, 2024). Beyond that, methane pyrolysis using plasma has just breached the stage of Market Uptake (International Energy Agency, 2024). This work focuses on the continued innovation of methane pyrolysis by catalytic decomposition, an important step in increasing its technology readiness for market uptake.

1.2. Conventional Hydrogen Production

Conventionally, hydrogen is produced by the steam methane reforming reaction (SMR, Eq 1) combined with the water gas shift reaction (WGS, Eq 2). Overall, the SMR + WGS reaction (Eq 3) releases one mole of CO_2 per mole of CH_4 consumed.

$$CH_4 + H_2O \leftrightarrow 3H_2 + CO \qquad \Delta H^{\circ}_{298} = 205.81 \text{ kJ/mol} \qquad \text{Eq 1}$$

$$CO + H_2O \leftrightarrow H_2 + CO_2 \qquad \Delta H^{\circ}_{298} = -41.17 \text{ kJ/mol} \qquad \text{Eq 2}$$

$$CH_4 + 2H_2O \leftrightarrow 4H_2 + CO_2 \qquad \Delta H^{\circ}_{298} = 164.65 \text{ kJ/mol} \qquad \text{Eq 3}$$

SMR + WGS typically takes place in the catalyst-packed tubes of a reforming furnace. Additional CO_2 is produced when natural gas is burned to supply heat to the reaction. As a result, conventional hydrogen production has a relatively large carbon footprint. CO_2 emissions can be mitigated by the use of carbon capture, utilization, and storage where CO_2 from flue gas is captured and sequestered underground or utilized elsewhere (Rostrup-Nielsen & Christiansen, 2011).

1.3. Methane Pyrolysis

Methane pyrolysis, or methane decomposition, occurs when a methane molecule is thermally cracked into hydrogen gas and solid carbon by:

$$CH_{4(g)} \rightarrow 2H_{2(g)} + C_{(s)} \qquad \Delta H^{\circ}_{298} = 75 \text{ kJ/mol} \qquad \text{Eq 4}$$

In comparison to the SMR + WGS reaction, no CO2 is directly produced. Instead, a solid carbon coproduct is produced. If clean energy is used to supply heat to the reaction, then the hydrogen can be produced with very little carbon footprint. Sources of indirect emissions include the natural gas supply chain and those associated with electricity generation, depending on the technology choice (Catalan et al., 2023; Parkinson et al., 2018).

1.4. Methane Decomposition Reactors

Continuous operation of an industrial-scale methane decomposition reactor poses some unique challenges due to the production of solid carbon. When methane decomposition occurs in a non-catalytic tubular reaction furnace without catalyst packing, carbon deposits form on the inner tube walls, eventually blocking the flow of gas (Abánades et al., 2011). Catalytic methane decomposition using catalyst pellets in a packed or fluidized bed result in carbon deposition on the catalyst pellets and eventual catalyst deactivation. Catalyst reactivation involves burning that carbon deposits off the catalyst pellets, which generates CO_2 emissions (Abbas & Wan Daud, 2010; Muradov, 2017).

A bubble column of molten media such a metal, salt, or both has been proposed as a solution to the carbon deposition problem. Methane gas is injected at the bottom of the molten bath. As bubbles rise to the top, the methane decomposition reaction produces hydrogen gas and solid carbon. Studies have found that only a thin layer of carbon (10 μm) forms on the reactor walls, and it does not thicken with time (Geißler et al., 2015; Upham, Agarwal, Khechfe, Snodgrass, Gordon, Metiu, & McFarland, 2017). A liquid medium is selected such that its density is greater than the density of carbon, so that carbon will float to the top of the melt so it can be removed. A significant amount of research has been conducted on the performance of different molten media, as discussed in the next section.

1.5. Molten Media Selection for Methane Decomposition

Preliminary laboratory investigations have studied methane decomposition in pure molten metals with low melting points and viscosities, similar to those of tin (Geißler et al., 2016; Serban et al., 2003) and gallium (Leal Pérez et al., 2021). A molten metal with a low melting point (e.g. 232 °C for tin and 30°C for gallium) is ideal for industrial applications because the materials of construction used for the reactor must be able to withstand the selected operating temperature. A low viscosity molten metal helps facilitate mixing to ensure uniform heating in the bubble column.

Metals with higher catalyst activity such as platinum, nickel, and palladium have higher melting points, whereas metals with lower melting points have lower catalytic properties (Palmer et al., 2019). Recent studies have investigated the use of a molten metal alloy wherein a metal with higher catalyst activity is combined with a "solvent" metal with a lower melting point (Kim et al., 2025; Palmer et al., 2019; Scheiblehner et al., 2023; Upham, Agarwal, Khechfe, Snodgrass, Gordon, Metiu, & McFarland, 2017). Upham et al. studied the rate of hydrogen production for various binary alloys (Upham, Agarwal, Khechfe, Snodgrass, Gordon, Metiu, & McFarland, 2017). Of all the alloys studied, $Ni_{0.27}Bi_{0.73}$ was found to have the highest rate of hydrogen production. Palmer et al. extended the work of Upham by studying the catalytic properties of a Cu-Bi alloys in comparison to Ni-Bi alloys (Palmer et al., 2019). The catalytic activity of the $Cu_{0.45}Bi_{0.55}$ mixture was found to be higher than that of $Ni_{0.27}Bi_{0.73}$ (Palmer et al., 2019). This finding is important for future scale up, because Cu is significantly cheaper than Ni. Recently, Kim et al studied Zn-Bi alloys for methane pyrolysis (Kim et al., 2025). Simulations were used to evaluate the catalytic activity of a $Zn_{0.45}Bi_{0.55}$ mixture and found the activation energy for methane pyrolysis to be even lower than for $Cu_{0.45}Bi_{0.55}$. Again, this finding is significant because Zn is even lower in cost than Cu (Kim et al., 2025).

Molten salts have been studied as another medium for methane pyrolysis due to their low cost, high temperature stability, and non-toxicity (Boo et al., 2021; Kang et al., 2020; Palmer et al., 2021; Parkinson et al., 2021; Pruvost et al., 2022). Kang et al. studied catalytic methane pyrolysis in molten $MnCl_2$-KCl (Kang et al., 2019). It was observed that $MnCl_2$ has a high vapour pressure (0.13 atm at 1000 °C) which is comparable to the partial pressure of methane at the reactor inlet (0.5 atm), so bubbles exiting the melt contained some $MnCl_2$ (Kang et al., 2019). The presence of $MnCl_2$ vapour in the hydrogen product could lead to fouling of downstream heat exchangers in a scaled-up industrial process. Additionally, evaporated $MnCl_2$ will need to be replenished which will add to the operational costs of the reactor. Pruvost et al. conducted a techno-economic assessment of natural gas pyrolysis in a molten mixture of KCl/$MnCl_2$ (Pruvost et al., 2022). To minimize evaporation of salt, the reactor outlet is quenched to 750 °C. The outlet stream was estimated to contain 160 ppm of evaporated salt, which would only require 4 days for a 1mm fouling layer to build up on downstream heat exchangers (Pruvost et al., 2022). Additional quenching could minimize the salt evaporated but would result in a larger flowrate of gas at the outlet, and therefore larger equipment downstream. Studies on methane pyrolysis using alkali-halide salts such as NaCl, NaBr, KCl, and KBr found them to provide low catalytic reactivity (Palmer et al., 2021). Additionally, experimental studies by Parkinson et al. encountered operational issues when salt clogged the disengagement space above the molten salt level (Parkinson et al., 2021).

1.6. Carbon Removal

Different methods have been proposed for the separation of carbon from the molten media. Methods used in experimental investigations do not necessarily translate to continuous operation at an industrial scale. In experiments conducted where the reaction takes place in a cylindrical quartz glass tube, the molten mixture was allowed to cool and solidify before removing the solidified medium and carbon for analysis, sometimes by breaking the quartz tube (Geißler et al., 2015; Kang et al., 2019; Palmer et al., 2021). These methods of carbon separation are only applicable in small scale laboratory experiments.

Von Wald et al. proposed sizing the exit radius of an industrial sized methane pyrolysis reactor to promote entrainment of carbon in the gases so they can be separated using a cyclone (Von Wald et al., 2020). Similarly, Upham et al. proposed entrainment by geometric design or by introducing hydrogen or inert gas at a high flow rate to carry the carbon to a cyclone, bag filter, or other solid-gas separation method (Upham, Agarwal, Khechfe, Snodgrass, Gordon, Metiu, & Mcfarland, 2017). Pérez et al. proposed a reactor design using a molten gallium filled vertical vessel where hydrogen leaves at the top and carbon exits via gravity through a high-temperature resistant pipe with a series of reducing valves to decrease the pressure up to 1 bar. This design is similar to the one employed for slag removal in blast furnaces (Leal Pérez et al., 2021). The carbon exiting is assumed to be pure and is cooled using moving bed heat exchangers. Without testing this process, it is unknown how much molten metal will flow with the carbon as it exits through the pipe. Parkinson et al. proposes using a vertical down-comer to transfer carbon floating on the melt into a gas-solid bubbling-bed vessel where methane can be bubbled through the hot carbon to help cool it and preheat methane before it is fed into the reactor and the cooled carbon is sent to storage (Parkinson et al., 2017). If the carbon is contaminated with molten metal or salt, cooling at this stage would likely clog the gas-solid bubbling bed by solidifying the molten medium. Some researchers proposed skimming the carbon off the top, similar to slag removal in steel manufacturing (Steinberg, 1999; Upham, Agarwal, Khechfe, Snodgrass, Gordon, Metiu, & Mcfarland, 2017). Ultimately, all the proposed methods for carbon removal assume that pure carbon exits the reactor, which greatly simplifies the processing, transport, or disposal of the carbon product. This assumption is, however, unlikely to be true as shown by other studies discussed later in this review.

1.7. Carbon Product Characterization, Degree of Graphitization, and Purity

Multiple studies have been conducted to characterize the carbon produced by methane decomposition. Overall, the design choice to have a molten metal that is more dense than carbon has worked reasonably well in experimental studies because carbon has been observed to form as a powder on top of the melt

(Geißler et al., 2015; Parkinson et al., 2017; Upham, Agarwal, Khechfe, Snodgrass, Gordon, Metiu, & McFarland, 2017). Geißler et al. noted that only a thin layer (7 μm) of carbon formed between the molten metal and the reactor wall, and it did not increase in thickness with time (Geißler et al., 2015). Rahimi et al. introduced a layer of salt (NaBr or KBr) on top of a molten NiBi alloy to reduce metal contamination in the carbon (Rahimi et al., 2019). Carbon interacted differently with different salts, forming a distinct carbon phase on top of the NaBr layer but dispersing within the layer of KBr. This was attributed this to NaBr having a higher density and low adhesion energy with carbon, whereas KBr has a lower density and higher adhesion energy with carbon (Rahimi et al., 2019). This observation agrees with those of Kang et al. where the carbon was completely mixed in with pure KCl and $MnCl_2$(67)-KCl(33) salts when each was tested separately as a medium for methane pyrolysis (Kang et al., 2019).

Research has also aimed to understand which parameters affect the structure of the carbon product. Different studies have observed varying characteristics in the carbon formed from methane pyrolysis depending on the molten media selected and the reaction temperature. Studies of methane pyrolysis using different salts (KCl, NaCl, KBr, and NaBr) observed similar amorphous morphology in the carbon produced using each medium (Palmer et al., 2021; Parkinson et al., 2021). Kang et al. observed similar morphology in carbon produced in pure KCl; however, carbon produced in MnCl2(67)-KCl(33) was more graphitic. Kim et al. had similar observations in the study of ZnBi alloys, where carbon produced on pure molten Bi was amorphous whereas carbon produced on $Zn_{0.45}Bi_{0.55}$ was partially crystalline (Kim et al., 2025). It seems that catalytic methane pyrolysis produces a more crystalline carbon product with a higher degree of graphitization than non-catalytic. When Upham et al. studied catalytic molten metals, they found that most of the carbon was graphite (Parkinson et al., 2017). Palmer et al. also noted that at lower temperatures (950 °C), amorphous spherical particles assembled into larger cauliflower like carbon structures (Palmer et al., 2021). As the temperature increased beyond 1050 °C, the morphology changes to sheet-like structures. Palmer et al. hypothesized that it could be due to the rearrangement process of carbon atoms transitioning from the gas to solid phase (Palmer et al., 2021). This is supported by Parkinson et al.'s observations where

the morphology was cauliflower-like for experiments conducted at 1000 °C (Parkinson et al., 2019). Rahimi et al. observed flakes of graphitic carbon in a single phase NiBi reactor, and spherical morphologies of 20-50 nm in size with aggregates of 100-200 nm produced in a NiBi/KBr two phase reactor (Rahimi et al., 2019).

Research has also aimed to understand the level of contamination in carbon from liquid media bubble reactors used for methane decomposition, which varies greatly depending on the configuration. Upham et al. studied the carbon powder produced in a Ni-Bi liquid metal bubble reactor using x-ray spectroscopy and found it to contain 60.78 wt% C, 32.08 wt% Bi, 2.93 wt% Ni, 2.83 wt% O, and 1.39 wt% Si (Upham, Agarwal, Khechfe, Snodgrass, Gordon, Metiu, & Mcfarland, 2017). Rahimi et al. used a scanning electron microscope with an energy dispersive X-ray analyzer (SEM/EDS) for elemental analysis to study the effect of adding a molten layer of salt (KBr, KCl, or NaBr) on top of molten $Ni_{0.27}Bi_{0.73}$ on the purity of carbon produced. Carbon produced in a bubble column without a layer of salt was significantly more contaminated with metal, with 17.36 wt% C, 12.98 wt% Ni, and 69.66 wt% Bi. Carbon from the experiments using a salt layer were all water-washed before analysis, but contained up to 95.06 wt% carbon, 0.18 wt% Ni, 0.56 wt% Bi, 1.06 wt% Na, and 3.14 wt% Br for a column with 110 mm NiBi layer with 240 mm NaBr on top (Rahimi et al., 2019). Parkinson et al. used thermogravimetric analysis to study the carbon produced using different alkali-halide salts and found the purity of carbon to vary with the salt used (Parkinson et al., 2017). In order of most pure to least, NaCl yielded the purest carbon with 90 wt% C, followed by NaBr with 75 wt% C, KCl with 68 wt% C, NaBr-KBr with 65 wt% C, and KBr which yielded the lowest carbon purity of about 63 wt% C (Parkinson et al., 2021). Parkinson et al. attributed the differences to electrostatic interactions between the carbon and salts, which can be measured by the adhesion energy and contact angle (Parkinson et al., 2021). A higher contact angle between the carbon and salt results in more salt being trapped, and thus a lower carbon purity (Parkinson et al., 2021). Scheiblehner et al. used SEM/EDS analysis to study the carbon produced in molten alloys of CuBi, CuSn, and CuGa (Scheiblehner et al., 2023). Interestingly, the purity of carbon varied with different alloys used. The purest carbon came from experiments using

$Cu_{0.95}Ga_{0.05}$, with 99.5 wt% C. Copper alloys with Sn and Ni resulted in relatively high carbon purity, all with >95 wt% C. Copper alloys with bismuth led to the lowest purity, with $Cu_{0.60}Bi_{0.40}$ giving 49.9 wt% C, and $Cu_{0.20}Bi_{0.80}$ 63.8 wt% C due to the high vapour pressure of bismuth (Scheiblehner et al., 2023). Metals with a higher vapor pressure can evaporate in the reactor and then condense onto the carbon product floating on top. Kim et al. made similar observations studying the carbon produced over a Zn-Bi alloy, except the carbon was more severely contaminated by Zn because it has an even higher vapour pressure than Bi (Kim et al., 2025).

1.8. Carbon Black Market & Uses

Uses for the carbon product vary with its purity and degree of graphitization. Common forms of carbon found on the market are petroleum coke, carbon black, activated carbon, and carbon filaments (Leal Pérez et al., 2021). Graphitic carbon is of higher value if it can target the market of carbon anodes for battery and metal production industries (Pruvost et al., 2022). Carbon black has an amorphous structure, and 90% of its production is used in rubber applications, mostly for tires in the automotive industry, but can also be used as a pigment in inks and coatings (Palmer et al., 2020; Patnaik & Brown, 2010). Typical rubber-grade carbon black is >97.3 wt% carbon, with traces of 0.20-0.40% H_2, 0.2-1.20% O2, 0.2-1.2% S, 0.1-1.00% ash and 0.6-1.5% volatile components on a dry basis (Y. Wang et al., 2001).

The carbon black market size is forecasted to increase from USD $24.10 billion in 2025 to USD $31.87 billion by 2030 at a CAGR of 5.75% (Mordor Intelligence, 2025). The carbon black industry is evolving with changing markets. Vehicle production showed a 14% increase in 2023 compared to the previous year, which drives the need for carbon black in tire manufacturing and automotive components. Global electric vehicle sales demonstrated a 25% increase in 2023 over the previous year, which indicates strong future demand for carbon black in EV-related applications (Mordor Intelligence, 2025). In the event that large

scale production of hydrogen by methane pyrolysis results in more carbon product than the market demands, the carbon may have to just be stored safely, which will incur additional costs.

1.9. MDR Techno-Economic Analyses

Economic analyses involving methane decomposition processes highlight the need for more knowledge on the available market for the carbon product. Methane decomposition appears to be a favourable technology, particularly for methanol production, however the findings are based on some fundamental assumptions about the carbon purity and market (Catalan et al., 2023).

Parkinson et al. conducted a techno-economic assessment of methane pyrolysis in molten metals where they used a discounted cash flow analysis to determine the estimated return on invested capital for pyrolysis processes compared to SMR (Parkinson et al., 2017). Increasing taxes on CO_2 emissions are expected to play a role in the economic performance of hydrogen producing processes as time continues. At different CO_2 tax rates ranging from \$0/tonne to \$100/tonne, Parkinson et al. determined the price of H_2 that achieved a 10% internal rate of return for SMR. Then, they used that same H_2 price and CO_2 tax value to determine the IRR for pyrolysis. Pyrolysis was found to be competitive with SMR when the carbon tax was USD \$78/tCO_2 (Parkinson et al., 2017). They assumed the carbon product to be sellable at \$200/t as coking coal, which is burned in coal plants as fuel. This would significantly add to the indirect emissions from hydrogen produced by methane pyrolysis if that is how the carbon is used. As net-zero emissions are pursued, the demand for coking coal will be reduced. Unless the market for carbon from methane pyrolysis is developed for other applications, it is more likely that the carbon will incur costs for storage in a landfill if produced on a large scale (Parkinson et al., 2017). Pruvost et al. also commented that the potential of the process is linked to the size of the market for the carbon product (Pruvost et al., 2022). The price at which carbon can be sold increases as the market size decreases. The market size for carbon used for electricity and heat is the largest, between 1200-9000 Mton/year, then metallurgy, chemicals, and biochar at 750 to 1100

Mton/year, then carbon anodes, graphite and sorbents at 40-70 Mton/year. If the pyrolysis process is restricted to selling carbon at high prices, then the hydrogen produced can only take up a small amount of the hydrogen market. If the economics are justified by selling carbon at a lower price, then the market potential for hydrogen produced using methane pyrolysis is much larger. Catalan et al. conducted a techno-economic analysis of a low carbon methanol process where hydrogen is produced in a liquid bubble reactor filled with $Cu_{0.45}Bi_{0.55}$ with a layer of salt, such as NaBr on top (Catalan et al., 2023). The levelized cost of carbon (LCOC) is defined as the carbon sale price required to make the net present value of the project to be zero. The LCOC was found to be $0.269/kg. This carbon selling price is very competitive with the price of carbon black used for rubber tires, which ranged from $1.4 to $2.5/kg in 2021. In their work, the carbon is assumed to be purified sufficiently with hot washing with HCl solution, as Rahimi et al. demonstrated in their experiments. However, the cost of HCl washing or carbon drying was not modeled or included in the economic analysis. Similarly, Angikath et al. conducted a techno-economic assessment of hydrogen production from natural gas pyrolysis in molten bubble column reactors (Angikath et al., 2024). They studied three molten media: NiBi, Ga, and KCl-$MnCl_2$. The process uses a 9.7 MW electric arc furnace to evaporate salt in the carbon by thermal cleaning. Molten KCl-$MnCl_2$ was the least expensive molten media; however, it might be challenging to separate from carbon at high temperatures due to its lower density. In the end, they suggested $Ni_{0.27}Bi_{0.73}$ might be the most viable option. However, the electric arc furnace would be insufficient to remove metal impurities from the carbon. They conducted a sensitivity analysis on the LCOC to evaluate the impact of natural gas, hydrogen, and electricity costs. Natural gas prices vary globally and fluctuate with supply and demand and ultimately have a significant effect on the LCOC. In regions where natural gas is consistently lower in price such as the middle east and the US, the LCOC can approach zero or even negative values if the cost of natural gas is $100/ton and electricity is $48/MWh. However, if the cost of electricity drops due to changes in the mix of electricity found in the grid, then the LCOC can remain low even at higher natural gas prices.

The conclusion of these studies underscores the need for larger prototypes of catalytic methane decomposition reactors with molten metals, complete with carbon purification processes. Understanding the carbon produced at larger scales is critical to accurately predicting the economic viability of methane decomposition.

1.10. Carbon Product Cleaning

Based on the current knowledge of catalytic methane decomposition, a large-scale process is incomplete without a carbon purification step. Several researchers have experimented with different methods of removing impurities at a laboratory scale. Rahimi et al. proposed adding a layer of molten salt on top of molten NiBi, so that metallic particles will be scrubbed from carbon particles as they float up through the salt layer and the carbon will be mostly contaminated with salt as opposed to metal (Rahimi et al., 2019). Observations from SEM/EDS spot analysis indicated that there was a significant increase in carbon purity in experiments with molten salt layers on top of the metal in comparison to experiments with no salt layer, from 17.36 wt% C with no salt up to 95.06 wt% C with 240 mm NaBr and just water washing. However, this approach has not been tested on a larger scale to see if vigorously bubbling the contents of the column would cause the salt and carbon to mix with the molten metal more than observed in experiments using a quartz tube with a 22 mm ID (Rahimi et al., 2019). Rahimi et al. also studied the effectiveness of different purification treatments for carbon contaminated with 12.98 wt% Ni and 69.66 wt% Bi after water washing. Vacuum heating at 1000 °C for 12 h reduced the nickel and bismuth content down to 1.84 wt% and 46.34 wt%, respectively. In another set of experiments, refluxing in 1 M HCl at 70 °C for 24h reduced the nickel and bismuth content down to 4.09 wt% and 37.10 wt%, respectively (Rahimi et al., 2019). Palmer et al. also studied cleaning methods for carbon produced over a NiBi catalyst (Palmer et al., 2020). Treatments included vacuum distillation at 1100 °C and HCl washing which resulted in similar observations to Rahimi et al. (2017). They also tried magnetic extraction which decreased Ni contamination from 0.73 wt% to 0.32 wt% (Palmer et al., 2020). Palmer et al. concluded that the metal contamination level and costs associated

with cleaning were likely unacceptable in a commercial process. They recommended using a salt layer on top of the melt, as Rahimi et al. (2017) did, to minimize metal losses and replace metal contaminants with salt which may not be as limited in options for disposal or application as a product.

Studies on the purification of carbon contaminated with salt have proven that it is not as simple as originally hoped. Palmer et al. studied purification methods for carbon contaminated with alkali halide salts (KCl, NaCl, KBr, NaBr) (Palmer et al., 2021). Hot water washing at 70 °C for 2 h resulted in considerable remaining contaminant levels of salt ranging from about 15 to 35 wt%. They also tried heat treatment at 1100 °C for 12 h to vaporise salt. Heat treatment was more effective for potassium-based salts as opposed to sodium-based salts, where the contamination levels were reduced to <3 wt% and 27.5 wt%, respectively. An additional heat treatment at 1500 °C, above the boiling point of NaCl, was done for 12 hours which reduced the NaCl content to 3.5 wt%. Boo et al. had similar observations when studying the purity of carbon produced from methane pyrolysis in molten KCl (Boo et al., 2021). After warm water washing at 50 °C, HCl washing at 50 °C, and sonication in 50 °C water, they concluded that despite the solubility of KCl in water, high levels of KCl remained in the salt after these treatments. They also tried heating under a vacuum at 1000 °C, which increased the purity of water washed carbon from 93.4 at% to 95.2 at%. However, they concluded that this was still too much KCl loss to justify this method of hydrogen production. They also tried heating the carbon to 1200 °C, closer to the boiling point of KCl (1420 °C), under flowing Ar. The argon was flowed to prevent the carbon from burning at the high temperature. This increased the purity of water washed carbon from 93.4 at% to 97.2 at%. Boo et al. commented that heat treatment is the most advantageous method of carbon purification because it reduces the amount of wastewater generated when compared to water-related procedures, and because the evaporated salt can be recovered and reused (Boo et al., 2021).

To the authors knowledge, the only proposed method of carbon purification on an industrial scale has been described by Pruvost et al. for their techno-economic assessment of natural gas pyrolysis in a 50/50 mixture

of $MnCl_2$ and KCl (Pruvost et al., 2022). They propose using quench gas at the outlet of the pyrolysis reactor to prevent carryover of evaporated salt in the hydrogen stream, which would lead to excessive fouling in the downstream heat exchangers. Then, the carbon contaminated with salt is processed in an electrically heated shaft furnace to heat the carbon to 1450 °C above the boiling point of KCl at atmospheric pressure. Other heating options suggested are a microwave system to ensure uniform heating, or resistive heating elements for a more economical option. Nitrogen purge gas is used to transport the evaporated salt, then the hot carbon is cooled in a steam generating heat exchanger down to 60 °C (Pruvost et al., 2022). However, none of the proposed methods have been practically tested.

1.11. Knowledge Gap, Objectives, and Organization of This Thesis

Substantial research has been conducted to understand the catalytic activity of various molten metals and salts, as well as to characterize the carbon produced from catalytic methane decomposition; and techno-economic analyses underscore the necessity to sell the carbon. Only bench-scale experimental studies have been conducted to study methods for cleaning the carbon so that it can be sold. Bench-scale studies on carbon cleaning have been generally unsuccessful at purifying the carbon to rubber-grade carbon black purity. However, no research has been conducted to develop an industrial-scale process to purify the carbon product from catalytic methane decomposition.

In the present study, a detailed process design for the purification of carbon contaminated with $Cu_{0.45}Bi_{0.55}$ alloy from catalytic methane pyrolysis on a large scale is presented. Multiple steps are required to remove and recover bismuth and copper from the carbon product, followed by drying the purified carbon. The Methods section describes the theory, equipment, and design equations used to model and size equipment for each step in the process. The Sizing section demonstrates the application of the methods described as they are used to design a process that purifies carbon produced in the methane decomposition reactor described by Catalan & Rezaei, which produces 10,000 Nm^3/h, corresponding to a small-scale hydrogen

plant (Catalan & Rezaei, 2022). The Costing section describes the methodology used to estimate the capital costs of the carbon processing equipment. Last, the Conclusions section highlights the most significant findings of this work followed by recommendations for future research.

2. Methods

The processing steps for carbon contaminated with $Cu_{0.45}Bi_{0.55}$ alloy are outlined in Figure 1. First, bismuth is removed by a vacuum distillation process and recycled back to the MDR reactor. Next, the mixture of carbon and molten copper is cooled, granulated, and ground to a fine solid particle size. The fine particles of carbon and copper increase the surface area of the mixture, which allows for efficient leaching of the copper metal in the next step of the process. Copper metal is dissolved in an aerated leaching tank with dilute sulfuric acid. The resulting heterogenous mixture is composed of solid carbon in an aqueous solution of $Cu^{2+}_{(aq)}$, $SO_4^{2-}{}_{(aq)}$ and $HSO_4^{-}{}_{(aq)}$. A rotary drum vacuum filter is used to separate the carbon from the liquid. The purified carbon is rinsed and dried for packaging. Copper ions in the remaining liquid are recovered as copper metal by cementation wherein copper ions precipitate out of solution in the presence of scrap iron due to differences in the reduction potential of each metal. The precipitated copper is a fine powder that can be filtered from the solution using a rotary drum vacuum filter. The copper powder is rinsed and dried before it is recycled back to the MDR reactor. This section provides a detailed overview of the process design equations and theory for each step of the carbon purification process.

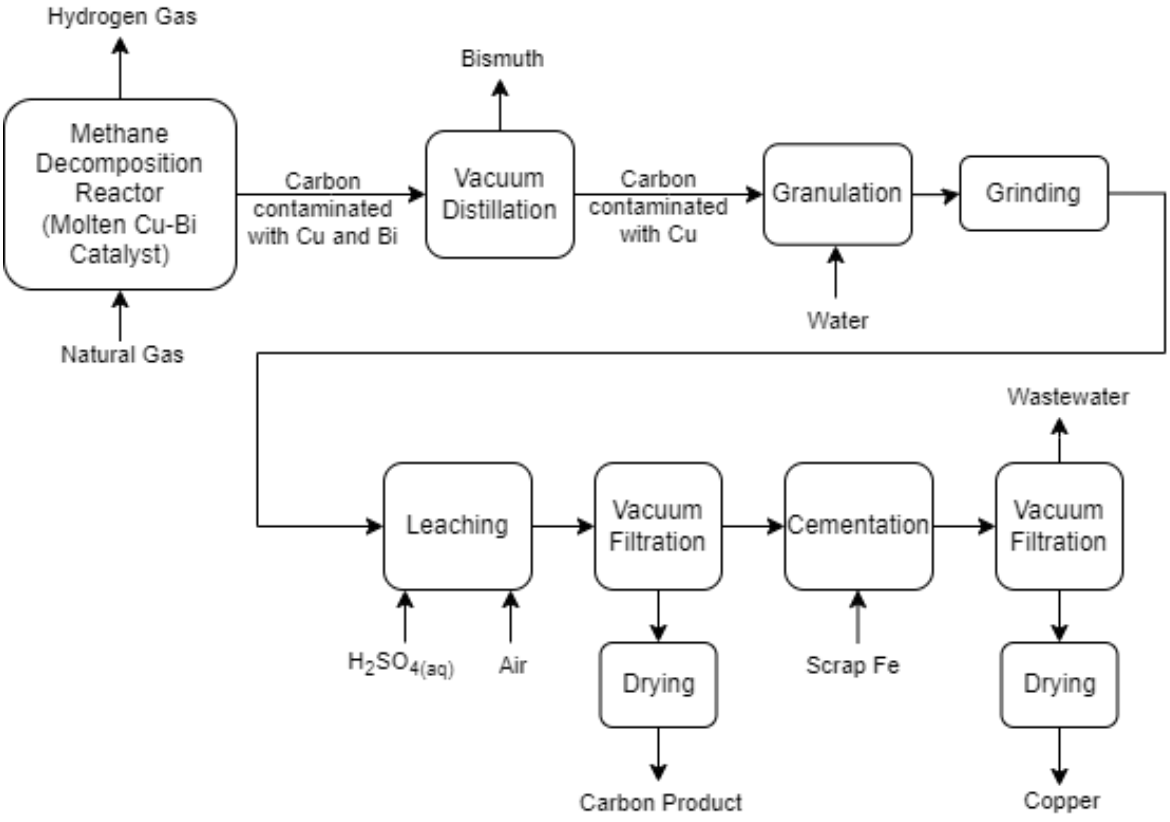

Figure 1: Block flow diagram of the carbon processing steps

2.1. Bismuth Removal by Vacuum Distillation

2.1.1. Phase Equilibrium for Cu-Bi Mixtures

Chen et al. (2019) studied Cu-Bi alloys under vacuum distillation by measuring the vapour-liquid equilibrium at 10 Pa. They modeled the VLE diagrams for Cu-Bi at 10 Pa using the Wilson equation and compared the results to their experimental data (Figure 2). At temperatures above 1200 K, the mole fraction of copper in the liquid phase is very close to 1. This allows us to conclude that it is physically possible to remove nearly all of the bismuth by vacuum distillation, and that the process is not limited by thermodynamics. At high temperatures above 1350 K, the vapour phase contains some copper, up to 15 mole % at 1550 K. Therefore, if the vacuum distillation process operates at high temperatures above 1350

K, it is expected that the recovered bismuth will contain some copper. Since the recovered bismuth will be recycled back to the MDR reactor as catalyst, the presence of some copper is not expected to cause any issues.

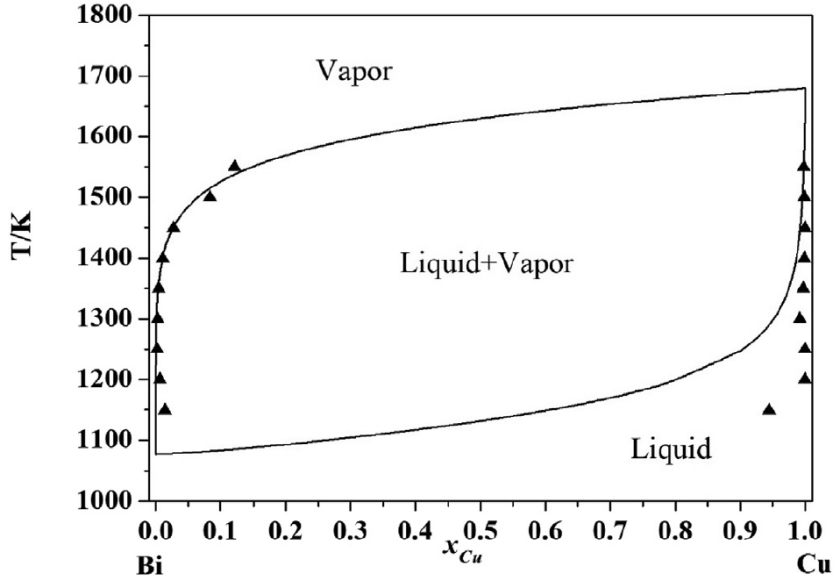

Figure 2: Comparison of the predicted VLE of calculation (lines) with experimental data (symbols) of Cu-Bi alloy at 10 Pa (Chen et al., 2019).

2.1.2. Preferential Evaporation of Bismuth

The separation of bimetallic alloys such as Cu-Bi using vacuum distillation relies on differences in vapour pressure between each constituent. The relative volatility coefficient α is used to compare the vapour pressures with consideration for the molecular weight of each constituent (Equation 5). Ideally, α should be either very large or very small. When α is unity, separation by vacuum distillation is not possible, as each component will have similar concentrations in the vapour phase and in the condensed phase (Ozberk & Guthrie, 1986).

$$\alpha = \varphi^{\circ}_{Bi}\left(\frac{P^{\circ}_{Bi}}{P^{\circ}_{Cu}}\right)\sqrt{\frac{M_{Cu}}{M_{Bi}}} \qquad \text{Eq 5}$$

In Equation 5, φ°_{Bi} is the unitless equilibrium activity coefficient of bismuth, P°_{Bi} and P°_{Cu} are the equilibrium vapour pressures of pure liquid bismuth and copper, while M_{Bi}, and M_{Cu} are the molecular weights of bismuth and copper. Correlations to calculate φ°_{Bi}, P°_{Bi}, and P°_{Cu} are outlined in Appendix A. Figure 3 illustrates the effect of temperature on α and on the partial pressures of Bi and Cu. Over the temperature range 900 – 1700K, Bi exhibits higher vapour pressures than Cu, and α is sufficiently high for preferential separation of Bi from a Cu-Bi melt to be achievable by vacuum distillation.

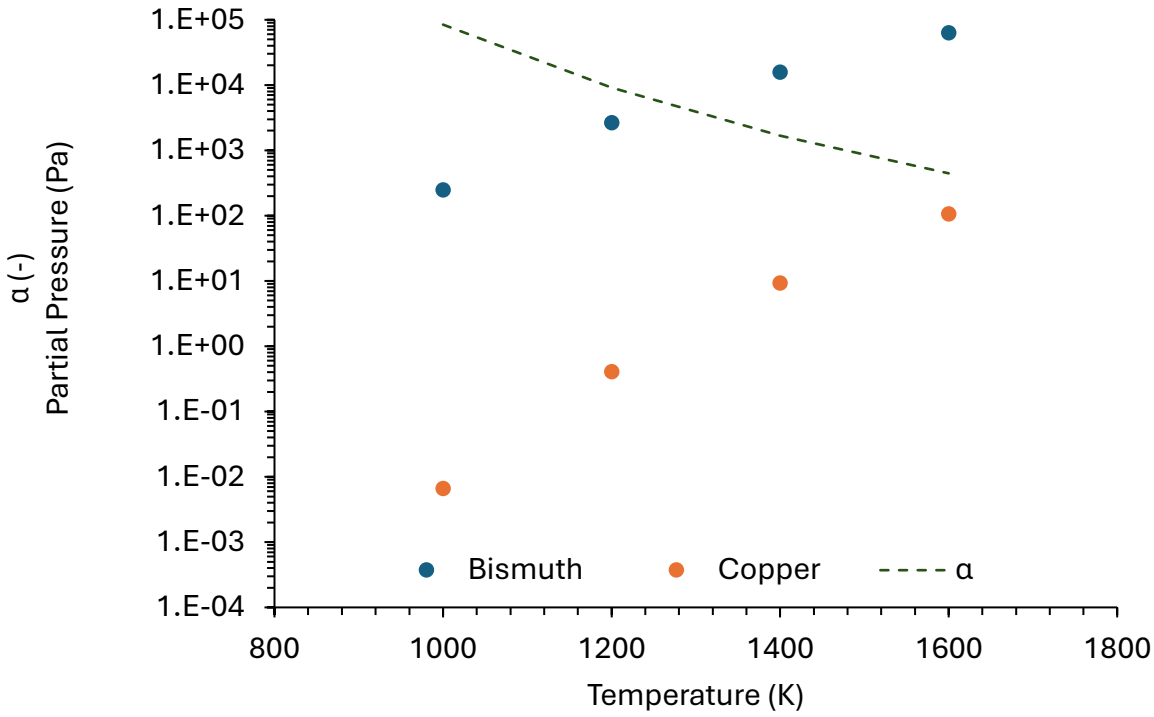

Figure 3: Partial pressures of pure species (Bi and Cu) and relative volatility coefficient versus temperature.

2.1.3. Mass Transfer Rate of Bismuth in Copper Melts

Ozberk and Guthrie presented a kinetic model for the vacuum refining of inductively stirred copper melts (Ozberk & Guthrie, 1986). The rate of bismuth mass transfer (r_{Bi}, kg/s) in vacuum distillation follows first order kinetics and can be modeled by Equation 6 (Ozberk & Guthrie, 1986):

where K is the overall mass transfer rate constant (m/s), A is the surface area of the melt (m^2), and C_{Bi}^B is

$$r_{Bi} = KAC_{Bi}^B \quad \text{Eq 6}$$

the bulk concentration of bismuth in the melt (kg_{Bi}/m^3).

The overall mass transfer rate coefficient (K, Equation 7) is a function of three mass transport processes, each with their own respective rate constant: mass transfer from the bulk liquid phase to the liquid-gas interface (K_L, m/s), evaporative mass transfer across the liquid-gas interface (K_E, m/s), and mass transfer in the gas phase away from the liquid-gas interface, which K_U (m/s) accounts for (Ozberk & Guthrie, 1986).

$$\frac{1}{K} = \frac{1}{K_L} + \frac{1}{K_E} + \frac{1}{K_U} \quad \text{Eq 7}$$

Ozberk & Guthrie (1986) used the Machlin model, Equation 8, to estimate K_L for an inductively stirred melt.

$$K_L = \sqrt{\frac{8D_{Bi}U_{Bi}}{\pi r_{melt}}} \quad \text{Eq 8}$$

where D_{Bi} is the diffusivity of bismuth in the melt (m^2/s), U_{Bi} is the mean velocity of bismuth at the surface of the melt (m/s), and r_{melt} is the radius of the melt (m).

Ozberk (1980) used an Arrhenius-type equation to estimate D_{Bi} at different temperatures.

$$\frac{D_{1423K}}{D_{Bi}} = e^{-\Delta E/R\left(\frac{1}{1423}-\frac{1}{T(K)}\right)} \quad \text{Eq 9}$$

where D_{1423K} is the diffusivity of bismuth at 1423 K, estimated by Ozberk & Guthrie (1986) to be 1.0x10^{-9} m^2/s, ΔE is the activation energy (30 kcal/mol), and R is the universal gas constant (1.987x10-3 kcal·K^{-1}·mol^{-1}). The mean velocity of bismuth at the surface of the melt, U_{Bi}, is related to the melt temperature, the melt area-to-volume ratio, the melt diameter, and the characteristic frequency of inductive stirring (Harris, 1984). Harris (1984) presented typical values of melt surface velocities for various experimental conditions, ranging from 0.09 to 0.13 m/s. Ozberk & Guthrie (1986) took an average U_{Bi} value of 0.10 m/s in their model.

The evaporation mass transfer coefficient at the theoretical maximum rate of bismuth evaporation from the liquid surface under a perfect vacuum is given by (Ozberk & Guthrie, 1986):

$$K_E = \frac{\zeta P^{\circ}_{Bi} \varphi_{Bi} M_{Cu}}{\rho_{Cu}\sqrt{2\pi R T M_{Bi}}} \quad \text{Eq 10}$$

where ζ is the unitless surface evaporation coefficient and is taken as unity for liquid metals (Ozberk & Guthrie, 1986). The equilibrium vapour pressure of bismuth P°_{Bi} is in Pa, the density of copper ρ_{Cu} is in kg/m^3, and the molecular weights of copper and bismuth are in kg/mol. A perfect vacuum implies that no evaporated bismuth condenses back into liquid.

Because the gas phase mass transfer coefficient was not experimentally quantifiable, Ozberk and Guthrie (1986) conducted experiments to obtain K, calculated K_L and K_E analytically, and then combined their results to obtain K_U by Equation 7. Using their results, Ozberk & Guthrie (1986) developed an empirical correlation for K_U (m/s) based on temperature (°C) and pressure (Pa):

$$K_U = [-14.526 + 11.75 \times 10^{-3}(T) + 29.464(1/P)] \times 10^{-5} \quad \text{Eq 11}$$

Because Equation 11 was developed using experimental data in the ranges 8 - 13.3 Pa and 1150 - 1350 °C, extrapolation to lower temperatures or higher pressures can yield negative values for K_U, as illustrated by Figure B1 in Appendix B. Furthermore, Figure B2 shows that the overall mass transfer coefficients of Bi predicted by combining equations 7 to 11 satisfactorily match the experimental data of Ozberk & Guthrie (1986).

2.1.4. Lift-Spray Vacuum Distillation Apparatus

The rate of bismuth mass transfer (r_{Bi}) increases proportionally with the surface area of the melt (A), as shown by Equation 6. When designing a batch vacuum distillation process for a desired amount of bismuth removal and processing time, the required melt surface area could be considerable. To help increase the available surface area, a patented "lift-spray" vacuum distillation process has been studied by Allaire & Harris (1989a; 1989b), Harris (1984), and Harris & Davenport (1982). This invention is an adaptation of the RH (Ruhrstahl Heraeus) degassing process used in steelmaking, wherein snorkels submerged in liquid steel are injected with gas, causing steel to flow up an upleg into a vacuum chamber where dissolved gases such as hydrogen and nitrogen can be removed from the steel. This work proposes an adaptation of the lift-spray vacuum distillation process for the separation of bismuth from the mixture of bismuth, copper, and solid carbon leaving the methane decomposition reactor.

As illustrated in Figure 4, solid product leaving the MDR is fed into the melt crucible where it is inductively heated to a temperature > 1085 C°. The melt crucible temperature must maintain the molten state of the metal even after nearly all the bismuth has been evaporated from the melt. Since the melting point of copper

(1085 °C) is higher than that of bismuth (271 °C), the melt crucible temperature must be higher than 1085 °C. The top surface of the product in the melt crucible is at atmospheric pressure.

Above the melt crucible is an enclosed vacuum chamber. Steam ejectors can be used to evacuate gasses from the vacuum chamber and control the vacuum pressure. A tubular riser extends from the melt crucible to the vacuum chamber. A lifting gas, such as hydrogen, is injected at the base of the riser. The mixture of molten metal and carbon flows upward in the riser, along with the lifting gas, into to the vacuum chamber. The drop in pressure between the bottom and the top of the riser results in gas expansion, causing the mixture of molten metal and carbon to disperse in a spray as the gas bubbles burst. Spraying the mixture into the vacuum chamber significantly increases the surface area of the melt, thus increasing the rate of bismuth removal. The melt radius, r_{melt}, needed to evaluate the mass transfer coefficient in the liquid phase (K_L, Equation 8) is taken as the mean radius of the droplets in the spray. Because the solids contain a high concentration of bismuth (≈70 wt% (Rahimi et al., 2019)), multiple risers may be needed to increase the available surface area for mass transfer. The mixture of remaining bismuth, copper, and carbon falls to the base of the vacuum chamber where it drains back into the melt crucible through a conduit, facilitating mixing in the melt crucible. Additionally, the melt crucible must remain oxygen-free to prevent the combustion of the hydrogen lifting gas at high temperatures.

Before gases are evacuated through the steam ejectors, they pass through a vapour condensing arrangement consisting of multiple vertical plates with a large surface area. Figure 5 illustrates the view from the top of the condensing arrangement. The preferred condenser surface area is 0.35 m^2 to 0.60 m^2 per tonne of metal in the treated batch (Harris & Davenport, 1984). The plates extend out from a central joint into troughs surrounding the perimeter of the vacuum chamber. As bismuth condenses on the plates, the liquid adheres to their surface and flows down into the bismuth collection trough without dripping back into the molten metal. The liquid bismuth then exits the trough by flowing through the leg leading to the bismuth collection vessel. The central joint at the top of the condenser is connected to a heat transfer element which cools the

plates enough to condense the bismuth without solidifying it. The bismuth dew point temperature varies with the pressure of the vacuum chamber, which should be optimized for each specific application.

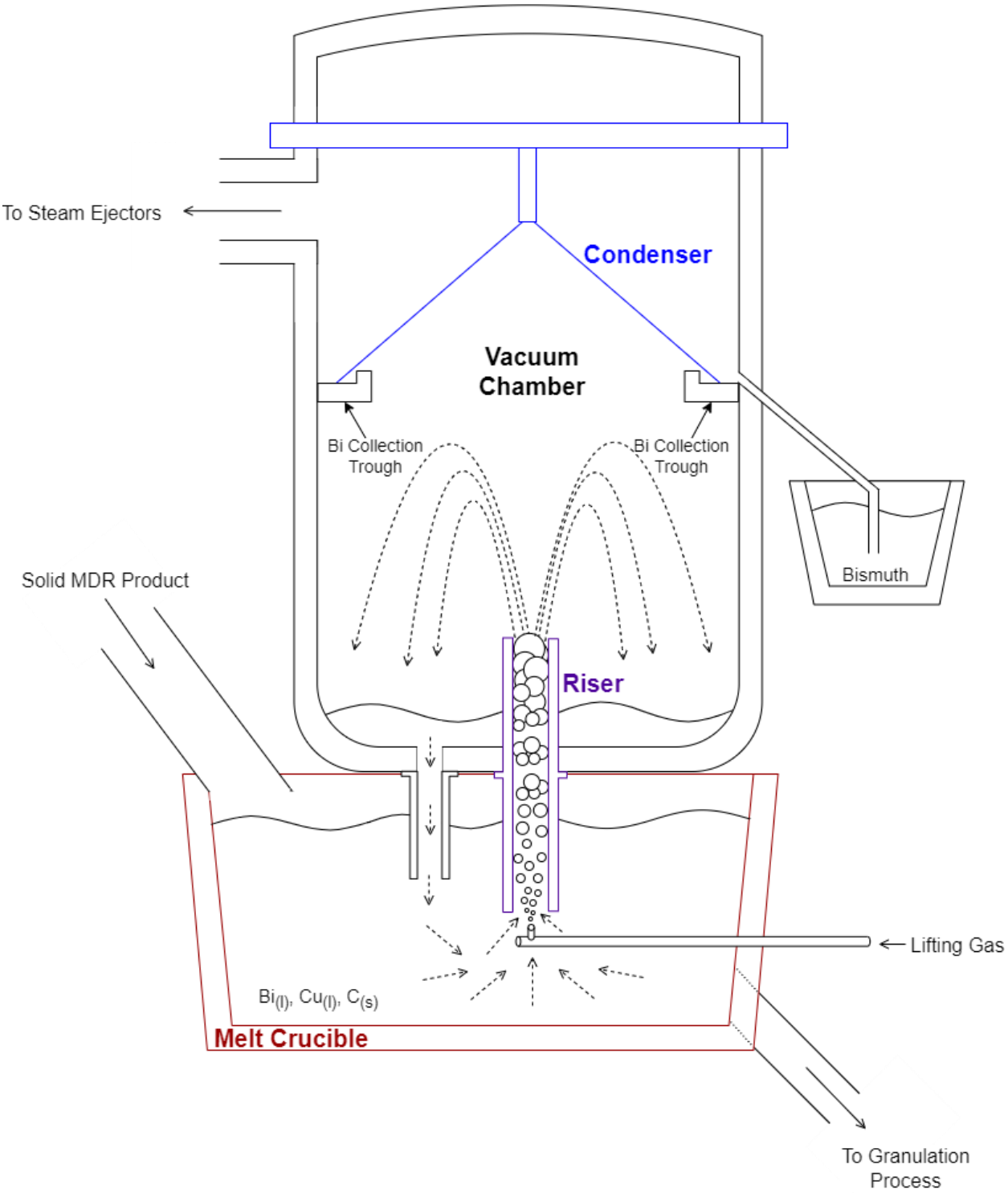

Figure 4: Conceptual diagram of lift-spray apparatus adapted from Allaire (1991) and Harris & Davenport (1984).

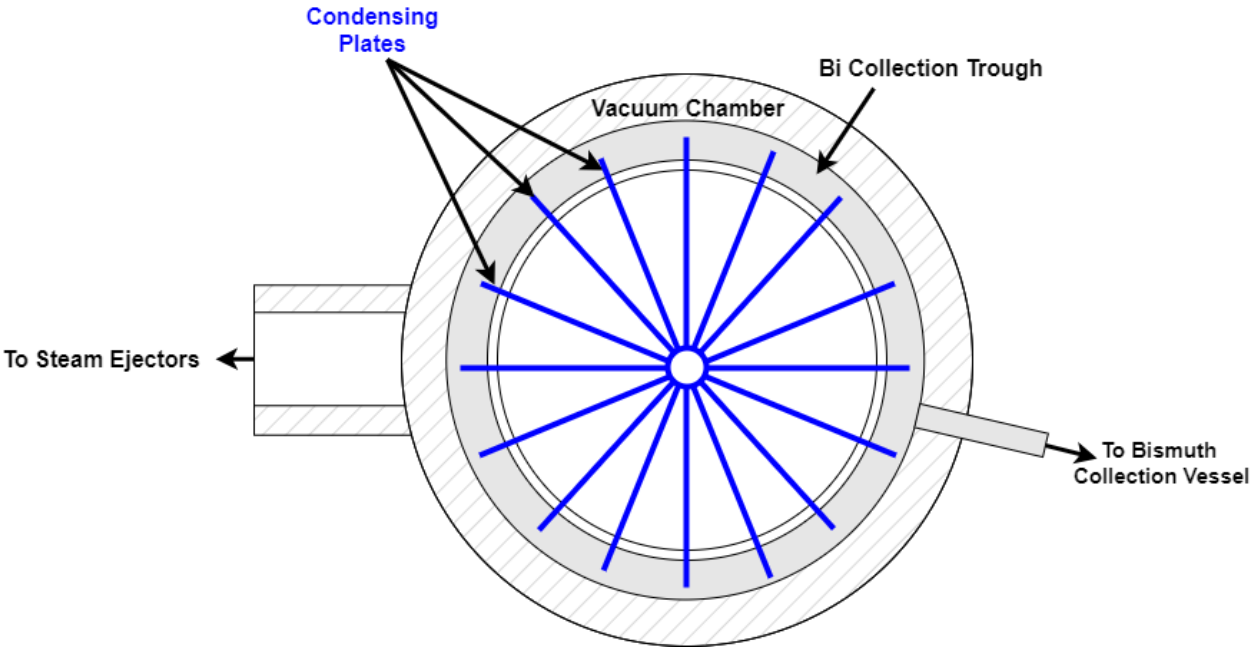

Figure 5: Top view of condensing plates of lift spray apparatus

2.1.5. K_L (Liquid Phase Mass Transfer Coefficient, m/s) in Lift-Spray Droplets

Section 2.1.2 presented the mass transfer model used by Ozberk & Guthrie (1986) for inductively stirred melts. This model contains the term K_L for mass transfer from the bulk liquid phase to the liquid-gas interface. The Machlin model, Equation 8, is used to calculate K_L for liquid-phase mass transfer in the inductively stirred melt, a system with simple hydrodynamics when compared to the droplets of the lift

spray apparatus. K_L is a function of U_{Bi}, the melt surface velocity, which has been studied for inductively stirred melts but not for droplets projected into a vacuum as seen in the lift-spray vacuum distillation apparatus. To the author's knowledge, there are no models for the surface velocity of solutes in a droplet projected into a vacuum space. Allaire (1991) comments on the challenges with accurately estimating K_L for copper matte vacuum purification using a lift-spray apparatus and uses an average value from the literature for liquid metal stirred systems of 2×10^{-4} m/s for his model.

Fundamental mass transfer concepts can be used to frame the minimum and maximum limits of K_L for bismuth in the droplets. The dimensionless Sherwood number, Sh, represents the ratio of total mass transfer from convection and diffusion to the rate of diffusive mass transfer (Treybal, 1981).

$$Sh = \frac{K_L d}{D_{Bi}} \qquad \text{Eq 12}$$

where d (m) is the mean liquid droplet diameter. If there is significant internal convection inside the liquid droplet, Sh is a function of the Peclet number Pe:

$$Sh = 2 + C.Pe^n \qquad \text{Eq 13}$$

where Pe is given by:

$$Pe = \frac{U_{Bi} d}{D_{Bi}} \qquad \text{Eq 14}$$

and the constants C and n depend on the specific flow and transport mechanisms inside the droplet. When there is no convection inside the droplet (U_{Bi}=0), mass transfer inside the droplet is purely diffusion-driven and Equation 13 simplifies to $Sh = 2$. Combining this result with Equation 12 sets a minimum value for the liquid phase mass transfer coefficient:

$$K_{L,min} = 2\frac{D_{Bi}}{d} \quad \text{Eq 15}$$

At 1360 K (the melting point of copper), D_{Bi} is estimated to be 6.12x10^{-10} m^2/s using Equation 9. The gas lift spray droplet diameter can be approximated as 0.02 m (Lee, 1988). Therefore, $K_{L,min}$ is on the order of 6.1x10^{-8} m/s.

Conversely, if convection dominates inside the droplet (high U_{Bi}), Equation 13 indicates that Sh scales as Pe^n where n ≈ 1/3 (Treybal, 1981). For high enough Pe values, K_L, which is proportional to Sh (Equation 12), can become much larger than K_E and K_U such that it no longer affects the overall mass transfer coefficient.

$$\frac{1}{K} = \frac{1}{K_L} + \frac{1}{K_E} + \frac{1}{K_U} \approx \frac{1}{K_E} + \frac{1}{K_U} \quad \text{Eq 16}$$

Physically, Equation 16 means that there is no resistance to mass transfer in the liquid phase, and the evaporative and gas phase mass transport processes control the removal of bismuth.

For comparison, Allaire (1991) studied copper matte purification using a lift-spray apparatus and selected a K_L value of 2x10^{-4} m/s from literature for his model (Allaire & Harris, 1989b; Herbertson & Harris, 1985). Similarly, Ozberk & Guthrie (1986) calculated K_L values ranging from 5.09 x10^{-5} m/s at 1150 °C up to 9.78 x10^{-5} m/s at 1350 °C using Equation 8 and assuming U_{Bi}= 0.10 m/s. Despite the limitations of the Machlin model, Equation 8 is used to estimate K_L in this work. Equation 9 is used to calculate D_{Bi}, and U_{Bi} is taken as 0.10 m/s as done by Ozberk & Guthrie. The predicted minimum value of K_L at 6.1x10^{-8} m/s is lower than Allaire's estimate, which may ultimately lead to the design of an oversized lift spray apparatus in this work. A recommendation for future research is the development of a liquid phase mass transport coefficient (K_L) model for the specific geometry of droplets sprayed into a vacuum distillation chamber. Additionally, the

empirical model for K_U should be extended to include a larger range of temperatures and pressures used for this application (section 3.2.1).

2.1.6. Surface Area For Mass Transfer

For the lift-spray apparatus, the total surface area of the droplets $A_{droplets}$ (m^2) is significantly larger than the surface area of the melt in the crucible (A). Therefore, Equation 6 is modified so that the rate of bismuth mass transfer depends on $A_{droplets}$:

$$r_{Bi} = KA_{droplets}C_{Bi}^{B} \quad \text{Eq 17}$$

An analytical model for calculating $A_{droplets}$ is required to determine the rate of bismuth removal. Allaire (1991) proposed a set of calculations for the scale-up of a lift-spray apparatus to industrial size. The present work adapts these calculations to the processing of carbon contaminated with copper and bismuth, as detailed in the following.

Assuming that the spray consists of spherical droplets of equal radius r (m), the specific area (A_S, m^2/m^3) of the spray is:

$$A_S = \frac{4\pi r^2}{4/_3\,\pi r^3} = \frac{3}{r} \quad \text{Eq 18}$$

Hence, the total surface area of all the droplets $A_{droplets}$ (m^2) is related to the total volume of droplets suspended in the spray $V_{droplets}$ (m^3) by:

$$A_{droplets} = \frac{3V_{droplets}}{r} \quad \text{Eq 19}$$

Moreover, $V_{droplets}$, depends on the volumetric flow rate of liquid in the riser $Q_{L,riser}$ (m^3/s), the exposure time of each droplet (t_e, s) before it reaches the base of the vacuum chamber, and the number of risers (N_{risers}):

$$V_{droplets} = Q_{L,riser} t_e N_{risers} \quad \text{Eq 20}$$

The number of risers (N_{risers}) can be optimized to increase or decrease the rate of bismuth removal as desired. Furthermore, the superficial velocity of the liquid in the riser, J_L (m/s), is given by:

$$J_L = \frac{Q_{L,riser}}{\pi r_{riser}^2} \quad \text{Eq 21}$$

where r_{riser} (m) is the internal radius of the riser. In this work, r_{riser} is taken as 0.2m, a typical riser radius of RH degassing units in industry (Allaire, 1991). Combining Equations 20 and 21 gives:

$$V_{droplets} = t_e N_{risers} J_L \pi r_{riser}^2 \quad \text{Eq 22}$$

The exposure time of each droplet in the vacuum chamber (t_e) is estimated by assuming that each droplet follows a parabolic flight path as illustrated in Figure 6.

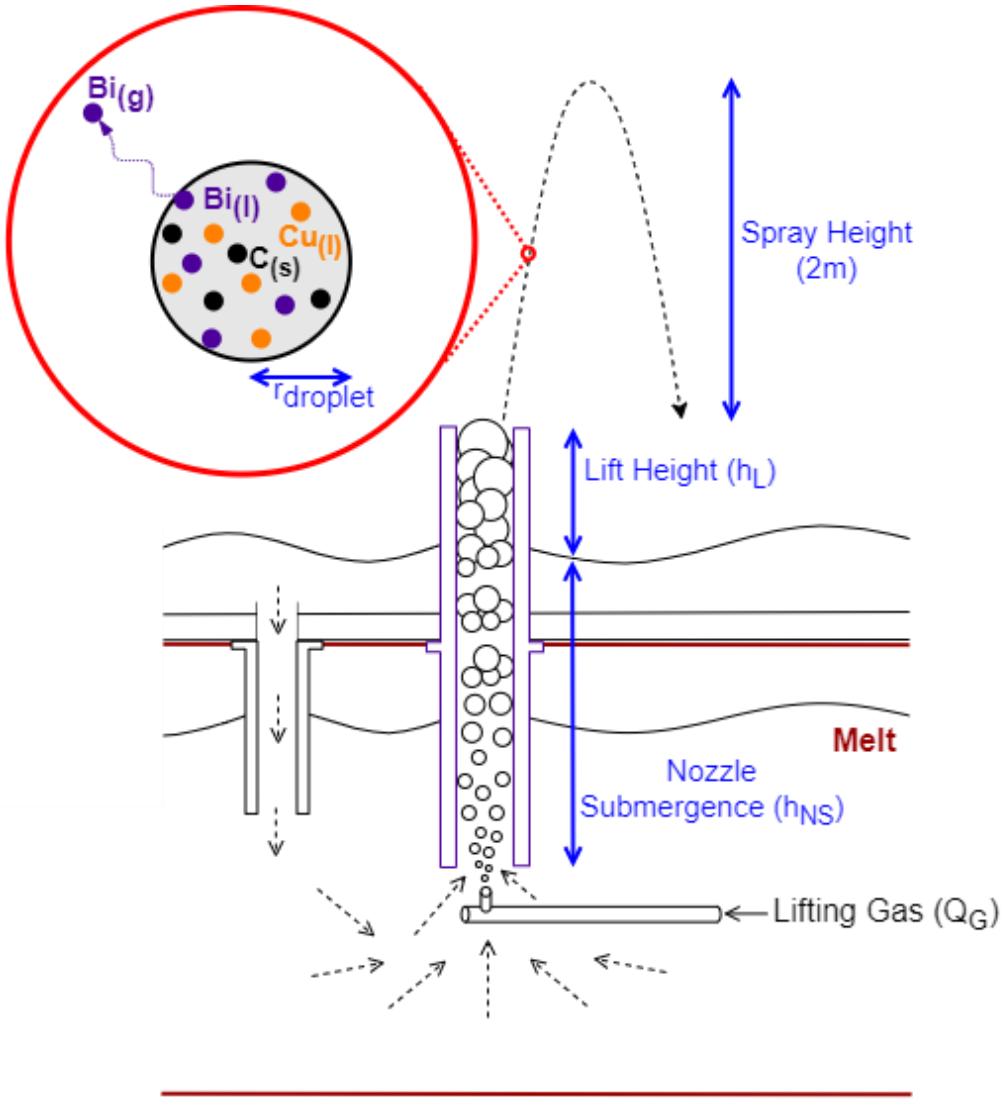

Figure 6: Riser geometry and droplet flight path

A spray height of 2m is assumed, based on Allaire's (1991) interviews with operators of RH degassing units. An analytical model for the maximum height of droplets would be challenging to develop due to the rapid expansion of gasses under vacuum which causes an increase in the actual liquid velocity near the top of the riser. Additionally, the mass transfer of bismuth into the lift gas bubbles can also contribute to an

increase in their size. The time of flight from the top of the parabola to the bottom (a distance of h = 2m) is calculated using the kinematic equation for a free-falling object:

$$h = v_i t + 0.5gt^2 \quad \text{Eq 23}$$

where v_i is the initial velocity in m/s (v_i=0 at the top of the parabola), t is the flight time (s), and g is the acceleration due to gravity (m/s^2). Since the droplets take nearly the same time to rise to their maximum altitude and to fall down to the base of the vacuum chamber, the total droplet exposure time is given by:

$$t_e \approx 2t = 2\sqrt{\frac{2h}{g}} \quad \text{Eq 24}$$

Equation 24 may underpredict the actual flight time of droplets if the lift height of the riser h_L above the liquid level in the vacuum chamber is significant. The liquid level in the vacuum chamber, and hence h_L, can be controlled by injecting lifting gas into the downleg through which the molten mixture drains back into the melt crucible (Allaire, 1991).

Lee (1988) studied spray generation by gas lift pumps using a pilot scale nitrogen-water system and found that the reduced top pressure of the riser causes gas bubbles to expand as they approach the top of the riser, thus increasing the void fraction near the top. Similarly, increasing the volumetric flow rate of the gas (Q_G) causes an increase in J_L until J_L eventually reaches a maximum beyond which further increase with Q_G has no effect (Tighzert et al., 2013). This is because at very high volumetric flow rates of gas, large gas slugs form that cannot maintain their shape and stability, thus preventing the liquid from moving forward effectively (Tighzert et al., 2013). Consequently, there is an optimum Q_G that results in a maximum J_L for gas lift pumps.

Additionally, studies found that increasing the nozzle submergence (h_{NS} in Figure 6) can increase the rate of bismuth removal (Lee, 1988). The nozzle submergence is the distance from the bottom of the riser to the

surface of the melt in the crucible. Increasing h_{NS} allows more distance for the bubbles to travel, expand, and coalesce, thus increasing the superficial gas and liquid velocities. Therefore, the melt crucible should be made as deep as the volume of the melt will allow, while maintaining a diameter large enough to allow for proper riser spacing. The lift ratio, β, can also be used to optimize the design of the riser:

$$\beta = \frac{h_L}{h_L + h_{NS}} \qquad \text{Eq 25}$$

Lee's experiments found that an optimum lift ratio between 0.1 and 0.3 allows for the fastest rate of refining.

Figure 7 from Allaire (1991) plots J_G versus J_L from Lee's experiments with a nitrogen-water system 1/5th of industrial size (Lee, 1988). This figure is used to determine the required J_G for a selected value of J_L at a lift ratio (β) of 0.1 to 0.3. In this work, J_L is specified in the design of the apparatus and J_G is estimated using Figure 7.

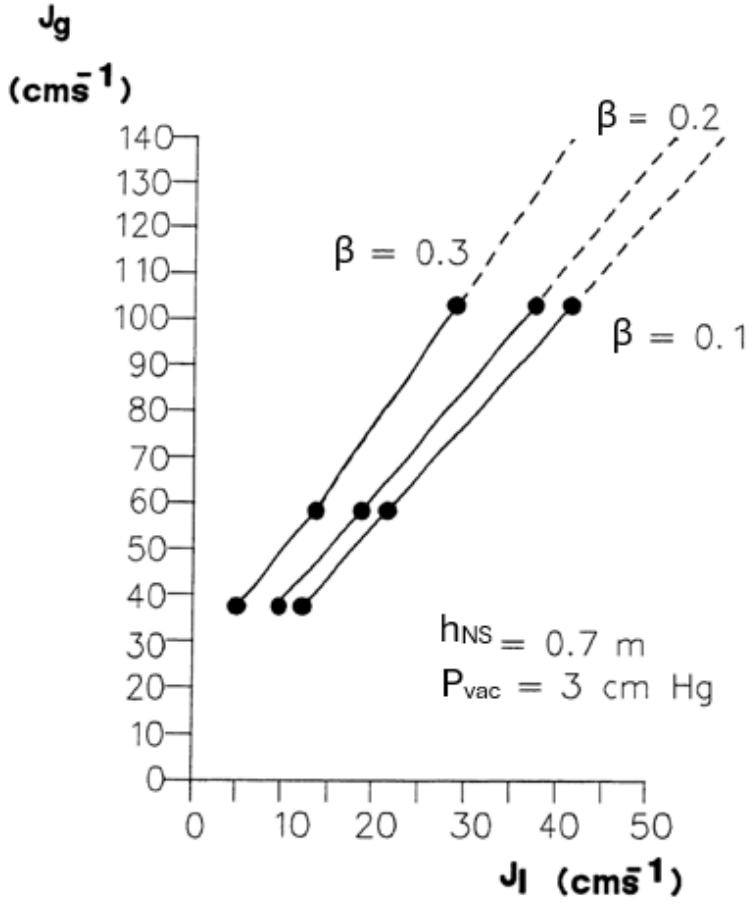

Figure 7: Superficial gas velocity versus superficial liquid velocity in riser leg (Allaire, 1991)

The droplet radius in the vacuum chamber is assumed to be uniform and equal to half the maximum droplet diameter, d_{max} (m) given by:

$$d_{max} = 4\left(\sigma/_{g\Delta\rho}\right)^{0.5} \qquad \text{Eq 26}$$

where σ is the surface tension in N/m and $\Delta\rho$ is the difference in density (kg/m^3) between the liquid and vapour phases (Allaire, 1991). The assumption that the droplets are all of maximum size leads to a

conservative estimate of the available surface area for mass transfer. The surface tension of a binary metal liquid alloy composed of components Cu and Bi is calculated using Butler's method (Butler, 1932):

$$\sigma = \sigma_{Cu} + \frac{RT}{\mathcal{A}_{Cu}} ln \frac{\gamma_{Cu}^{s}}{\gamma_{Cu}^{b}} + \frac{RT}{\mathcal{A}_{Cu}} ln \frac{1 - X_{Bi}^{s}}{1 - X_{Bi}^{b}} = \sigma_{B} + \frac{RT}{\mathcal{A}_{Bi}} ln \frac{\gamma_{Bi}^{s}}{\gamma_{Bi}^{b}} + \frac{RT}{\mathcal{A}_{Bi}} ln \frac{1 - X_{Bi}^{s}}{X_{Bi}^{b}} \quad \text{Eq 27}$$

where superscripts b and s represent the bulk phase and surface phase, respectively. The surface tension of the molten metal is a function of the surface tension of pure components (σ_{Cu} and σ_{Bi}, N/m), the molar surface area of pure component i ($\mathcal{A}_i$, J.mol^{-1}), the activity coefficients of component i in the bulk and surface phases γ_i^b and γ_i^s, and the mole fraction of component i in the bulk and surface phases, respectively (X_i^b and X_i^s). The surface tensions of pure copper and bismuth are calculated using Equations 28 and 29, respectively (Matsumoto et al., 2005., Database of Thermophysical Properties of Liquid Metal Coolants for GEN-IV, n.d.).

$$\sigma_{Cu} = 1.257 - 2.0x10^{-4}(T(K) - 1356) \qquad 1287<T(K)<1998 \qquad \text{Eq 28}$$

$$\sigma_{Bi} = 0.4208 - 8.1x10^{-5}\big(T(K)\big) \qquad 545<T(K)<1400 \qquad \text{Eq 29}$$

The molar surface area $\mathcal{A}_i$ is calculated by:

$$\mathcal{A}_i = 1.091 N_o^{1/3} V_i^{2/3} \quad \text{Eq 30}$$

where N_O is Avogadro's number (6.022x10^{23}) and V_i is the molar volume of component i (m^3/mol). The molar volume is calculated by:

$$V_i = \frac{M_i}{\rho_i} \quad \text{Eq 31}$$

where M_i and ρ_i are the molar mass (kg/mol) and density (kg/m^3) of the pure component, respectively. The density of liquid bismuth can be calculated for range of temperatures from 545K to 1837K by (Catalan & Rezaei, 2022):

$$\rho_{l,Bi} = 10698 - 1.2064\,T(K) \quad \text{Eq 32}$$

The density of liquid copper can be calculated for a temperature range from 1356K to 2500K by (M.J. Assael et al., 2010):

$$\rho_{l,Cu} = 7997 - 0.819(T - 1357.8) \quad \text{Eq 33}$$

The activity coefficients of the bulk and surface phases are related by:

$$\gamma_i^s = \left(\gamma_i^b\right)^\beta \quad \text{Eq 34}$$

where β =0.83 for liquid alloys (Speiser et al., 1987; Tanaka & Hack, 2001; Yeum et al., 1989). In this work, γ_i^b is taken as unity for both pure metal components, which assumes an ideal solution due to the lack of more specific knowledge about the thermodynamics of Cu-Bi solutions. The surface tension is calculated by adjusting the value of X_B^s until both parts of Equation 27 are equal.

2.1.7. Scale-up of Process

The rate of bismuth mass transfer (r_{Bi}, Eq 17), which controls the removal of bismuth, can be inserted into the mass balance equation for a batch reactor (Eq 35) to obtain a model for the rate of bismuth removal:

$$\frac{dm_{Bi}}{dt} = -r_{Bi} \quad \text{Eq 35}$$

where m_{Bi} is the mass of bismuth in the melt (kg_{Bi}), and t is the processing time (s). Since r_{Bi} is a function of C_{Bi}^{B} (the bulk concentration of bismuth in the melt), and C_{Bi}^{B} changes as bismuth is removed, so does the volume of the melt. Equation 36 accounts for the changing volume of the melt,

$$V_{melt} = V_0 - \left[\frac{m_{Bi,0} - m_{Bi,t}}{\rho_{Bi}}\right] \quad \text{Eq 36}$$

where V_0 is the initial volume of bismuth and copper to be treated and $m_{Bi,0}$ is the initial mass of bismuth. Combining Equations 17, 35, and 36 with $C_{Bi}^{B} = m_{Bi}/V_{melt}$ yields the rate of bismuth removal:

$$\frac{dm_{Bi}}{dt} = -KA_{droplets}m_{Bi}\left[V_0 - \frac{m_{Bi,0} - m_{Bi,t}}{\rho_{Bi}}\right]^{-1} \quad \text{Eq 37}$$

which can be integrated using numerical methods such as fourth order Runge-Kutta algorithm, which may be implemented in software environments like Excel, Matlab, or Python. Figure 8 illustrates the changes in surface tension and melt surface area as the mixture is processed. The surface tension increases as bismuth is removed, and since the droplet diameter increases with surface tension (Eq. 26), this results in a decrease of the total surface area of the droplets for a given liquid flow rate being sprayed. Eventually both parameters approach a maximum or minimum value after most of the bismuth has been removed from the melt. Overall, the mass transfer area decreases with processing time, which negatively affects the efficiency of bismuth removal from the melt.

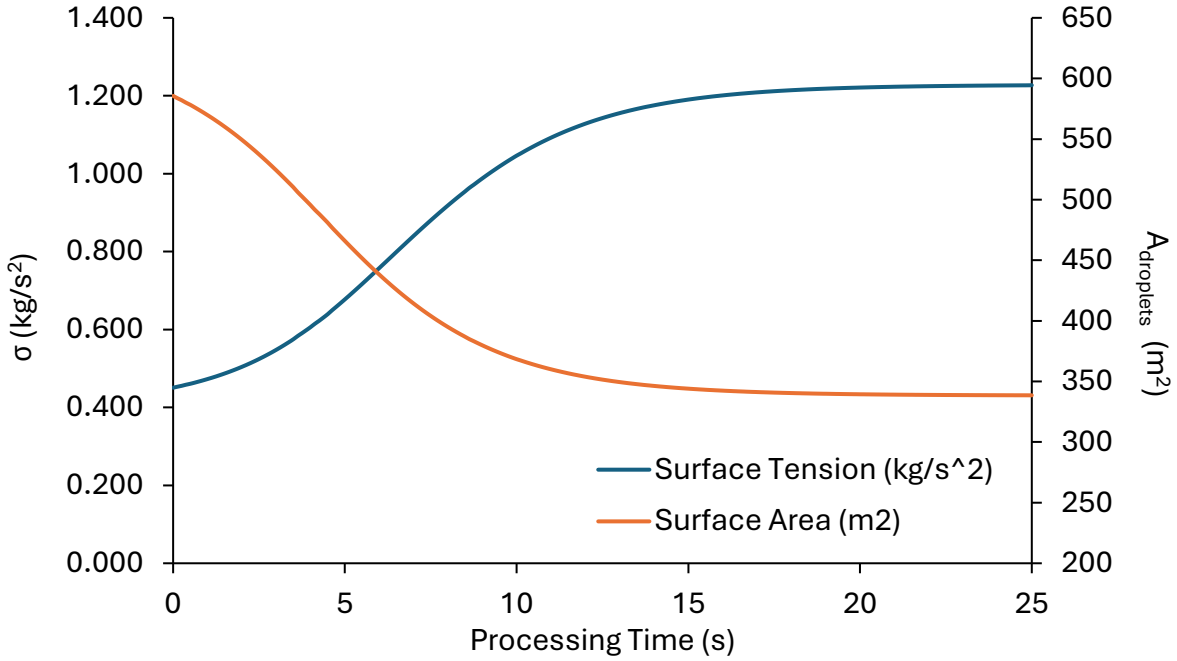

Figure 8: Change in surface tension and surface area versus time [T=1500 K, P=30 Pa, riser diameter=0.4 m, 14 risers, J_L=0.5 m/s, J_G=1.2 m/s, Initial mass fractions X_{Bi}=0.7, X_{Cu}=0.13, X_C=0.17]

2.2. Solids Processing

After bismuth removal, the solid carbon is still contaminated with molten copper metal. A wet granulation process, such as those used for slag granulation in steelmaking, can be used to solidify the product into uniform particles. The particles can then be ground into a smaller particle size, which will allow for faster copper leaching kinetics in the next step of carbon purification (See Section 2.3).

2.2.1. Wet Granulation

Figure 9 illustrates the wet granulation and dewatering process adapted for this work. The molten copper and carbon mixture leaving the vacuum distillation process travels along a hot runner that is angled to promote flow of the material. Below the runner is the granulation tank with water jets flowing co-currently

to the flow of molten copper and carbon. The molten copper and carbon are dropped from the hot runner into the water jets that break up the molten solids into fine particles with an average size of 1mm (Leyser & Cortina, 2006). A mass ratio of 1:10 for solids to water is suggested for effective granulation (*Granulated Blast Slag (GBS)*, 2024). The solidification time of the particles depends on the size of the droplets and the temperature difference between the molten slag and the granulation water (Leyser & Cortina, 2006). Studies on blast furnace slag granulation suggest that the mixture of molten copper, solid carbon and water must be processed for at least 30 seconds for the solids to break up into smaller particles while cooling down at the same time (Van Stein Callenfels & Van Ikelen, 2003). However, further research should be conducted on the solidification time of the copper and carbon mixture, as opposed to blast furnace slag. Copper is an excellent heat conductor and will likely require a lower processing time. However, 30 seconds serves as a conservative estimate in this work to ensure that particles are broken up and cooled sufficiently.

Different heat transfer mechanisms have been postulated based on the temperature of the granulation water and turbulence of the mixture. Cold granulation water with good turbulence between the slag and water allows for an optimum removal of heat without steam release. The high turbulence allows for any local steam generated to be condensed upon contact with cold granulation water. More commonly, cold water granulation with some steam release can occur at high slag flows. In these cases, a stainless steel stack is placed above the granulation tank to remove vapours from the system. The last heat transfer mechanism is heat removal by steam generation, wherein the circulating water is about 90-95 °C (Leyser & Cortina, 2006). The molten media cools by supplying the latent heat of vaporization to the hot water. In a cold-water system, the large quantities of water consumed will need to be cooled in a cooling tower before recirculation. On the other hand, water in the hot water system can be recirculated directly and requires less makeup water to account for losses due to steam generation. However, hot water systems have been found to wear and corrode at a faster rate than cold water systems (Van Stein Callenfels & Van Ikelen, 2003). A cold water system is suggested in this work for the granulation of copper and carbon.

After processing, a dewatering unit reduces the moisture content of the granulated particles to about 10-12 wt% (Mcdonald & Werner, 2015). Figure 9 illustrates a cross section of the dewatering drum, for which the outer wall is a screen that allows water to pass. The mixture of water and granulated particles is fed to the drum. The inner walls of the drum have vanes which help scoop up the granulated particles as the drum rotates. As the granulated particles are raised by the drum rotation, water is removed, and the dewatered granules are dropped onto a conveyor belt which removes them from the process. Near the top of the dewatering drum is a purge air jet to help remove granulated particles from the drum. After granulated particles are dropped onto the conveyor belt, a purge water jet helps clear any particles stuck to the screen as it rotates (Leyser & Cortina, 2006). Particles removed by the conveyor belt can be transported by a bucket or screw conveyor to the grinding process.

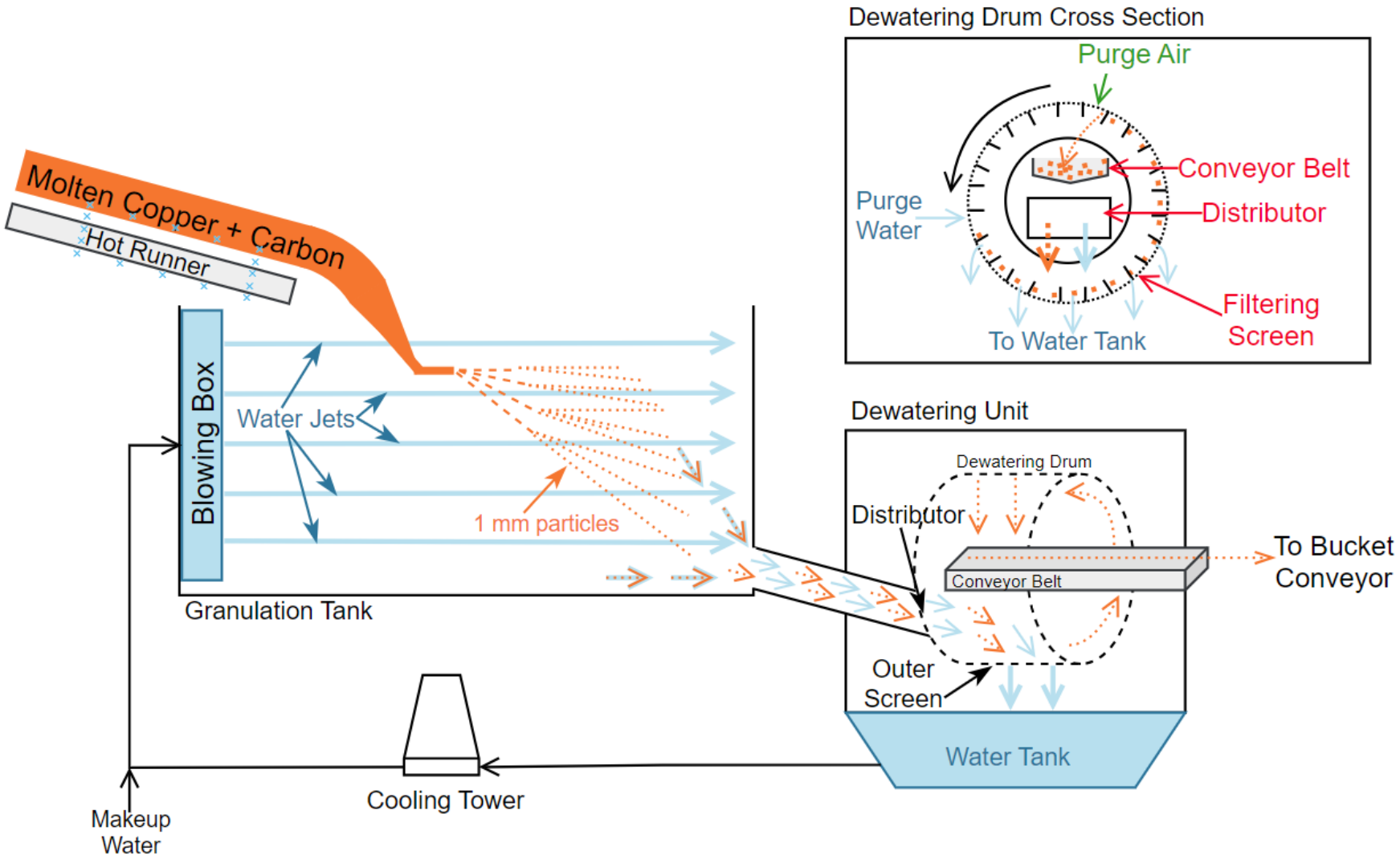

Figure 9: Wet granulation and dewatering unit (Adapted from Paul Wurth) ("INBA System Slag Granulation with Continuous Dewatering and Pollution Control," 2015; Leyser & Cortina, 2006)

2.2.2. Grinding

The purpose of grinding is to reduce the granulated particles to a fine particle size that will speed up the leaching kinetics by increasing the available surface area of copper in the leaching reactor downstream. In agitation leaching processes of copper ore, a feed particle size of about 150 μm is used (Schlesinger & Mark E, 2011). While the actual grinder product size required can be optimized in the design of the leaching vessel, a stirred mill can be used to achieve a reduction in particle size at this order of magnitude. The reduction ratio (R_{red}, Eq 38) can also be used to guide the selection of grinding equipment, where F_{80} and P_{80} are the screen opening sizes that would let 80 wt% of the feed and ground material pass, respectively. Reduction in particle size in this process from 1 mm to 100 μm corresponds to R_{red}=10. The maximum R_{red} achievable by a stirred mill is 100, which makes it an excellent fit for this application (Metso Outotec, 2021). Metso's Vertimill stirred mill can handle feeds as coarse as 6mm and can grind products down to a particle size of 20 microns (*Vertimill*, 2024).

$$R_{red}=\frac{F_{80}}{P_{80}} \qquad \text{Eq 38}$$

Stirred mills are a well-established technology in the mineral processing industry. A vertical screw is suspended in the grinding chamber (Figure 10), which rotates to stir a fluidized feed mixture. The grinding media such as steel or ceramic balls) grind the feed using forces of impaction, compression, shearing, and attrition. Industrial stirred mills take a slurry feed consisting of 40-50% solids by weight (Metso Outotec, 2021). The grinding media is typically 12-50 mm in diameter, depending on the desired product size (Metso Outotec, 2021). Smaller grinding media allows for more surface area to facilitate grinding, thus improving efficiency. Stirred mills can be filled with up to 70% by volume grinding media, which is an improvement from horizontal ball mills which take 35-50% by volume grinding media to allow for void space for tumbling (Metso Outotec, 2021; Schlesinger & Mark E, 2011; *Stirred Mills* , 2024).

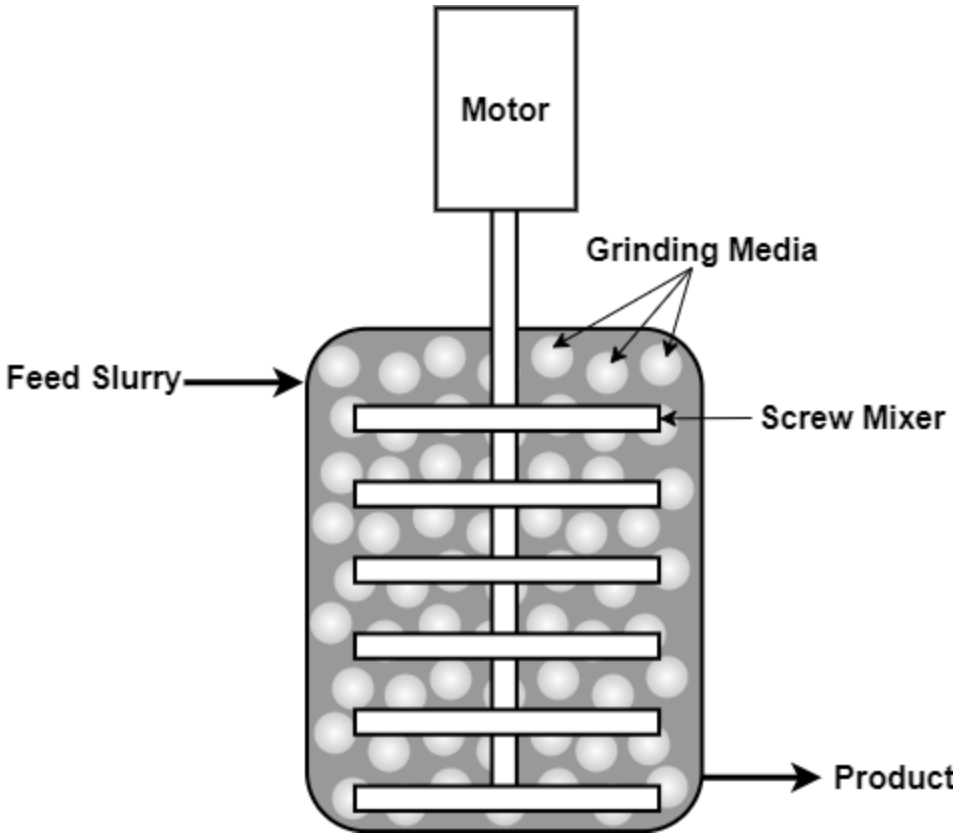

Figure 10: Stirred mill grinder conceptual drawing

The most common formula for estimating the specific power consumption of a grinder (W, kWh/sht) is the Bond formula (Metso Outotec, 2021):

$$W = 10 * W_i \left(\frac{1}{\sqrt{P_{80}}} - \frac{1}{\sqrt{F_{80}}} \right) \quad \text{Eq 39}$$

where W_i (kWh/sht) is the Bond's work index, where sht stands for short ton (sht=2000 lbs). Typically, the Bond's work index is calculated from ball-mill experimental data by:

$$W_i = \frac{44.5}{P_{100}^{0.23} GPR^{0.82} \left(\frac{10}{\sqrt{P_{80}}} - \frac{10}{\sqrt{F_{80}}} \right)} \quad \text{Eq 40}$$

where P_{100} is the 100% passing size of the product, and GPR is the average grams of ground product that passes through a selected mesh size per revolution of the last three experimental cycles. W_i for common minerals can be obtained from the literature; however, no information exists for the work index of the granulated product containing copper metal and carbon in this process. Haffez (Haffez, 2012) studied the correlation between the Bond work index and the mechanical properties (including harness, abrasion, compressive strength, and modulus of elasticity) of various ores of a range of Bond's work indices. While all of the properties studied exhibited some correlation to the Bond's work index, the modulus of elasticity (λ, GPa) was found to have the strongest correlation to W_i, with a correlation coefficient of 90% in the following equation:

$$W_i = 6.3Ln(\lambda) - 10.6 \qquad \text{Eq 41}$$

Material properties of annealed copper are used to estimate the properties of the granulated particles, estimated to have λ=121-133 GPa (*Copper, Cu; Annealed*, 2024). This corresponds to a W_i range of 19.61 – 20.21 kWh/sht. The average is taken as the best guess for W_i of the granulated particles, W_i=19.9 kWh/sht. For reference, the W_i of some other common materials include copper ore (W_i=12.72 kWh/sht), coke (W_i=15.13 kWh/sht), and silicon carbide (W_i=25.87 kWh/sht) (Metso Outotec, 2021). Based on F_{80}= 1 mm ($1x10^3$ μm) and P_{80}=100 μm, the estimated power consumption (W) of the ball mill is 21.54 kWh/sht or 23.74 kWh/tonne of dry solids. This level of power consumption is within the specified range of 3-25 kWh/t for Metso's Vertimill stirred mill grinder (*Vertimill*, 2024).

2.2.3. Rotary Drum Vacuum Filtration (RDVF)

Rotary drum vacuum filters (RDVF's) are effective at separating fine particles of 5 – 300 μm in size from slurries (Micronics Engineered Filtration Group, 2025). In this process, a RDVF is required to separate solid particles after leaching the copper and after cementation. Figure 11 illustrates the overall concept of

the RDVF, where a drum coated in a filter medium such as cloth or screen is submerged in the slurry to be separated. A vacuum is applied to the inside of the vacuum-drum, such that the slurry particles form a cake on the outside of the drum as the slurry liquid is sucked into a duct inside the drum. As the drum rotates, the filter cake passes through a filtration-deliquoring zone, one or more washing zones, then a final deliquoring zone before the solid cake is removed from the outside of the drum. In the washing zone, wash water is sprayed onto the cake to help with the removal of entrained species from the slurry liquid. Depending on the properties of the cake, different cake discharge methods are available, such as string, roll, and pre-coat discharge. The filtration angle, $\alpha_{filtration}$, varies with the immersion depth (E) of the drum in the slurry. The angle of the washing zone ($\alpha_{washing}$) can vary from 75-120° (Aspen Technology, 2023). The standard angle of the deliquoring zone is 60° (Aspen Technology, 2023). The sum of $\alpha_{ffiltration\text{-}deliquoring,}$ $\alpha_{washing,}$ and $\alpha_{deliquoring}$ must not be greater than the available surface area of the filter, which decreases as the immersion depth increases. Additionally, some surface area must be left for α_{non}, the angle without vacuum.

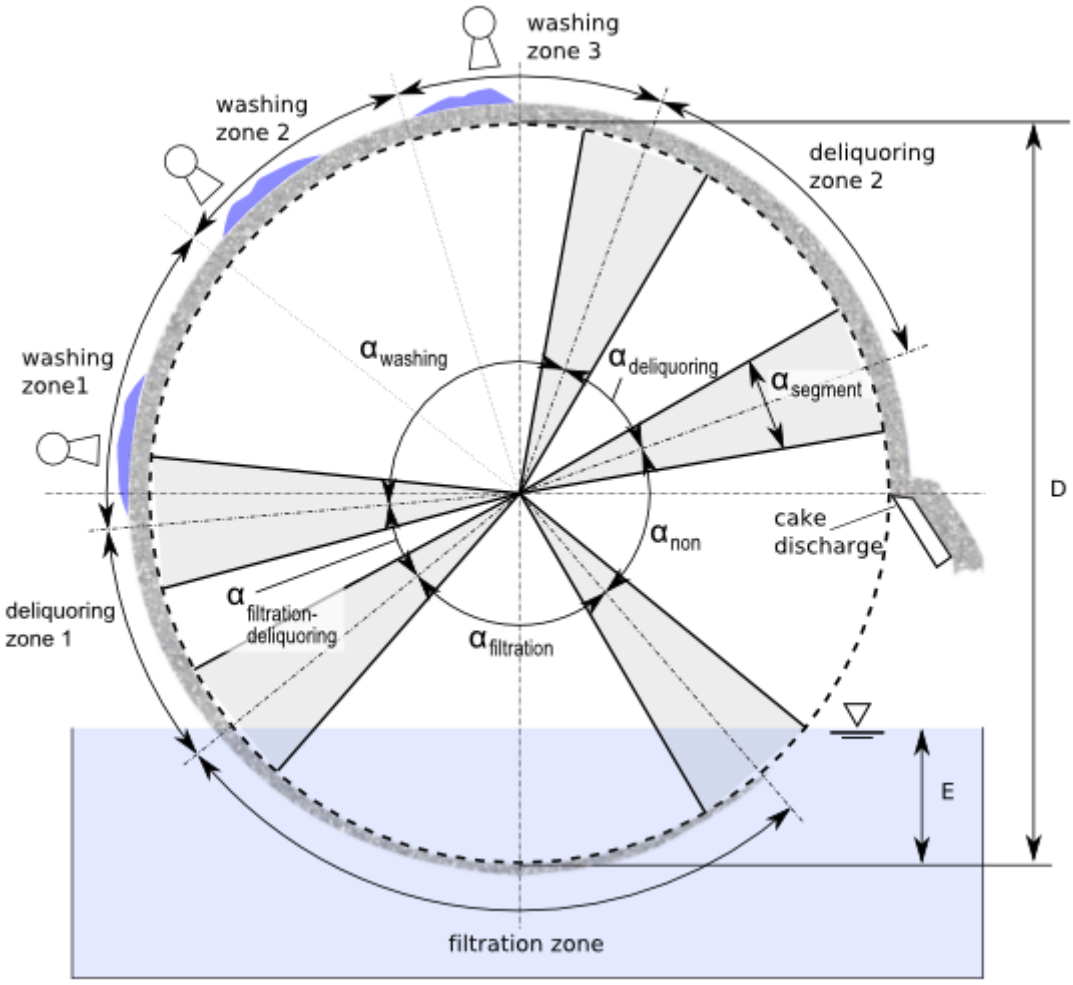

Figure 11: Oliver-type rotary vacuum-drum filter (Aspen Technology, 2023)

2.2.3.1. RVDF Sizing & Energy Consumption

Sizing the RVDF requires knowledge of the mass balance around the unit, such as the feed flow rate and solids concentration, the filtrate flow rate, the wet cake discharge rate, and the filter cake moisture content (Walker, 2017). The filter cake moisture content is a function of the physical properties of the slurry and can be determined precisely by experiments using the actual mixture to be filtered. For preliminary estimates, a filter cake moisture content ranging from 32 to 36 wt% moisture is reasonable (Walker, 2017).

Filtrate flux rate ($J_{filtrate}$) is the rate of flow of filtrate per unit filtration area in $kg/m^2/hr$ and is normally determined by test work using the slurry to be filtered. Filtrate flux rates can vary within an ideal operating window with values around 420 to 510 $kg/m^2/h$ (Walker, 2017). $J_{filtrate}$ and the filtrate flow rate, $\dot{m}_{Filtrate}$, can be used to calculate the filter surface area (A_{filter}) as follows:

$$A_{filter}\left(m^2\right)=\frac{\dot{m}_{Filtrate}}{J_{filtrate}} \qquad \text{Eq 42}$$

The RDVF motor consumes power proportionally to the area of the filter. Manufacturers of RDVF's provide sizing charts with estimated motor power for various filter sizes (*Vacuum and Pressure Drum Filters, YU and PYU*, 2024).

2.3.Copper Removal by Leaching

2.3.1. Copper Leaching Vessel

After vacuum distillation, granulation, and grinding, the carbon remains contaminated with metallic copper. Copper can be dissolved in oxygenated sulfuric acid solution as follows:

$$Cu_{(s)} + 2H^+ + 0.5O_2 \rightarrow Cu^{2+} + H_2O \qquad \text{Eq 43}$$

Figure 12 illustrates the proposed leaching vessel for the dissolution of copper. The solid mixture of carbon and metallic copper is fed to the vessel, along with a sulfuric acid solution. An aerated mixing mechanism can be used wherein air is injected at the top of the shaft and exits through the impeller blades to ensure that the vessel is uniformly aerated. The copper removal process is analogous to ore leaching processes used in mineral processing industries (Schlesinger & Mark E, 2011). The outlet of the leaching vessel is a slurry consisting of solid carbon in an aqueous solution of Cu^{2+}, SO_4^{2}, HSO_4^{-}, H^+, and OH^-. The solid carbon is later separated using a RDVF, as described in section 2.2.3.

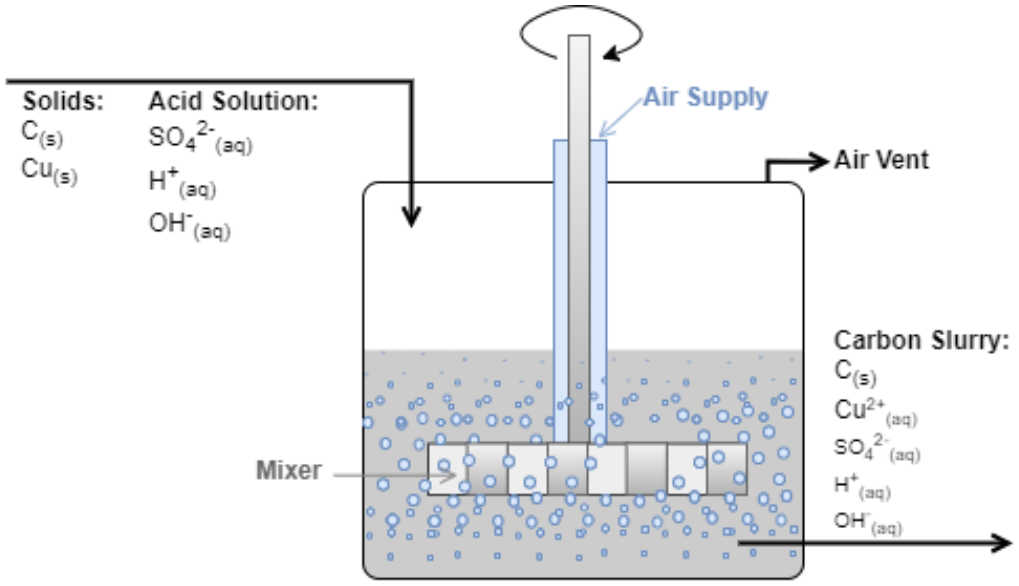

Figure 12: Copper leaching vessel conceptual diagram

2.3.2. Kinetic Model

Lu & Graydon (1953) conducted experiments to develop a kinetic model for the dissolution of copper metal in a sulfuric acid solution maintained at a pH of 1. The concentration of sulfuric acid that is needed in the leaching reactor feed to maintain the pH equal to 1 inside the reactor is calculated in Appendix D. The kinetic model is as follows:

$$r_{Cu^{2+}} = \frac{d[Cu^{2+}]}{dt} = 1.36 \times 10^3 e^{-(58994/RT)} (P_{O_2})^{0.5} \left(\frac{A_{Cu}}{V_L}\right) [Cu^{2+}]^{0.5} \quad \text{Eq 44}$$

where $r_{Cu^{2+}}$ is the rate of Cu^{2+} production (mol $Cu^{2+}/m^3/s$), $[Cu^{2+}]$ is the concentration of Cu^{2+} in the aqueous phase of the reactor (mol/m^3), P_{O_2} is the partial pressure of oxygen (atm), A_{Cu} is the surface area of copper in the reactor (m^2), and V_L is the volume of solution (m^3) inside the reactor. Validation of the kinetic model against the experimental data of Lu & Graydon (1953) is shown in Appendix E.

2.3.3. Leaching Reactor Sizing

Since the leaching reactor is assumed to behave as a CSTR, its material balance equation is:

$$F_{Cu^{2+}_{out}} - F_{Cu^{2+}_{in}} = V_L r_{Cu^{2+}} \quad \text{Eq 45}$$

where V_L (m^3) is the volume of liquid in the reactor, and $F_{Cu^{2+}_{out}}$ and $F_{Cu^{2+}_{in}}$ are the molar flow rates of Cu^{2+} at the outlet (mol/s), and inlet of the reactor, respectively, both in mol/s. Because all the copper entering the reactor is solid, $F_{Cu^{2+}_{in}} = 0$. Substitution of the kinetic model (Equation 44) in Equation 45 and further development shown in Appendix F yields:

$$V_L = \frac{2.45 \times 10^{-4} e^{(58994/RT)} \rho_{Cu} r_i \dot{m}_c}{\left(\rho_L x_{s,i}\right)^{\frac{3}{2}} (1 - X_{Cu})^{\frac{2}{3}} (1 - y_{Cu,i})} \left(\frac{X_{Cu}}{P_{O_2} M_{Cu} y_{Cu,i}}\right)^{\frac{1}{2}} \quad \text{Eq 46}$$

where X_{Cu} is the fractional conversion of solid copper to cupric ions, M_{Cu} is the molecular weight of copper (kg/mol), P_{O_2} is the partial pressure of O_2 (atm), ρ_{Cu} is the density of copper (kg/m^3), r_i is the radius of copper particles in the feed stream (m), $\dot{m}_c$ is the mass flow rate of carbon (kg$_C$/s), R = 8.314 J/mol-K, T is the reactor temperature (K), $y_{Cu,i}$ is the mass fraction of copper in the incoming solid matrix (kg copper/kg solid), $x_{s,i}$ is the mass fraction of solid in the slurry entering the reactor (kg solid/kg liquid), and ρ_L is the density of the liquid. Equation 46 can be used to calculate the required solution volume for a specified X_{Cu} and feed conditions. Appendix G outlines the results of an Aspen Plus simulation used to check the underlying assumption that the liquid density remains nearly constant between the inlet and outlet of the reactor. The simulation results show that the liquid density increases from 1040 kg/m^3 in the feed to 1080 kg/m^3 at the outlet for a specific conversion and set of feed conditions. Hence, the error introduced by this assumption is acceptable for preliminary design estimates.

As the leaching reaction progresses, the particles decrease in size as a function of the copper conversion $X_{Cu(s)}$ and the particle radius size of the feed r_i:

$$r_f = r_i * \left(1 - X_{Cu(s)}\right)^{\frac{1}{3}} \quad \text{Eq 47}$$

where the r_i is based on the P_{80} size leaving the grinder and $X_{Cu(s)}$ is specified in the design of the leaching vessel.

2.4. Carbon Drying

After the copper leaching process, the only remaining solids in the mixture are fine carbon particles. Studies of the carbon produced by methane pyrolysis have found the spherical particles to be 20-50 nm in diameter and aggregating in chains or more complex geometries of 100-200 nm in size (Rahimi et al., 2019). The particles can be separated from solution using a rotary drum vacuum filter, as described in section 2.2.3. Prior to separation, the carbon particles should be rinsed with water to remove any remaining ions from the leaching solution. Last, the carbon must be dried to meet market standards for carbon black. The estimated moisture content of solids leaving the rotary drum vacuum filter is approximately 32 – 36 wt%, as mentioned in section 2.2.3. An example of the maximum moisture content of carbon black pigment on the market is 1.5 wt % (DCL Corporation, 2020). A rotary dryer can be designed to lower the moisture content so the product is ready to be sold on the market.

2.4.1. Dryer Selection

Rotary dryers can operate on a batch or continuous basis. A cylindrical shell is rotated upon bearings and is slightly inclined with respect to the horizontal. Wet feed is introduced at the upper end of the dryer, and it dries as it progresses through the length of the shell. The shell rotates to improve air flow around the particles and can be equipped with flights on the inner walls to assist with lifting and showering solid particles within the vessel to promote contact between solids and hot gasses. Direct-contact dryers have hot gasses (such as air) flowing through the shell in contact with the particles to be dried. Indirect-contact dryers do not have contact between the heating medium and the product being dried; instead the wet material is heated by conduction through contact with a heated surface such as the wall of the dryer. Indirect rotary dryers are suitable for processes that require special gas atmospheres or exclusion of outside air (Mujumdar, 2006). The flow of air can also be co-current or counter-current to the flow of feed material. Co-current flow is used for heat sensitive materials, whereas counter-current flow is desirable to take advantage of the

higher thermal efficiency that can be achieved. A direct contact co-current rotary dryer (Figure 13) is proposed for drying the carbon black of this process. Direct contact co-current rotary dryers are used to avoid the possibility of ignition in coal rotary dryers, which contain materials of similar composition to the carbon black of this process (Mujumdar, 2006). The hot air feed can be heated by exchanging heat with steam or by heat integration with other process streams or flue gas. Carbon dust entrained in the moist outlet air can be separated using a bag filter or other appropriate means for such small particles.

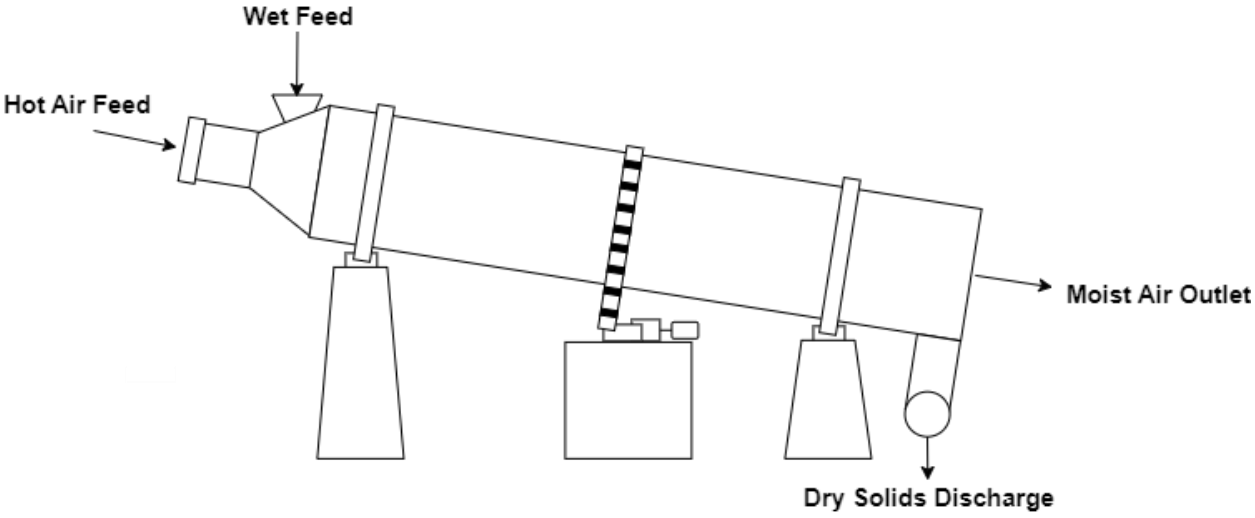

Figure 13: Simplified diagram of a direct contact co-current rotary dryer. Adapted from (Mujumdar, 2006).

2.4.2. Dryer Sizing

The rate of drying depends on several heat and mass transfer mechanisms. Heat is transferred from the hot air to the solid carbon and liquid water to raise them to the evaporation temperature of the water. Heat is also transferred to the heated water to provide the latent heat needed for evaporation. Last, heat is transferred to the carbon and water vapour to heat them to their final temperatures. Mass transfer occurs as moisture is

evaporated from the surface of the solid. Additionally, internal moisture in the solid particles can transfer to the surface of the particles by capillary flow (Mujumdar, 2006).

Due to the novelty of the carbon product formed in this process, characteristic drying curves are not yet available in the literature. A drying rate curve is determined by measuring the moisture content loss as a function of time. When the drying rate curve is determined for a range of conditions, the curves can be normalized with respect to the initial drying rate and average moisture content, then a single "characteristic drying rate curve" can be approximated for a single substance (Mujumdar, 2006). The characteristic drying rate curve is used to predict the rate of drying according to the moisture content when designing dryers. Without the drying rate characteristic curve for the carbon product, only preliminary design estimates can be made using empirical knowledge from literature and the mass & energy balance.

Rotary dryers can be rated in terms of the number of heat transfer units (N_T) they contain. Studies of industrial rotary dryers have found that N_T should be in the range of 1.5 to 2.5 for efficient operation. N_T is defined by:

$$N_T = \ln \frac{T_1 - T_W}{T_2 - T_W} \qquad \text{Eq 48}$$

where T_1 is the inlet gas temperature (K), T_2 is the outlet gas temperature (K), and Tw is the wet-bulb temperature of air at the inlet (K). The wet-bulb temperature is the lowest temperature to which air can be cooled by evaporating water into it. Typical inlet gas temperatures for co-current rotary dryers vary depending on the heating medium of the air. Steam-heated air is 400-450 K, and air heated by oil and gas fired burners is 800-1100K (Mujumdar, 2006). Typical co-current rotary dryer inlet gas ranges from 300 to 600 °C (Mujumdar, 2006). A psychrometric chart or calculator can be used to find Tw using T_1 as the dry bulb temperature and the humidity ratio of the air in kg water/kg dry air. A typical humidity ratio is 0.01 kg

water/kg dry air (Mujumdar, 2006), however this can vary depending on location, time of year, or other factors. Using this information, Equation 48 can be used to estimate T_2.

Figure 14 illustrates the parameters used to model the mass balance of water around the dryer by:

$$F_{DA}(Y_O - Y_{HA}) = F_S(X_i - X_O) \quad \text{Eq 49}$$

where F_{DA} and F_S are the flow rates (kg/h) on a dry basis of hot air and solids, respectively. Y_O and Y_{HA} are the absolute humidities (kg water/kg dry air) of air at the outlet and hot air inlet, respectively. X_O and X_i are the moisture content (kg water/kg dry solids) of solids at the outlet and the inlet of the dryer, respectively.

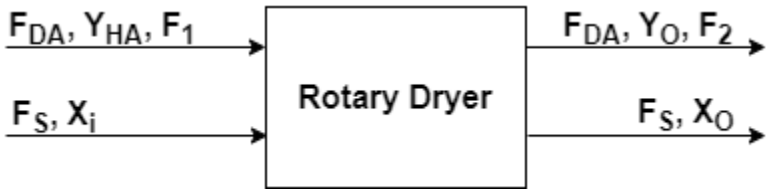

Figure 14: Mass balance around rotary dryer

F_1 and F_2 are the flow rates (kg/h) of moist air at the inlet and outlet and can be calculated by Equations 50 and 51.

$$F_1 = F_{DA}(1 + Y_{HA}) \quad \text{Eq 50}$$

$$F_2 = F_{DA}(1 + Y_O) \quad \text{Eq 51}$$

The heat duty of the rotary dryer (Q_T) is a summation of energy consuming processes, as shown by:

$$Q_T = (Q_{Solid} + Q_{Liquid} + Q_{Vaporization} + Q_{Final\ Temp})(1 + \xi) \quad \text{Eq 52}$$

where ξ represents the heat losses due to the convection between the outer surface of the dryer and the atmospheric air and especially, because of radiation, estimated to be about 7.5-10% (Mujumdar, 2006). Q_{Solid} is the energy required to heat the solids from the feed to the final temperature:

$$Q_{Solid} = \dot{m}_C C_{ps}(T_{SO} - T_S) \quad \text{Eq 53}$$

where $\dot{m}_C$ is the flow rate of dry carbon (kg/h), C_{ps} is the heat capacity of carbon, T_{SO} is the temperature of carbon at the outlet, and T_S is the temperature of carbon in the feed. Q_{Liquid} is the energy required to heat the water from the feed to the vaporization temperature:

$$Q_{Liquid} = \dot{m}_C X_S C_{pw}(T_{vap} - T_S) \quad \text{Eq 54}$$

where C_{pw} is the heat capacity of liquid water, T_{vap} is the vaporisation temperature of the water. $Q_{Vaporization}$ is the energy required to evaporate the water:

$$Q_{Vaporization=}\dot{m}_C \Delta H_{vap}(X_i - X_O) \quad \text{Eq 55}$$

where ΔH_{vap} is the latent heat of vaporization of water. $Q_{Final\ Temp}$ (Equation 60) accounts for energy used to heat the vapour to it's final temperature:

$$Q_{Final\ Temp=}\dot{m}_C(X_S - X_O)C_{pv}(T_{VF} - T_{vap}) \quad \text{Eq 56}$$

where C_{pv} is the heat capacity of water vapour.

After calculating Q_T, the dry air mass flow rate G (kg/h) can be calculated by:

$$G = \frac{Q_T}{C_{p,air}(T_1 - T_2)} \quad \text{Eq 57}$$

where $C_{p,air}$ is the heat capacity of air, T_1 is the inlet air temperature, and T_2 is the final air temperature.

The diameter of the dryer (m) can be calculated by (Mujumdar, 2006):

$$D = \sqrt{\frac{4G}{3600\pi ju}} \quad \text{Eq 58}$$

where u is the air mass velocity (kg/m^{2}s) which must be low enough to avoid entrainment of carbon in the air, so 0.556 kg/m^{2}s is a reasonable estimate from the lower range of allowable values (McCabe et al., 2004). j is a factor that accounts for the amount of free area available for the air to pass, about 85% (Mujumdar, 2006).

The volume of the dryer can be estimated by (Mujumdar, 2006):

$$V = \frac{\tau F_2}{H\rho_S} \quad \text{Eq 59}$$

where F_2 is the mass flow rate of the carbon product with the residual water (kg/h). H is the dryer holdup, for which values from 0.07-0.08 have been found to give good performance in industrial dryers. ρ_c is the density of the carbon (kg/m^3). τ is the retention time of the product (h), which is around 7 to 15 minutes for rotary dryers (Mujumdar, 2006).

Last, the length of the dryer is given by:

$$L = \frac{4V}{\pi D^2} \quad \text{Eq 60}$$

The L/D ratio should be between 4 and 10 for optimum performance (Mujumdar, 2006).

The preceding equations provide a preliminary estimate of dryer sizing for the proposed process. However, it is critical to acknowledge that estimates based on pilot plant data will yield different results than those based on empirical studies, as done in this work. Common practice has been to oversize dryers to account for the uncertainty in mathematical models (Mujumdar, 2006). However, a more optimized process in terms of energy efficiency and capital costs could be developed with additional testing, research & development.

2.5. Copper Recovery by Cementation

The filtrate leaving the rotary drum vacuum filter after copper leaching contains significant amounts of Cu^{2+} in aqueous solution, along with SO_4^{2-}. The cupric ions must be converted to metallic copper, Cu^0, which can be recycled back to the methane decomposition reactor (MDR) or sold. Recovering and recycling as much copper as possible is critical to improve the economic performance of the plant by reducing the need for makeup catalyst in the MDR.

Electrowinning is commonly used in the copper ore processing industry for copper recovery, where electrodes are inserted into a solution containing Cu^{2+} and copper metal deposits onto the cathode. Electrowinning requires several processing steps including liquid-liquid extraction of Cu^{2+} ions from the leaching solution, so it is ideal when producing large quantities of high-grade copper metal. However, in the context of carbon purification for methane decomposition in a liquid metal bubble reactor, a simpler process is desirable to minimize capital and operating costs.

Cementation is an electrochemical process wherein a more noble metal ion is precipitated from a solution of its salts by a metal higher in the electromotive series (Fisher & Groves, 1976). Hence, the cupric ions in leachate solution can be precipitated as cemented copper in the presence of metallic iron, as represented by:

$$Cu^{2+} + Fe^{0} \rightarrow Cu^{0} + Fe^{2+} \quad \text{Eq 61}$$

Studies on copper cementation have found that cemented copper is loose, porous, or powdery (Fisher & Groves, 1976). Kinetic studies have found that the cementation rate increases as the copper deposit grows on the iron surface, as they increase the cathodic reaction area (Fisher & Groves, 1976). However, when cementation takes place in a rotating drum reactor, the agitation causes the copper particles to break away from the iron surface, allowing random collisions of copper particles with each other and with the iron particles. As more cemented copper is produced, the cathodic reaction area in the cementation reactor increases, which increases the overall rate of cementation (Fisher & Groves, 1976).

2.5.1. Cementation Kinetics

Fisher and Groves (1976) conducted a kinetic study of copper cementation in a revolving drum reactor. Sixpenny finishing nails were selected as the source of iron, as they are fabricated out of a low alloy steel and are available in large quantities. For each experiment, 40 sixpenny finishing nails equating to 67.8 g and 148.8 cm^2 were used in $3.25x10^{-3}$ m^3 of liquid (Fisher & Groves, 1976). Batch reactor experiments were conducted to evaluate the effect of solid copper metal concentration on the rate of cementation by adding copper metal powder to the revolving drum reactor prior to starting the experiment. The rate of copper cementation (g m^{-3} min^{-1}) is assumed to follow first order kinetics, which is supported by the experimental data of Fisher and Groves (1976):

$$r = \frac{d[Cu^{2+}]}{dt} = -k[Cu^{2+}] \quad \text{Eq 62}$$

where $[Cu^{2+}]$ is the copper ion concentration in g/m^3, t is the time in minutes, and k is the cementation rate constant $\left(min^{-1}\right)$. The experimental data of Fisher and Groves is consistent with the integrated form of Equation 62 (Appendix H):

$$[Cu^{2+}]_t = [Cu^{2+}]_0 e^{-kt} \quad \text{Eq 63}$$

Using their experimental data, the value of k for each experiment was determined by minimizing the sum of squared errors (SSE) between the experimental data and model predictions of Equation 63. Figure H1 in Appendix H compares the experimental data with the model predictions for different initial amounts of metallic copper.

Since the surface area of iron affects the rate of cementation, the rate constant k can be expressed as the product of $A_{Fe,}$ the initial surface area of iron (cm^2), and k', the apparent rate constant $\left(cm^{-2}min^{-1}\right)$:

$$k = k' A_{Fe} \quad \text{Eq 64}$$

After calculating k for each experiment by fitting the experimental data to the predictions of equation 63, the apparent rate constant for each experiment can be calculated using $A_{Fe} = 148.8\ cm^2$.

The apparent rate constants for each experiment can be plotted versus $[Cu^0]$, the solid copper concentration (g/m^3), to obtain a correlation for k' as a function of $[Cu^0]$:

$$k' \times 10^6 = -5.399 \times 10^{-9}[Cu^0]^2 + 5.035 \times 10^{-4}[Cu^0] + 3.268 \quad \text{Eq 65}$$

where the initial cemented copper concentration for each experiment, $[Cu^0]$, is calculated by dividing the initial cemented copper mass in grams by the volume of liquid used in the experiment, 3.25×10^{-3} m^3. See Appendix H for the graph of k' versus $[Cu^0]$ in Figure H2.

In this work, the apparent rate constant, k', will be applied to the design of a continuous revolving drum cementation reactor. The CSTR mole balance equation for solid cemented copper is as follows:

$$[Cu^0]_{out} = \frac{-rV}{Q} \quad \text{Eq 66}$$

where $[Cu^{2+}]_{out}$ and $[Cu^0]_{out}$ are the concentrations of copper ions and cemented copper at the outlet of the reactor, respectively. The liquid flow rate Q (m^3/s) is assumed to stay constant between the inlet and outlet of the reactor. V is the volume of solution in the reactor (m^3), and r is the rate of cementation given by:

$$r = -k' A_{Fe} [Cu^{2+}]_{out} \quad \text{Eq 67}$$

Substituting Eq. 67 in Eq. 66 gives:

$$[Cu^{2+}]_{out} = \frac{[Cu^{2+}]_{in} Q + rV}{Q} \quad \text{Eq 68}$$

where $[Cu^{2+}]_{out}$ is the cupric ion concentration at the reactor outlet. Moreover, the mole balance on copper writes:

$$[Cu^{2+}]_{out} = [Cu^{2+}]_{in} - [Cu^0]_{out} \quad \text{Eq 69}$$

Substitution of Eq. 69 in Eq. 68 and rearranging yields:

$$\left(1 + \frac{k' A_{Fe} V}{Q}\right) [Cu^0]_{out} = \frac{k' A_{Fe} V}{Q} [Cu^{2+}]_{in} \quad \text{Eq 70}$$

Eq. 70 must be solved numerically for $[Cu^0]_{out}$ because k' is a function of $[Cu^0]_{out}$ by Eq. 65. The Excel Solver was used for this purpose.

2.5.2. Cementation Reactor Sizing

The cementation reactor sizing serves to determine which reactor volume will achieve a desired level of copper recovery, Cu_R, defined by:

$$Cu_R = \frac{[Cu^0]_{out}}{[Cu^{2+}]_{in}} \quad \text{Eq 71}$$

The amount of iron needed is calculated so that the ratio of iron mass to reactor volume matches the value of 143.79 $kg_{iron}/m^3_{solution}$ in the experiments of Fisher & Groves (1976). The surface area of iron in the reactor (A_{Fe}) depends on the dimensions of the scrap iron pieces. In this work, the iron is assumed to consist of 10-gauge iron wire cut into 1" lengths. These dimensions are comparable to those of the steel nails in the experiments of Fisher and Groves. A_{Fe} can be calculated as:

$$A_{Fe}(m^2) = 143.79\left(\frac{kg_{Fe}}{m^3{}_{solution}}\right) * V_{solution}\ (m^3) * A_{s,Fe}\left(\frac{m^2}{kg_{Fe}}\right) \quad \text{Eq 72}$$

where $A_{s,Fe}$, (m^2/kg) is the specific surface area of iron on a mass basis, given by:

$$A_{s,Fe} = \frac{A_{Fe,p}}{m_{Fe,p}} \quad \text{Eq 73}$$

where $A_{Fe,p}$ is the surface area of one cylindrical piece of iron, given by

$$A_{Fe,p} = 2\pi r_{Fe,p} L_{Fe,p} + 2\pi {r_{Fe,p}}^2 \quad \text{Eq 74}$$

where $r_{Fe,p}$ and $L_{Fe,p}$ are the radius and length of one piece of scrap iron. The mass of one piece of scrap iron, $m_{Fe,p}$ is given by:

$$m_{Fe,p} = \pi r_{Fe,p}{}^2 L_{Fe,p} \rho_{Fe} \quad \text{Eq 75}$$

Figure 15 illustrates the predicted copper recoveries as a function of liquid in the reactor.

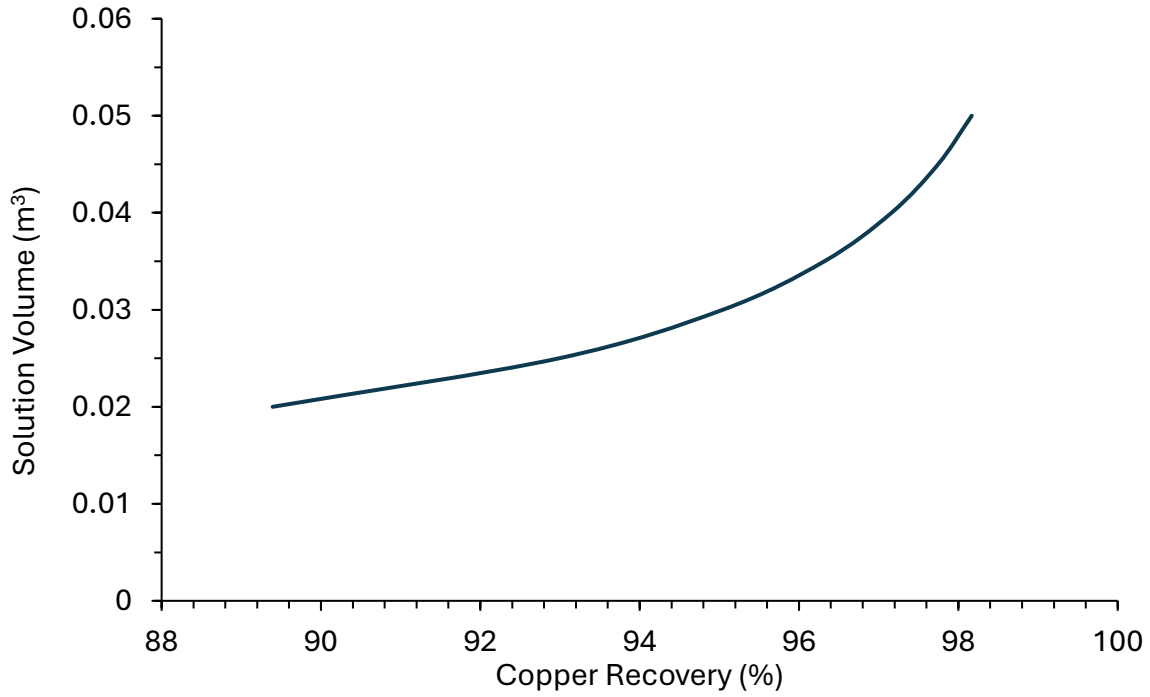

Figure 15: Solution volume versus copper recovery. [Q=6.5x10-5 m3/s, Cu2+,in=1600 g/m3, 10-gauge iron wire cut into 1" pieces]

The reactor volume must account for the volume of solution in the reactor, the volume of iron, and the void space in the reactor. The volume of solution V is specified as an input to equation 70, the volume of iron is calculated by:

$$V_{Fe} = \frac{A_{Fe}}{A_{S,Fe} \rho_{Fe}} \quad \text{Eq 76}$$

where $\rho_{Fe} = 7890 \frac{kg}{m^3}$ is the density of iron. The void space V_s is calculated using the experimental solution volume $V_{Exp} = 10\ gal$, and the actual drum volume $V_{drum\ Exp} = 12.24\ gal$ from the experiments of Fisher and Groves (1976):

$$V_s = 1 - \frac{V_{Exp}}{V_{drum\ Exp}} \quad \text{Eq 77}$$

where the void space = 0.183. The total cementation reactor volume is calculated by:

$$V_{cementation} = \frac{V + V_{Fe}}{1 - V_s} \quad \text{Eq 78}$$

Power consumption of the cementation reactor is based on the motor used to rotate the cementation drum. Dean, Groves & May (Dean et al., 1968) report power consumption for their cementation experiments using automobile scrap in a rotating drum as 0.284 kWh/lb $_{\text{cemented copper}}$. The actual power requirements may be somewhat less if using iron wire or scrap iron nails, because the available surface area per unit of mass of iron would be greater than for the sixpenny finishing nails used by Dean and Groves.

2.5.3. Separation and Drying of the Copper Product

The slurry exiting the cementation drum contains fine copper powder in an aqueous solution of SO_4^{2-}, Fe^{2+}, H^+, and OH^- ions. Studies on the copper powder produced by cementation have found an average particle size for the copper to be 57 μm (Jhajharia et al., 2016). The copper powder can be separated using a RDVF, as described in section 2.2.3. However, the copper must be dried to a maximum moisture content of 0.5 wt% for packaging and transport (Neikov et al., 2009).

Drying moist copper powder with hot air creates an environment where oxidation of the copper is favoured by:

$$2Cu + O_2 \rightarrow 2CuO \quad \text{Eq 79}$$

A rotary dryer can be used where the combustion products of natural gas are used as a drying agent (Neikov et al., 2009). The combustion gas has a low oxygen content which helps protect the copper from oxidation. Vacuum tray dryers can also be used to lower the boiling point of water so evaporation can take place at lower temperatures than in conventional dryers. However, they can only operate on a batch basis and have higher capital and operational costs due to the vacuum pressure at which they operate (Neikov et al., 2009). An additional step that can be taken to prevent corrosion is hydrophobization, where an inhibitor such as soap, glue, or gelatine is added to a rinse solution before filtering and drying (Neikov et al., 2009). The film of inhibitor on the surface of the copper particles provides a protective barrier against corrosion.

2.6. Wastewater Processing

The ferrous sulfate solution produced by the separation of cemented copper from the slurry can be used in wastewater treatment as a coagulant (U.S. EPA, 2023). Since the amount of wastewater produced likely surpasses the demand for coagulants in industry, it is preferable to treat the water to recover the Fe^{2+}, HSO_4^-, and SO_4^{2-} so the water can be reused in the process to dissolve H_2SO_4 in the leaching vessel, or as wash water for the RDVF's. A process for producing gypsum and magnetite from aqueous ferrous sulfate is described by Natgata et al. and is illustrated in Figure 16.

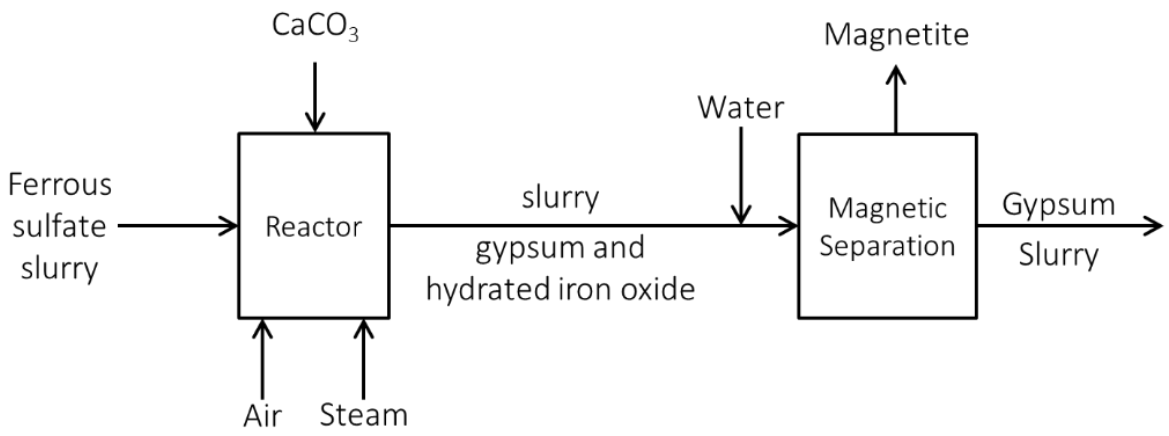

Figure 16: Box diagram for wastewater processing

The feed is aqueous ferrous sulfate with an iron concentration of 10-100 g/L. In step one, an oxidizing and neutralization reaction takes place by adding calcium carbonate, $CaCO_3$, to the feed in the presence of air and steam. If calcium hydroxide is used, then the gypsum crystals formed are very fine such that it becomes difficult to obtain good quality in a high yield (Nagata, 1979). Air used as oxidizing gas should be added at 1-8 L/min per liter of the reaction liquid. The pH of the reaction liquid is maintained at 5-6, and the temperature is maintained at 60-80 °C during the reaction. Depending on the season, the heat of reaction may be enough to maintain the reaction temperature. Otherwise, steam can be added to the reactor to increase the temperature as needed. As the reaction progresses on a batch or continuous basis, magnetite and gypsum are formed.

The water content of the slurry leaving the reactor is adjusted to 2-200 g/L and then goes through a wet magnetic separator to remove magnetite. Gypsum particles in the remaining slurry have a particle size of approximately 3-15 μm and can be separated out using a rotary drum vacuum filter. The remaining water will then only contain traces of ferric sulfate and can be reused in the process either as wash water for the RDVF's or in the leaching reactor. However, it is unknown what effect traces of Fe^{2+} may have on the

leaching reaction. Future work could investigate the effect in order to determine if additional water processing is necessary.

3. Sizing

The methods described in section 2 are applied to design a carbon purification process for a methane decomposition reactor that produces 122.4 mol/s of H_2, which is equivalent to 10,000 normal m^3/h and corresponds to a small-scale hydrogen plant (Catalan & Rezaei, 2022). Based on the stoichiometry of methane decomposition, 61.2 mol/s of pure carbon is produced in the reactor. The metallic catalyst, $Cu_{0.45}Bi_{0.55}$, contaminates the carbon thus increasing the overall flow rate of solids from the reactor.

Estimated contamination of the carbon is based on experiments by Rahimi et al. who analyzed the carbon produced by methane pyrolysis in bubble columns containing molten metals and molten salts (Rahimi et al., 2019). Solids produced by experiments using a NiBi catalyst contained 17.36 wt% carbon, 12.98 wt% nickel and 69.66 wt% bismuth. In this work, the copper and bismuth contamination of the solids is conservatively estimated to be equivalent to the nickel and bismuth contamination found in Rahimi's experiments, respectively. The actual level of carbon contamination could be lower, as other experimental research has found carbon produced on $Cu_{0.60}Bi_{0.40}$ alloy to have up to 49.9 wt% carbon (Scheiblehner et al., 2023).

Aspen Plus can be used to predict the electrolytic behaviour of species fed to the leaching vessel along with its downstream streams and processes. The ELECNRTL property method is selected in Aspen Plus. Details on the simulation methodology for these processes is outlined in their respective sections starting from section 3.5.

3.1. Carbon Product Specifications

The composition and purity of carbon black on the market can vary depending on the method of production: oil-furnace black, lampblack, thermal (decomposition) black, acetylene black, etc (Y. Wang et al., 2001). Typical rubber-grade furnace carbon black is >97.3 wt% carbon, with traces of 0.20-0.40% H_2, 0.2-1.20% O_2, 0.2-1.2% S, 0.1-1.00% ash, and 0.6-1.5% volatile components on a dry basis (Y. Wang et al., 2001). Dissolved minerals contained in hard water used to quench hot black is the source of most ash (Y. Wang et al., 2001). This process aims to produce carbon black with at least 98 wt% carbon on a dry basis. The rotary dryer is intended to reduce the moisture content of the carbon black to a maximum moisture content of 1.5 wt%, in line with typical values found in carbon black datasheets (DCL Corporation, 2020).

3.2. Vacuum Distillation

3.2.1. Vacuum Distillation Model Predictions

The feed to the vacuum distillation process is summarized in Table 1. Since vacuum distillation is a batch process, the initial melt mass is based on the solids produced in 20 h of operation of the methane pyrolysis reactor.

Table 1: Vacuum Distillation Feed Specifications

Description	**Units**	**Value**
Pure Carbon Molar Flow Rate	mol/s	61.2
Pure Carbon Mass Flow Rate	kg/s	0.735
X_{Bi}	kg_{Bi}/kg_{Solid}	0.6966
X_{Cu}	kg_{Cu}/kg_{Solid}	0.1298
X_C	kg_C/kg_{Solid}	0.1736
Solids Flow Rate	kg_{Solid}/s	4.23
Hours of MDR Operation Per Batch	h	20
Initial Melt Mass	kg_{Solid}	304844

Figure 17 illustrates the predictions of the vacuum refining model for the bismuth-to-carbon mass ratio m_{Bi}/m_C as a function of processing time in the batch lift-spray apparatus. This ratio accounts for the carbon purity with respect to bismuth. Data in Figure 17 is the result of numerical integration of Equation 37 using Runge-Kutta method in Excel.

Figure 17A shows that the processing time required to achieve a given carbon purity decreases with increasing temperature. The temperature is constrained by the materials of construction used for the vacuum distillation process. Additionally, higher temperatures require more energy input which increases the operational costs of the process. Figure 17B shows that decreasing the pressure decreases the processing time of the melt. However, very low pressures require more ejector stages. The maximum number of ejector stages outlined in the literature is 5, which can achieve vacuum pressures from 4.7 to 90 Pa (Turton et al, 2018). Figure 17C shows the effect of the initial mass fraction of bismuth (with copper included). For mixtures with a lower initial level of bismuth contamination, the processing time is less. Figure 17D shows the effect of the number of risers. As more risers are added, the processing time decreases. Lastly, Figure 17E shows the effect of the superficial liquid velocity (J_L). Increasing J_L decreases the processing time.

Sizing of the vacuum distillation process is optimized to allow a reasonable processing time for the solids mixture. The solids processing time should be less than the time it takes for the MDR to produce the next batch in order to allow sufficient time for removal of the processed solids and filling of the next batch. The mass ratio of bismuth to carbon in the product of vacuum distillation should be less than 0.005 kg_{Bi}/kg_C so that the purity of the final carbon product can contain less than 2 wt% metals when also accounting for residual copper.

Table 2 summarizes the overall design parameters from modelling the vacuum distillation apparatus. The selected temperature is 1500 K to help minimize the number of risers and processing time. The selected pressure is 30 Pa, which will require five ejector stages of the ABC-X-D-X-E type where X represents the location of a condensing heat exchanger (Turton et al, 2018). This design requires 14 risers with a diameter

of 0.4 m and length of 1 m. Each riser will have its own melt crucible and vacuum chamber. Design parameters for each melt crucible and individual risers are discussed in the following section. For a processing time of 20 hours, a product purity of 0.0031 kg_{Bi}/kg_{C} can be achieved, which meets the target of less than 0.005 kg_{Bi}/kg_{C}.

Table 2: Vacuum Distillation Model Results

Parameter	Units	Value
Temperature	C (K)	1226.85 (1500)
Pressure	Pa	30
Number of risers	-	14
Riser Diameter	m	0.4
Lift Ratio	-	0.3
jL	m/s	0.4
jG	m/s	1.4
Riser length	m	1
Processing Time	h	20
Mass Ratio Bi to C in Product	kg_{Bi}/kg_{C}	0.0031

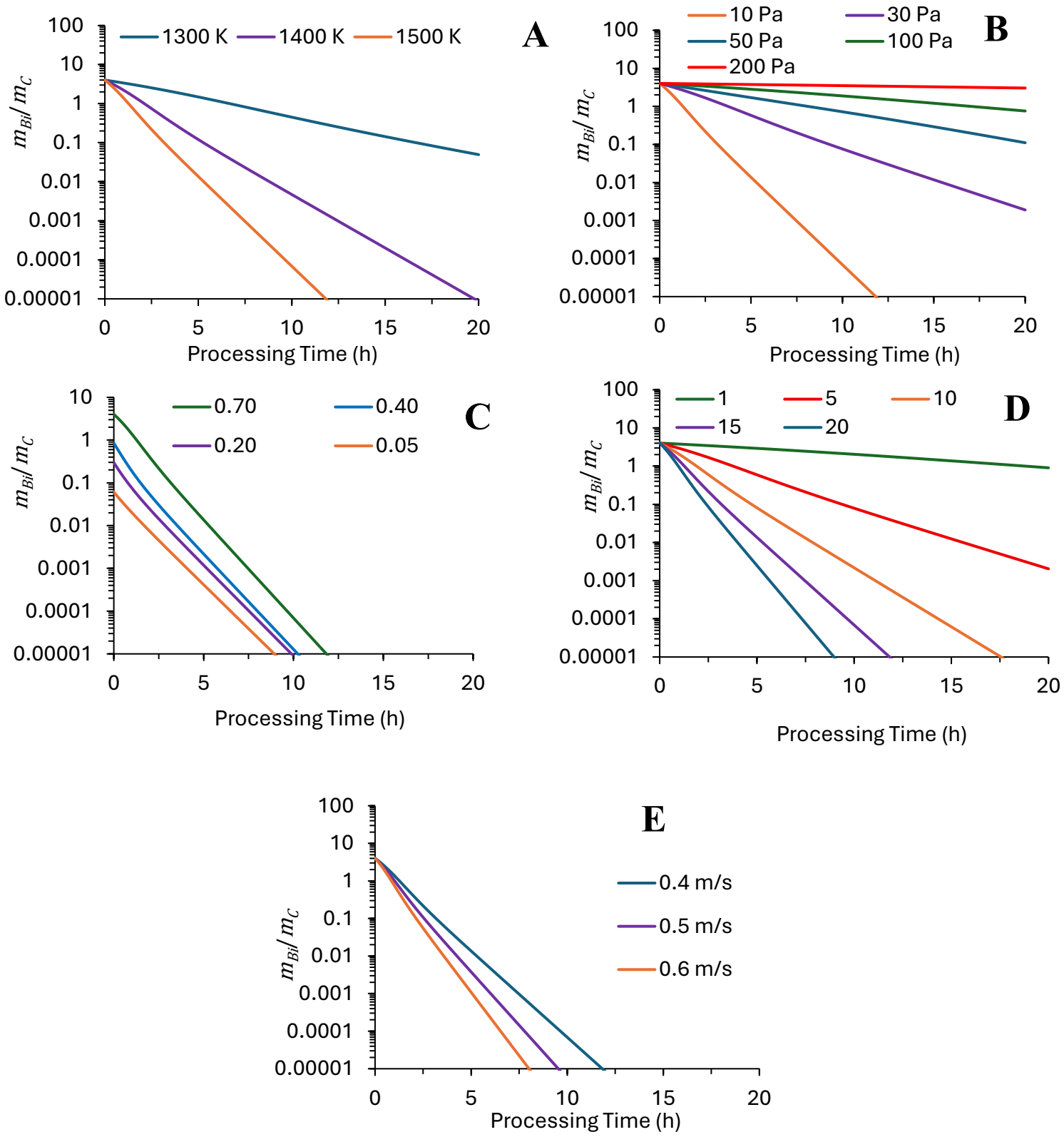

Figure 17: Effect of A) Temperature, B) Pressure, C) Initial bismuth mass fraction, D) N_{risers}, and E) J_L on bismuth processing time. [Base conditions for each trial: T=1500 K, P=10 Pa, riser diameter=0.4 m, 15 risers, J_L=0.4 m/s, J_G=1.4 m/s, Initial mass fractions XBi=0.70, XCu=0.13, XC=0.17]

3.2.2. Vacuum Distillation Dimensions

Each riser has its own melt crucible, so only after determining the number of risers, the melt crucible dimensions can be sized since the total batch of contaminated carbon is divided equally between all the melt crucibles. The crucible is designed to ensure that the riser remains submerged even as the melt level decreases during the batch processing time, see Figure 18.

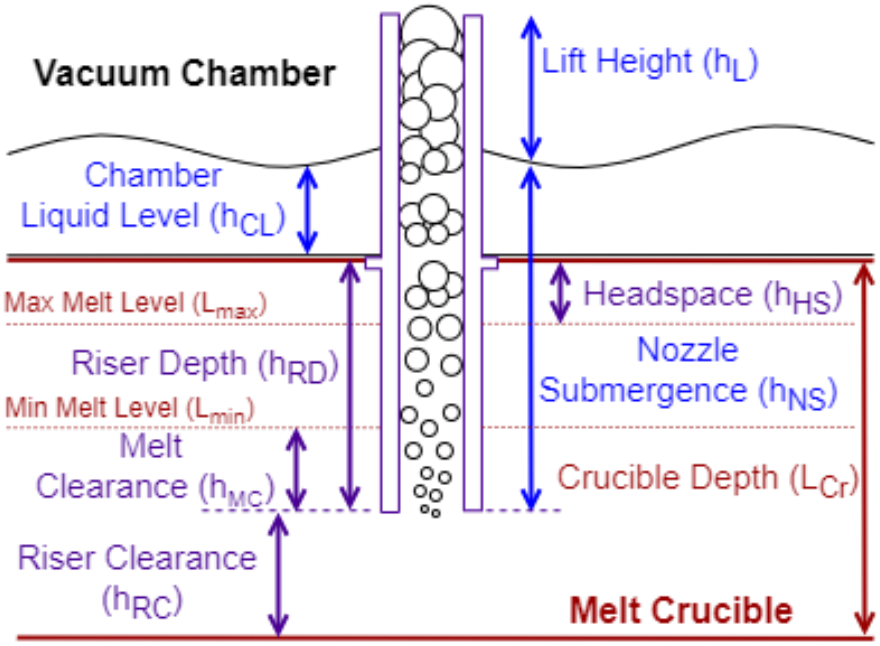

Figure 18: Melt Crucible Dimensions

The nozzle submergence h_{NS} is 0.7 m to maintain consistency with the correlation in Figure 7 between J_L and J_G. The lift height, h_L, is a function of the lift ratio, β=0.3, and h_{NS}:

$$h_L = \frac{\beta h_{NS}}{1-\beta} = 0.3\ m \qquad \text{Eq 80}$$

The total riser length, h_R, is the sum of h_L and h_{NS}. The riser depth in the melt crucible, h_{RD}, is calculated using the chamber liquid level, h_{CL}= 0.05 m.

$$h_{RD} = (h_L + h_{NS}) - h_L - h_{CL} = h_{NS} - h_{CL} \quad \text{Eq 81}$$

The depth, L_{Cr}, and diameter, D_{Cr}, of the cylindrical melt crucibles are sized to satisfy the following constraints:

i. The crucible volume must be greater than the initial melt volume

ii. The melt clearance, h_{MC}, must be equal to 0.1 m (10 cm). The melt clearance is the distance between the bottom of the riser and the minimum melt level. A minimum distance is required to ensure that the riser remains submerged while the batch is processing.

iii. The headspace, h_{HS}, must be equal to 0.05 m (5 cm). The headspace is the distance between the maximum melt level and the top of the crucible. This is to prevent the crucible from overfilling.

The crucible volume V_{Cr} is calculated by:

$$V_{Cr} = \pi \left(\frac{D_{Cr}}{2}\right)^2 L_{Cr} \quad \text{Eq 82}$$

The minimum and maximum melt levels in the crucible (L_{min} and L_{max}) are calculated using the initial and final melt volumes (V_i and V_f) and the cross-sectional area of the crucible, A_{Cr}:

$$A_{Cr} = \pi \left(\frac{D_{Cr}}{2}\right)^2 \quad \text{Eq 83}$$

$$L_{min} = \frac{V_f}{A_{Cr}};\ L_{max} = \frac{V_i}{A_{Cr}} \quad \text{Eq 84}$$

The riser clearance, h_{RC}, is the distance between the bottom of the crucible and the bottom of the riser, calculated using the crucible depth and riser depth:

$$h_{RC} = L_{Cr} - h_{RD} \quad \text{Eq 85}$$

The melt clearance, h_{MC}, is the difference between the minimum melt level and the riser clearance:

$$h_{MC} = L_{min} - h_{RC} \quad \text{Eq 86}$$

The headspace is the difference between the crucible depth and the maximum melt level:

$$h_{HS} = L_{Cr} - L_{max} \quad \text{Eq 87}$$

The melt crucible dimensions D_{Cr} and L_{Cr} are determined using the Excel Solver function with the three constraints specified. The crucible diameter is found to be 1.01 m and the depth is 0.99 m, resulting in a total crucible volume of 3.16 m^3. Table 3 summarizes the sizing parameters for the melt crucibles to satisfy the constraints listed.

Table 3: Vacuum Distillation Crucible and Riser Sizing Results

	Units	Value
Lift Ratio, β	-	0.3
Nozzle Submergence, h_{NS}	m	0.7
Lift Height, h_L	m	0.3
Chamber Liquid Level, h_{CL}	m	0.05
Riser Length, h_R	m	1
Riser Depth, h_{RD}	m	0.65
Crucible Depth, L_{Cr}	m	0.99
Crucible Diameter, D_{Cr}	m	1.01
Crucible Volume, V_{Cr}	m^3	3.16
Initial Melt Volume*	m^3	3.00
Final Melt Volume*	m^3	1.41
Minimum Melt Level, L_{min}	m	0.44
Maximum Melt Level, L_{max}	m	0.94
Riser Clearance, h_{RC}	m	0.34
Melt Clearance, h_{MC}	m	0.10
Headspace, h_{HS}	m	0.05

*From vacuum refining model calculations

Each riser will have its own vacuum chamber, sized to accommodate the spray from the riser. Allaire interviewed RH degassing unit operators to determine that the minimum radial dispersion of the riser's spray is one meter, so the vacuum chamber's minimum diameter is set to 3.2 m (Allaire, 1991). The maximum spray height is 2 meters, and an additional 2 meters of free board above the spray is required to avoid excessive splashing into the exit vacuum duct and condenser. Therefore, the cylindrical vacuum chamber height is the sum of h_{CL}, h_L, the riser spray height, and the freeboard distance above the spray. In this process, the vacuum chamber height is 0.05 + 0.3 + 2 + 2 = 4.35 m.

The average mass flow rates and mass fractions of carbon, copper and bismuth leaving the vacuum distillation process are summarized in Table 4.

Table 4: Vacuum Distillation Product Flow Rates and Mass Fractions

	Mass Flow Rate (kg/h)	Mass Fraction
Carbon	2646.04	0.5712
Copper	1978.44	0.4271
Bismuth	8.115	0.0018
Total	4632.6	1.000

3.3. Granulation and Dewatering

The next step in processing this material is granulation and dewatering. Since vacuum distillation takes place above the melting point of copper, the copper and remaining bismuth are in molten liquid form at the end of vacuum distillation. The granulation tank uses a 1:10 mass ratio of solids to water to break up the molten mixture into 1 cm particles and cool them. Multiplying the total mass flow of material leaving vacuum distillation by ten gives the mass flow rate of water to granulation, 46326 kg/h in this case. The total feed to granulation is summarized in Table 5.

Table 5: Granulation Feed Mass Flows and Fractions

	Mass Flow Rate (kg/h)	Mass Fraction
Carbon	2646	0.05193
Copper	1979	0.03882
Bismuth	8.115	0.000159
Water	46326	0.909
Total	50959	1.000

After granulation, dewatering is required to adjust the water content so the feed to the grinder is 45 wt% solids. The total mass flow of the dewatered mixture to the grinder, 10294.7 kg/h, is determined by:

$$Mass\ Flow\ to\ Grinder = \frac{Mass\ Flow\ of\ Dry\ Solids}{Mass\ Fraction\ of\ Solids\ in\ Grinder\ Feed} \quad \text{Eq 88}$$

The mass flow rate of water removed by dewatering is the difference between the total mass flow to granulation and the mass flow to the grinder, 40663.9 kg/h.

3.4. Grinding

The particle size entering the grinder (F_{80}) comes from the granulation process and is 1 mm (1000 μm), so the minimum product size (P_{80}) achievable is 10 μm because this correlates to a reduction ratio (Equation 38) of 100 which is the maximum reduction ratio for a stirred mill. The feed to the grinder is summarized in Table 6, and the methods described in section 2.2.2 are used to calculate the grinder's power consumption rate for a range of applicable P_{80} sizes, as illustrated in Figure 19.

Table 6: Mass Flows and Fractions Leaving Grinder

	Mass Flow Rate (kg/h)	Mass Fraction
Carbon	2646.04	0.2570
Copper	1978.44	0.1922
Bismuth	8.115	0.00079
Water	5662.06	0.5499
Total	10294.7	1.000
Total (Dry Basis)	4632.64	-

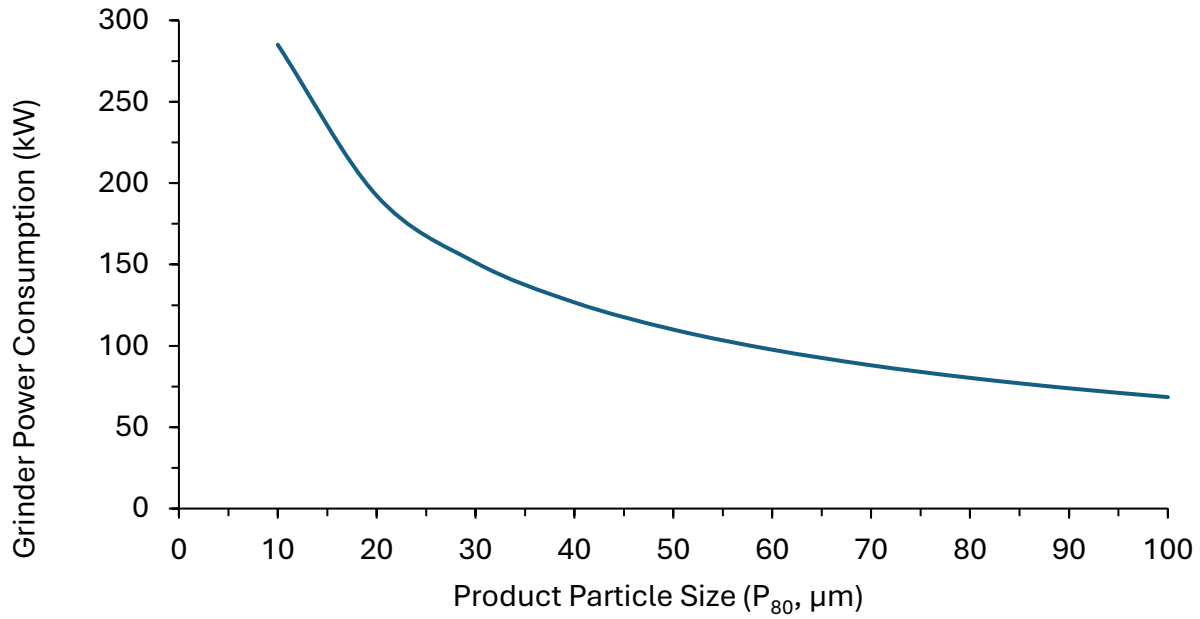

Figure 19: Grinder Power Consumption

The selected P_{80} is 50 µm because this particle size allows for a reasonable leaching vessel size while minimizing the grinder power consumption. The total mass flow rate on a dry basis is used to calculate the grinder power consumption (P_G).

$$P_G = 23.74 \frac{kWh}{t} * 4.63264 \frac{t}{h} = 110.0\ kW \quad \text{Eq 89}$$

The material leaving the grinder has the same composition as the feed outlined in Table 6 on a dry basis. However, the grinder feed is a slurry consisting of 45 wt% solids, but the leaching vessel requires a feed ratio of 0.15 kgSolid/kgLiquid (13.0 wt% solids), so additional water is added to the mixture. Aspen Plus is used to optimize the ratio. Based on the flow rate of solids, a total liquid flow of 28, 080 kg/h is required. Subtracting the water present from the grinding process gives 28,080 – 5662 = 22,418 kg/h of water needs to be mixed with the feed entering the leaching vessel from the grinder.

3.5. Aspen Plus Simulation of Electrolytic Processes

After grinding, the solids mixture of copper, carbon, and traces of bismuth is mixed with water and H_2SO_4 to be fed to the leaching vessel. To obtain more accurate predictions of speciation, electrochemical reactions, liquid densities and volumetric flow rates, Aspen Plus is used to model the electrolytic process downstream of the grinder. Figure 20 outlines the Aspen Plus flowsheet for the model. Heat and material balance tables for all of the streams modeled in Aspen Plus are in Appendix I. In the following sections, the simulation methodology for each electrolytic process will be described along with the sizing results.

3.6. Solids Modelling in Aspen Plus

Individual streams for the solids, water, and H_2SO_4 content are modeled in Aspen Plus to make up the feed to the leaching vessel (Figure 20, LEACHR). The composition and flow rate of the solids stream is taken from Table 4 which describes the product leaving the MDR on a dry basis. Based on a leaching vessel Cu conversion of 99.8%, the particles are expected to decrease in size from P_{80}= 50 μm at the inlet to P_{80}= 6.3 μm at the outlet of the leaching vessel as per Equation 47. Experimental data from an investigation on the particle size distribution where the P_{80} = 10 μm in the product of a stirred mill using stainless steel media, summarized in Table 7, is used to enter the PSD mesh and particle sizes in Aspen Plus (Huang et al., 2022). The PSD entered in Aspen Plus allows for more conservative sizing of the dryer because the P_{80} entered (10 μm) is larger than the expected P_{80} (6.3 μm), which will likely cause the dryer to underpredict the rate of drying for liquid on the surface of the particles, since smaller particles will have more specific surface area for drying than large ones.

The PSD mesh in Aspen Plus is populated by specifying a normal distribution function with a standard deviation of 6.5 microns and a D_{50} of 4.5 microns (Huang et al., 2022). The solids PSD mesh and weight fractions calculated by Aspen Plus are summarized in Table 7. Intervals 4 and 5 in Table 7 are the most

significant because the particle size of 10 μm fits within the cumulative weight fraction range containing 0.80, meaning that the model for a normal distribution of particle sizes fits the intended P_{80}= 10 μm.

Table 7: PSD Mesh and weight fractions of solid mixture containing carbon, copper, and bismuth

Interval	Lower limit (μm)	Upper limit (μm)	Weight fraction	Cumulative weight fraction
1	0	2	0.3533	0.3533
2	2	4	0.1201	0.4734
3	4	6	0.1230	0.5964
4	6	8	0.1146	0.7109
5	8	10	0.0972	0.8082
6	10	12	0.0751	0.8833
7	12	14	0.0528	0.9361
8	14	16	0.0338	0.9699
9	16	18	0.0197	0.9896
10	18	20	0.0104	1.0000

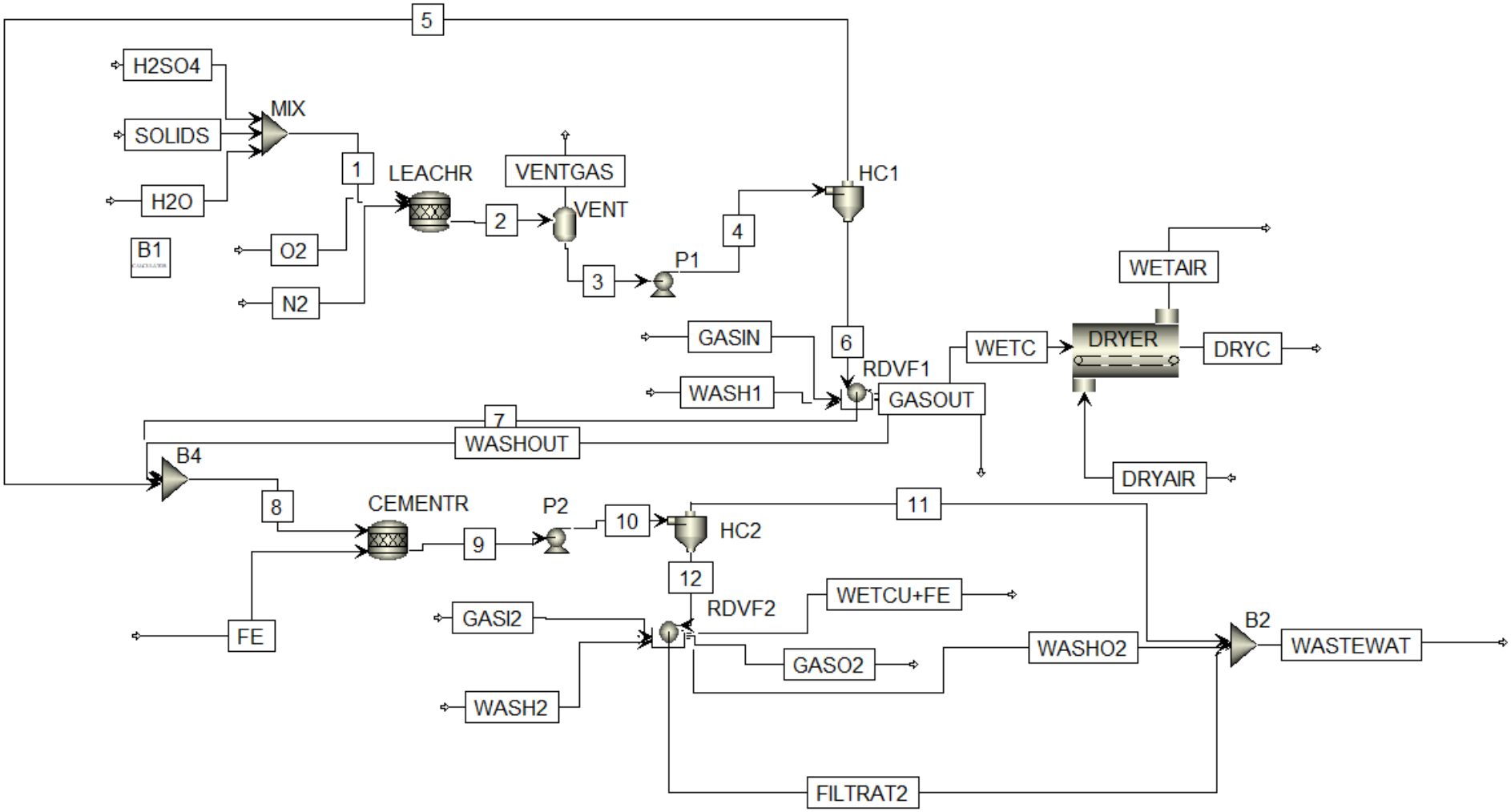

Figure 20: Aspen Plus Flowsheet

3.7.Leaching Vessel

3.7.1. Leaching Vessel Modelling Predictions

Figure 21 illustrates the effect of different parameters on the leaching vessel reactor size, as predicted by Equation 46. Figure 21A shows that increasing the temperature significantly decreases the reactor size, as this speeds up the kinetics of the leaching reaction. Increasing the reactor pressure also decreases the reactor size (Figure 21B) because the reaction rate is proportional to the square root of the partial pressure of oxygen in the vessel. However, operating at pressures above atmospheric would increase the capital and operational costs of the vessel. Figure 21C shows that the reactor size reaches a minimum for an intermediate value of $y_{Cu,i}$ which is explained by the relationship $V_L \propto \left(1 - y_{Cu,i}\right)^{-1} {y_{Cu,i}}^{-0.5}$ in equation 46. Figure 21D shows that increasing the inlet copper particle sizes require a larger reactor, because there is less surface area for the leaching reaction to occur for a given amount of solid copper in the reactor. Last, figure 21E shows that the reactor size decreases as $x_{s,i}$ (kg_{Solid}/kg_{Liquid}) increases, which is consistent with $V_L \propto x_{s,i}^{-3/2}$ in Equation 46.

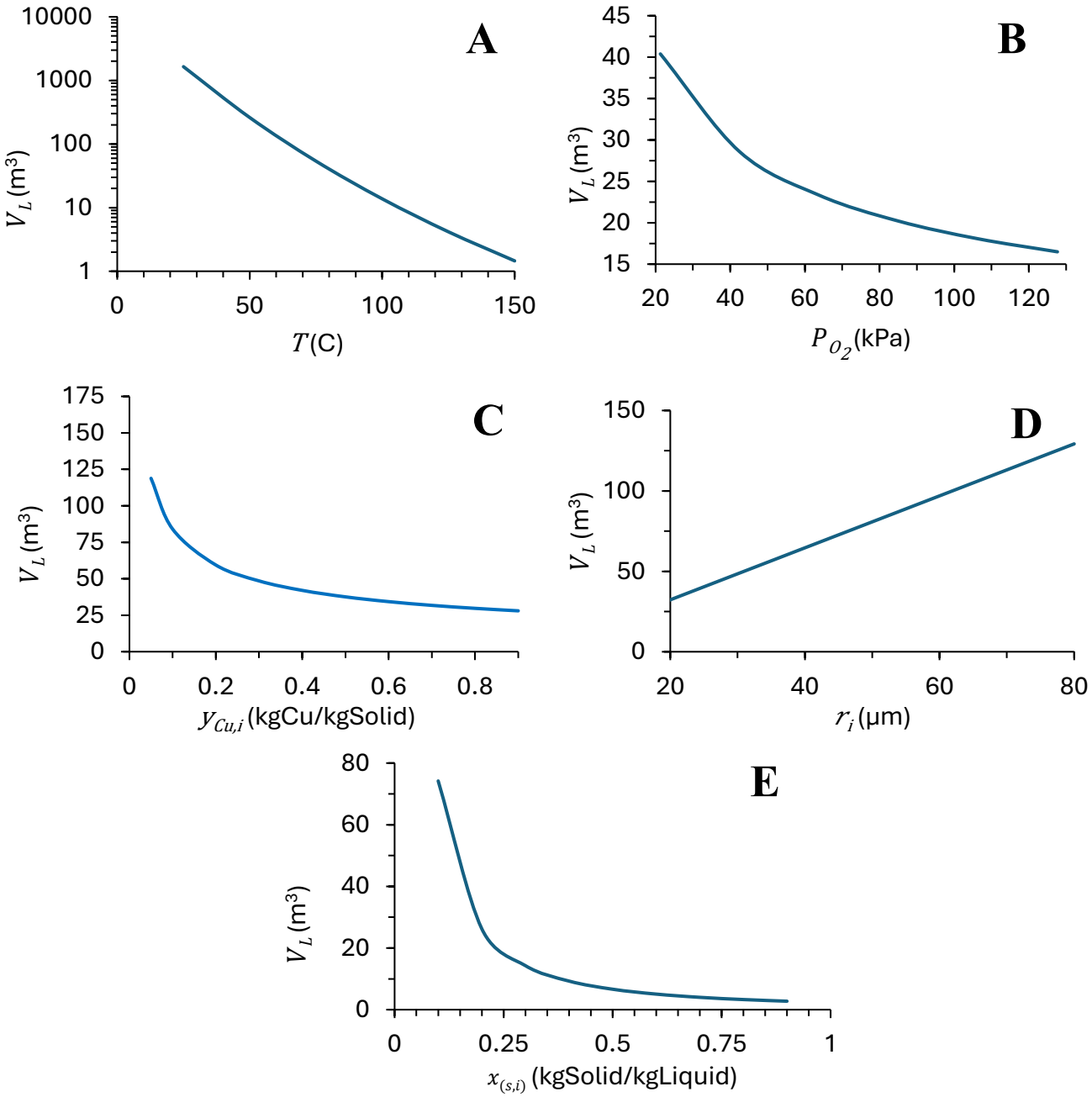

Figure 21: Effect of A) Temperature, B) P_{O_2}, C) $y_{Cu,i}$, D) r_i, and E) $x_{s,i}$ on V_L (m^3). [Base conditions: X_{Cu}= 0.998, $\dot{m}_c$= 0.736 kg$_C$/s, $y_{Cu,i}$= 0.423, $x_{s,i}$= 0.15, P_{O_2}= 21.28 kPa, T=80 °C, $\dot{m}_s$= 1.3 kg$_S$/s]

3.7.2. Leaching Vessel Simulation Methodology

The leaching vessel is modeled in Aspen Plus as a Stoichiometric Reactor which uses the chemical reaction for copper dissolution (Equation 43) and a specified fractional conversion of $Cu_{(s)}$ to calculation the composition and properties of the outlet stream. For a given conversion of $Cu_{(s)}$, Aspen Plus can provide more accurate inputs for the leaching vessel liquid volume calculation outlined in Equation 46. Additionally, the selected reactor temperature is entered in Aspen Plus to determine the heat duty of the leaching vessel.

Aspen Plus is used to optimize the ratio of H_2O and H_2SO_4 in the feed slurry to ensure that the mixture inside the reactor maintains a maximum pH of 1. Using the ELECNRTL model, Aspen Plus can calculate how much H^+ is complexed in a side reaction that can form HSO_4^-:

$$H^+ + SO_4^{2-} \leftrightarrow HSO_4^- \qquad \text{Eq 90}$$

The slurry fed to the leaching vessel is modeled as a mixture of solids (consisting of Cu, Bi, and C), H_2SO_4, and H_2O. The mass flows of species in the SOLIDS stream are specified using the flows to the grinder on a dry basis. Then, the flows of H_2SO_4 and H_2O are adjusted using trial and error until the desired $X_{s,i}$ in the feed slurry (Stream 1) is achieved and the desired pH is met by the product stream (Stream 2) leaving the leaching vessel.

The O_2 stream is specified to provide 15 mol% excess oxygen for the leaching reaction to proceed, and a calculator block (B1) calculates the flow rate of N2 based on the ratio of O_2 to N_2 in air that is 21:79. Results of the Aspen Plus model are used to obtain accurate inputs for ρ_L and $x_{s,i}$ in equation 46.

3.7.3. Leaching Vessel Sizing Results

Table 8 summarizes the optimal design conditions selected for the leaching vessel. If the leaching vessel can operate at atmospheric pressure, then capital costs can be minimized because the vessel wall thickness will not have to withstand high pressures. When air is the source of oxygen to the reaction, the partial pressure of O_2 is kept at 21 kPa as long as the oxygen content of the air source is 0.21 mol fraction. The ratio of solid to liquid in the feed slurry, $X_{s,i}$, is kept at 0.15 kg_{Solid}/kg_{Liquid}, a typical value for feed slurry compositions for flotation cells used in the mineral processing industry (Schlesinger et al., 2011). The ratio of metallic copper to solid in the feed, $y_{Cu,i}$ = 0.433 kg_{Cu}/kg_{Solid} is calculated based on the experiments of Rahimi et al. (2019), and the calculated amount of bismuth removed in the vacuum distillation step. The reaction temperature should avoid approaching 100 °C to avoid boiling the mixture at atmospheric pressure, so 90 °C is selected to minimize the reactor size while supplying enough heat to speed up the reaction kinetics and minimize the reactor volume. Last, the initial particle size is selected to be 50 μm as this is a relatively small feed particle size for a leaching vessel without approaching the absolute minimum particle size that the stirred mill can achieve, 10 μm, which would consume significantly more power to achieve as illustrated in Figure 19. The final leaching vessel size is 27.51 m^3 and the reactor duty is 4.16MW.

Table 8: Leaching Vessel Specifications

Parameter	Units	Value
$X_{Cu(s)}$	-	0.998
r_i	μm	25
yCu	kgCu/kgSolid	0.433
Xs	kgSolid/kgLiq	0.15
ρL	kg/m^3	1080.48
PO_2	kPa	21
$\dot{m}_s$	kgSolid/s	1.299
T	°C	90

3.8.RDVF 1

RDVF's 1 and 2 are modeled in Aspen Plus because they are downstream of the leaching vessel where the electrolytic model begins. The slurry leaving the leaching vessel contains about 7 wt% solids whereas the optimal RDVF feed should contain about 20-30 wt% solids. A hydrocyclone is used as a pre-thickener to remove some liquid from the slurry in order to obtain efficient separation and washing in RDVF1. The pressure drop across the hydrocyclone is assumed to be 2 bar, so a pump is used to increase the pressure of the slurry leaving the leaching vessel to 3 bar. The desired moisture content of the feed slurry to RDVF 1, 70 wt% liquid, is used to calculate the liquid load of solid outlet by:

$$L_s = \frac{0.70}{1 - 0.70} = 2.3 \ \frac{kg\ liquid}{kg\ solid} \qquad \text{Eq 91}$$

RDVF 1 is modeled in Aspen Plus as a Drum Solids Separator in order to determine the amount of wash water required and the remaining contaminants in the carbon product.

3.8.1. RDVF 1 Parameter Study

The effect of immersion depth, wash angle, and filtration-deliquoring angle are studied to see the effect on HSO_4^- mass flow and H_2O mass flow in the filter cake. HSO_4^- is studied because it is the contaminant of highest concentration in the feed slurry, so effective cake washing should remove as much HSO_4^- as possible so the final carbon product is as pure as possible. The mass flow of H_2O in the filter cake indicates the effectiveness of the filter in removing water, which will help to reduce the size and energy consumption of the dryer. Figure 22 illustrates the effect of the RDVF design specifications on the filter performance. The effects of all parameters studied are minimal because the Aspen Plus simulation gives warnings (e.g. excessive or insufficient cake thickness) or does not converge when unacceptable values are entered. See Figure 11 for a schematic illustrating the relevant angles of a RDVF.

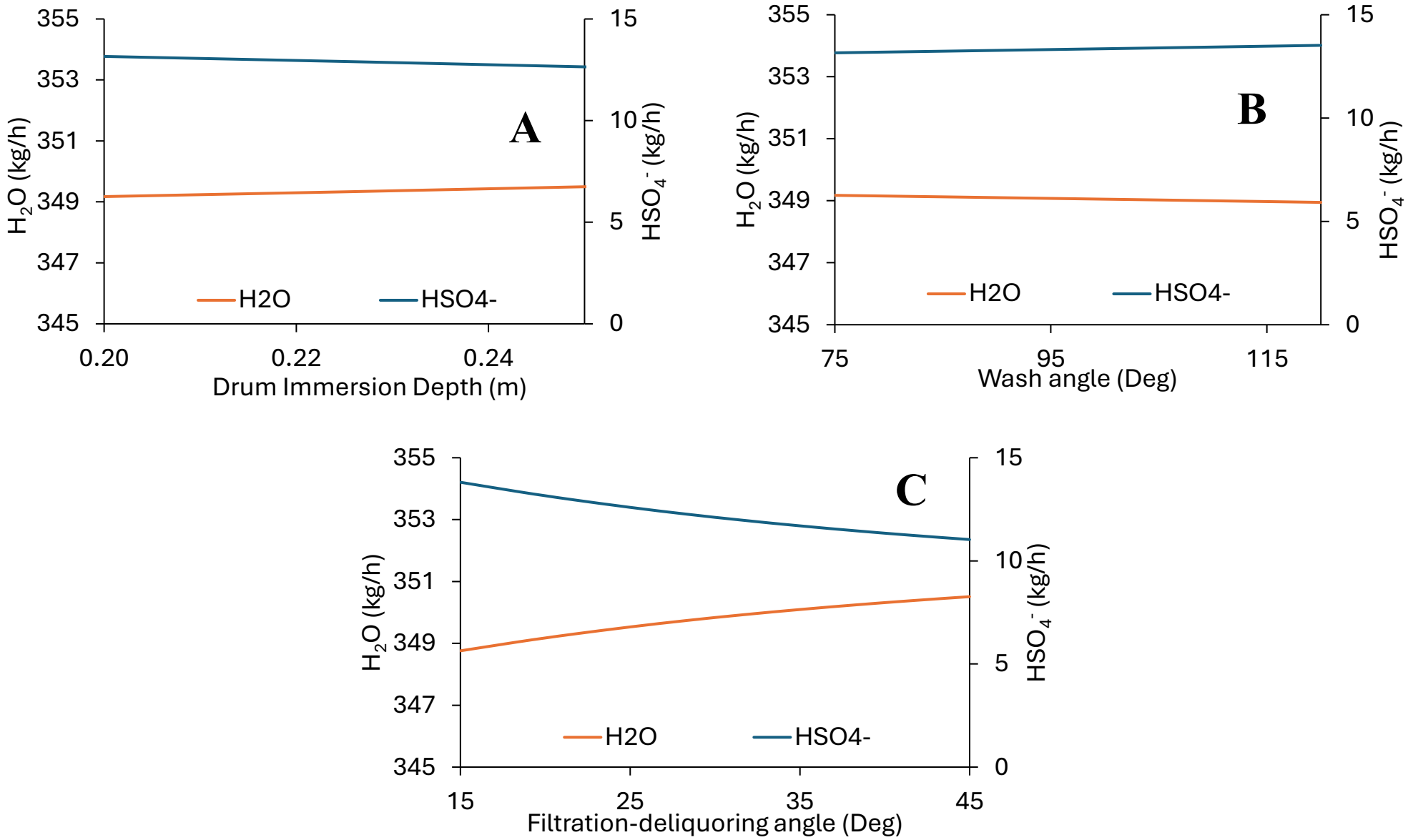

Figure 22: Effect of A) drum immersion depth (E), B) wash angle, C) filtration-deliquoring angle on H_2O and HSO_4^- mass flow rates in RDVF 2 filter cake. Base conditions: E=0.2 m, $\alpha_{washing}$=75°, $\alpha_{filtration\text{-}deliquoring}$=20°.

The optimized dimensions of RDVF 1 are summarized in Table 9. RDVF 1 removes 98.5% of HSO_4^- from the feed slurry and produces a filter cake with 74% solid fraction. Table 9 contains the heat and mass balance around RDVF 1. The wash water flow rate is 1728 kg/h, corresponding to a wash ratio of 0.37 kg water/kg dry solids. This is well within the range of typical RDVF's with wash ratios ranging from 0.2 – 2 kg water/kg dry solids (BOKELA, 2025)

Table 9: RDVF 1 Aspen Plus Specifications

Parameter	Units	Value
Specifications		
Drum Diameter	m	4
Drum Width	m	7
Number of Segments	-	24
Drum Speed	rpm	0.2
Immersion Depth	m	0.2
Filtration-deliquoring Angle	deg	45
Filtration Pressure Drop	bar	0.5
Washing Angle	deg	120
Deliquoring Angle	deg	60
Deliquoring Pressure Drop	bar	0.6
Filter Cake		
Compressibility model	-	incompressible
Aspect ratio	-	1
Washing		
Washing model	-	Choudhury & Dahlstrom
Washing efficiency	-	0.75
Wash liquid flow direction	-	Counter-Current
Number of wash zones	-	1
Deliquoring		
Deliquoring model	-	Schubert
Wetting angle	Deg	90
Schubert N parameter	-	2

Table 10: RDVF1 Stream Summary

Stream	Units	6	WETC	7	WASH1	WASHOUT	GASIN	GASOUT
Description								
Temperature	C	4.54	14.91	14.89	25.00	14.91	25.00	25.00
Pressure	bar	1.00	1.01	1.50	6.08	5.78	1.50	0.90
Mass Vapor Fraction	-	0.00	0.00	0.00	0.00	0.00	1.00	1.00
Mass Liquid Fraction	-	0.75	0.26	1.00	1.00	1.00	0.00	0.00
Mass Solid Fraction	-	0.25	0.74	0.00	0.00	0.00	0.00	0.00
Mass Flows	kg/hr	10719.5	3618.4	7008.9	1728.0	1753.0	9101.8	9178.2
Mass Fractions								
H_2O		0.5903	0.2536	0.7705	1.0000	0.9430	0.0000	0.0095
Cu		0.0004	0.0011	0.0000	0.0000	0.0000	0.0000	0.0000
H_2SO_4		0.0000	0.0000	0.0000	0.0000	0.0000	0.0000	0.0000
O_2		0.0000	0.0000	0.0000	0.0000	0.0000	0.0000	0.0000
H^+		0.0004	0.0000	0.0005	0.0000	0.0002	0.0000	0.0000
OH^-		0.0000	0.0000	0.0000	0.0000	0.0000	0.0000	0.0000
HSO_4^-		0.0797	0.0018	0.1198	0.0000	0.0231	0.0000	0.0000
SO_4^{--}		0.0395	0.0013	0.0512	0.0000	0.0164	0.0000	0.0000
Cu^{2+}		0.0396	0.0010	0.0568	0.0000	0.0131	0.0000	0.0000
C		0.2492	0.7381	0.0000	0.0000	0.0000	0.0000	0.0000
AIR		0.0000	0.0007	0.0011	0.0000	0.0042	1.0000	0.9903
Bi		0.0008	0.0023	0.0000	0.0000	0.0000	0.0000	0.0000
N_2		0.0002	0.0000	0.0002	0.0000	0.0000	0.0000	0.0000

3.9. Carbon Product Dryer

A dryer is used remove water from the RDVD 1 filter cake containing purified carbon and is modeled in Aspen Plus as a continuous co-current convective dryer. Heuristics are used to specify the residence time as 5 minutes (Couper et al., 2005). The dryer length is optimized by observing the model predictions and adjusting the length to obtain the desired product dryness. The mass transfer model is based on a specified number of mass transfer units (NTU) of 1.5, based on typical values for a rotary dryer (Dutta, 2009). Drying curve specifications are taken from experimental data where the sorption of water vapour on carbon black was studied (Dewey et al., 1932). The critical solids moisture content is 0.0295 and the equilibrium solids moisture content is 0.0130. The drying curve shape factor entered in Aspen Plus is 0.5, which corresponds to a straight line. Dry air is fed to the dryer at 1 atm and 250 °C, and the air flow rate is adjusted until the carbon moisture content is less than 1.5 wt%. The dryer diameter is calculated based on heuristics to verify that the length to diameter ratio of the dryer is within the optimal range of 4-10 (Mujumdar, 2006). Calculation of the dryer diameter is as follows.

The typical air velocity v_{air} in a rotary dryer is 1.5-3 m/s, so 3 m/s is estimated to be conservative (Couper et al., 2005). The volumetric flow rate of air Q_{air} is taken from Aspen Plus to be 6.80 m^3/s. The cross-sectional area of the dryer A_{dryer}, m^2 can be calculated by:

$$A_{dryer} = \frac{Q_{air}}{v_{air}} \quad \text{Eq 92}$$

The dryer diameter d_{dryer} is calculated from the cross-sectional area as:

$$d_{dryer} = 2\sqrt{\frac{A_{dryer}}{\pi}} \quad \text{Eq 93}$$

After checking the L/D ratio, the length and air flow rate can be adjusted iteratively to stay within the optimal design specifications for a rotary dryer of 4 to 10. The final dryer design specifications are summarized in Table 11.

Table 11: Dryer Specifications

Parameter	Units	Value
Feed Specifications		
Mass Solid Fraction	-	0.74
Mass Liquid Fraction	-	0.26
Volumetric Flow Rate	m^3/h	2.11
Dryer Specifications		
Q_{air}	m^3/s	6.80
v_{air}	m/s	3
A_{dryer}	m^2	2.03
d_{dryer}	m	1.61
Dryer Length	m	6.5
L/D ratio	-	4.04
Surface Area Inside Dryer (not including flights)	m^2	32.82

The dryer performance is plotted in Figure 23 to illustrate the effectiveness of moisture removal throughout the dryer. The solids reach the maximum dryness indicated by the equilibrium moisture content, 0.0256, near the outlet of the dryer. Table 12 contains the heat and mass balance of streams in and out of the dryer.

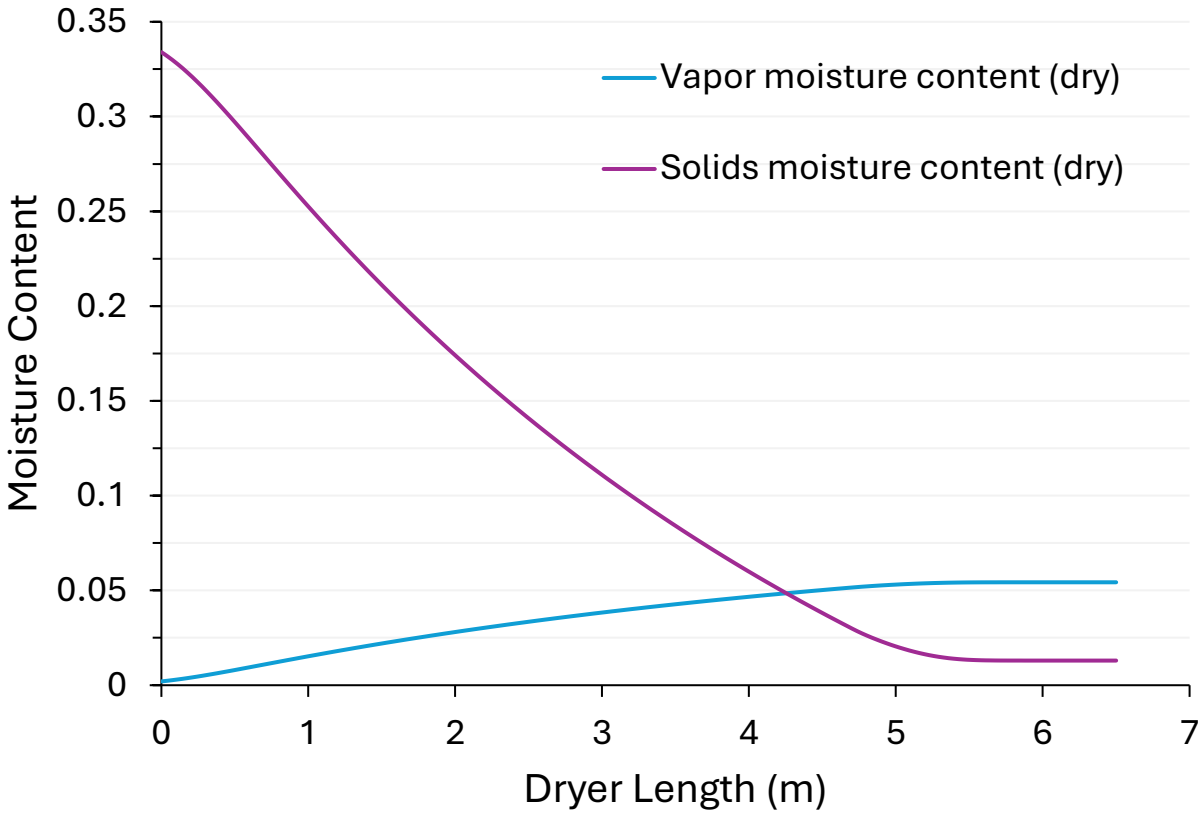

Figure 23: Vapor and solids moisture content (wt %) along the length of the rotary dryer

Table 12: Dryer Stream Summary

Stream	Units	WETC	DRYC	DRYAIR	WETAIR
Description					
Temperature	C	14.89	90.30	250.00	103.65
Pressure	bar	1.01	1.01	1.01	1.01
Mass Vapor Fraction	-	0.00	0.00	1.00	1.00
Mass Liquid Fraction	-	0.19	0.01	0.00	0.00
Mass Solid Fraction	-	0.81	0.99	0.00	0.00
Mass Flows	kg/hr	3618.3	2733.0	16500.0	17385.2
Mass Fractions					
H_2O		0.2536	0.0128	0.0020	0.0527
Cu		0.0011	0.0015	0.0000	0.0000
H_2SO_4		0.0000	0.0000	0.0000	0.0000
O_2		0.0000	0.0000	0.0000	0.0000
H^+		0.0000	0.0000	0.0000	0.0000
OH^-		0.0000	0.0000	0.0000	0.0000
$HSO4^-$		0.0018	0.0040	0.0000	0.0000
SO_4^{--}		0.0013	0.0000	0.0000	0.0000
Cu^{2+}		0.0010	0.0013	0.0000	0.0000
C		0.7381	0.9772	0.0000	0.0000
AIR		0.0007	0.0000	0.9980	0.9473
Bi		0.0023	0.0031	0.0000	0.0000

3.10. Cementation Reactor

The cementation reactor is modeled as a Stoichiometric Reactor in Aspen Plus specified with equation 61 as the reaction with a fractional conversion of Cu of 0.98. The reactor temperature is equal to the temperature of the feed (Stream 8), 7.18 °C and the pressure is 1 atm. An additional feed of pure iron is fed to the reactor. Based on the stoichiometry of the cementation reaction, Fe is fed at the rate it is consumed in the cementation reaction. The Aspen Plus model is used to obtain inputs for the volumetric flow rate of liquid, Q, and the concentration of Cu^{2+} in the feed stream, $[Cu^{2+}]_{in}$ in the calculations outlined in section 2.5, which are carried out using the Excel Solver function. The final cementation reactor specifications are summarized in Table 13. After calculating the total reactor volume, the length and diameter are optimized to maintain the length-to-diameter ratio of 3.6 as used in the experiments of Fisher and Groves (1976).

Table 13: Cementation Reactor Specifications

Parameter	Units	Value
Volumetric Flow Rate of Liquid In, Q	m^3/s	9.497×10^{-3}
Concentration of Cu^{2+} in, $[Cu^{2+}]_{in}$	g/m^3	58190
Volume of Solution in Reactor	m^3	1
Volume of Iron in Reactor	m^3	0.01822
Void Space Fraction in Reactor, V_s	-	0.1830
Total Reactor Volume	m^3	1.25
Length, L_{CR}	m	2.74
Diameter, D_{CR}	m	0.76
$Fe_{(s)}$ consumption rate	kg/h	0.4761

The slurry leaving the cementation reactor contains metallic copper and traces of iron. The iron supplied to the reactor is modeled as 1" pieces of 10 gauge thickness, so most of them will remain inside the reactor if a strainer device is used at the slurry outlet. However, since the size of the iron pieces decreases as the cementation reaction proceeds, a small amount of iron is expected to leave with the slurry. The slurry

leaving the cementation reactor is 95 wt% liquid, so it must pass through a hydrocyclone (HC2) to optimize the liquid content of the slurry to 66 wt% before it is fed to RDVF 2. HC2 is modeled in Aspen Plus following the same methodology described for HC1.

3.11. RDVF 2

RDVF 2 removes liquid from the copper product and washes away entrained impurities from the cementation solution. RDVF 2 is modeled similarly to RDVF 1 in Aspen Plus. The feed contains 66.6 wt% liquid and 7.7% HSO_4^-. The filter cake contains 1.6 wt% liquid and a negligible amount of HSO_4^-. The filter cake is 98.4wt% Cu with 0.35 wt% Fe. The optimized dimensions of RDVF 2 are summarized in Table 14. Table 15 summarizes the stream results for RDVF 2.

Table 14: RDVF 2 Aspen Plus Specifications

Parameter	Units	Value
Specifications		
Drum Diameter	m	3.5
Drum Width	m	1
Number of Segments	-	12
Drum Speed	rpm	0.2
Filtration Angle	deg	120
Filtration-deliquoring angle	deg	90
Filtration Pressure Drop	bar	0.5
Deliquoring Angle	deg	60
Deliquoring Pressure Drop	bar	0.5
Filter Cake		
Compressibility model	-	incompressible
Aspect ratio	-	1
Washing		
Washing model	-	Choudhury & Dahlstrom

Washing efficiency	-	0.75
Wash liquid flow direction	-	Counter-Current
Number of wash zones	-	1
Deliquoring		
Deliquoring model	-	Schubert
Wetting angle	Deg	90
Schubert N parameter	-	2

Table 15: RDVF 2 Stream Summary

Stream	Units	12	WETCU+FE	FILTRAT2	WASH2	WASHO2	GASI2	GASO2
Description								
Temperature	C	13.50	14.86	14.86	25.00	14.86	25.00	25.00
Pressure	bar	2.00	1.01	1.50	6.00	5.50	1.00	0.50
Mass Vapor Fraction	-	0.00	0.00	0.00	0.00	0.00	1.00	1.00
Mass Liquid Fraction	-	0.67	0.02	1.00	1.00	1.00	0.00	0.00
Mass Solid Fraction	-	0.33	0.98	0.00	0.00	0.00	0.00	0.00
Mass Flows	kg/hr	5850.6	1982.1	3847.9	396.0	372.2	6066.5	6110.7
Mass Fractions								
H_2O		0.5230	0.0159	0.7835	1.0000	0.9772	0.0000	0.0075
Cu		0.3332	0.9835	0.0000	0.0000	0.0000	0.0000	0.0000
H_2SO_4		0.0000	0.0000	0.0000	0.0000	0.0000	0.0000	0.0000
O_2		0.0000	0.0000	0.0000	0.0000	0.0000	0.0000	0.0000
H^+		0.0003	0.0000	0.0005	0.0000	0.0001	0.0000	0.0000
OH^-		0.0000	0.0000	0.0000	0.0000	0.0000	0.0000	0.0000
HSO_4^-		0.0769	0.0000	0.1166	0.0000	0.0083	0.0000	0.0000
SO_4^{--}		0.0336	0.0001	0.0498	0.0000	0.0078	0.0000	0.0000
Cu^{2+}		0.0007	0.0000	0.0011	0.0000	0.0001	0.0000	0.0000
C		0.0000	0.0000	0.0000	0.0000	0.0000	0.0000	0.0000
Fe		0.0001	0.0003	0.0000	0.0000	0.0000	0.0000	0.0000
Fe^{2+}		0.0316	0.0000	0.0476	0.0000	0.0046	0.0000	0.0000
AIR		0.0003	0.0001	0.0006	0.0000	0.0020	1.0000	0.9925

3.12. Copper Product Dryer

Sizing the dryer for the copper product in Aspen Plus requires information on the particle size distribution (PSD) in terms of mass fractions. Some studies have been conducted to evaluate the PSD of cemented copper in terms of volume fractions (Jhajharia et al., 2016; Poço et al., 2006). Volume fractions can be converted to mass fractions using the density of the particles. However, due to the presence of iron in the cemented copper, the density of different particle size fractions cannot be assumed to be uniform. Detailed information on the density of different particle sizes is required to accurately model the PSD in Aspen Plus using the information available in the literature.

4. Costing

4.1. Module Factor Approach to Costing

The module factor approach to costing is applied to the leaching and cementation vessels, pumps, pump drives, dryer, and filters (Turton et al, 2018). First, the purchased cost of equipment at ambient operating pressure and using carbon steel construction, C_p°, is fitted to the equation (Turton et al, 2018):

$$\log_{10} C_p^\circ = K_1 + K_2 \log_{10}(A) + K_3[\log_{10}(A)]^2 \qquad \text{Eq 94}$$

where A is the capacity or size parameter for the equipment, whose units are defined in Turton et al. (2018). K_1, K_2, and K_3 are constants specific to each type of equipment and are outlined in Turton et al. (2018).

The bare module cost, C_{BM}, gives the cost of equipment while factoring in different materials of construction than carbon steel, pressures above ambient, and other expenses such as installation labor,

freight, insurance, taxes, construction overhead, and contractor engineering expenses. The bare module cost is related to C_p° by:

$$C_{BM} = C_p^\circ F_{BM} \quad \text{Eq 95}$$

where F_{BM} is the material factor which can be calculated differently depending on the type of equipment, as outlined in Turton et al. (2018).

The total module cost, C_{TM}, is calculated by:

$$C_{TM} = 1.33 \sum_{i=1}^{n} C_{BM} \quad \text{Eq 96}$$

where the sum of bare module costs is multiplied by factors for contingencies and fees. Typically, contingencies and fees of 15% and 3% are used for well-understood processes, respectively. However, since the technologies used in this process have been adapted from well-understood processes for a novel application, the contingency fee is doubled to 30% to account for the degree of uncertainty. The total module cost represents the cost of making small to moderate expansions or alterations to an existing facility.

The carbon processing plant will be an entirely new facility on undeveloped land, so the grassroots cost is calculated to account for site development, auxiliary buildings, and utilities. These terms are unaffected by the materials of construction or operating pressure of the process. These costs are assumed to be equal to 50% of the base bare module costs, C_{BM}°, which represents the bare module cost for equipment constructed of carbon steel and operated at ambient pressure. The grassroots cost, C_{GR}, is calculated by:

$$C_{GR} = C_{TM} + 0.50 \sum_{i=1}^{n} C_{BM,i}^\circ \quad \text{Eq 97}$$

Table 16 lists the estimates of C_p°, C_{BM}, and C_{BM}° for equipment in the carbon purification process along with data for their sizing parameter, A, and the material of construction (MOC) and discharge pressure for the pumps. Centrifugal pumps are used because they can handle slurries, and are constructed of stainless steel to handle the acidic conditions (Turton et al, 2018).

Table 16: Equipment Cost Data

Blenders	Type	Volume (cubic meters)	# Spares			Purchased Equipment Cost	Bare Module Cost	Base Bare Module Cost
CEMENTR	Rotary	1.25	0			$ 30,800	$ 34,500	$ 34,500
Drives	**Drive Type**	**Power (kilowatts)**	**# Spares**			**Purchased Equipment Cost**	**Bare Module Cost**	**Base Bare Module Cost**
D1	Electric - Totally Enclosed	2.36	0			$ 46,900	$ 70,300	$ 70,300
D2	Electric - Totally Enclosed	4.67	0			$ 46,900	$ 70,300	$ 70,300
Dryers	**Type**	**Area (square meters)**				**Purchased Equipment Cost**	**Bare Module Cost**	**Base Bare Module Cost**
DRYER	Rotary	32.8				$ 237,000	$ 296,000	$ 296,000
Filters	**Type**	**Area (square meters)**				**Purchased Equipment Cost**	**Bare Module Cost**	**Base Bare Module Cost**
RDVF-1	Disc And Drum	88				$ 676,000	$ 1,120,000	$ 1,120,000
RDVF-2	Disc And Drum	11				$ 287,000	$ 474,000	$ 474,000
Pump	**Type**	**Power (kilowatts)**	**# Spares**	**MOC**	**Discharge Pressure (barg)**	**Purchased Equipment Cost**	**Bare Module Cost**	**Base Bare Module Cost**
P1	Centrifugal	2.36	0	Stainless Steel	1.99	$ 12,400	$ 26,900	$ 17,600
P2	Centrifugal	4.68	0	Stainless Steel	3.99	$ 14,300	$ 31,200	$ 20,300
Reactors	**Type**	**Volume (cubic meters)**				**Purchased Equipment Cost**	**Bare Module Cost**	**Base Bare Module Cost**
LEACHR	Jacketed Agitated	27.5				$ 149,000	$ 596,000	$ 596,000
User Added Equipment	**Description**	**BMF_0**	**Actual BMF**			**Purchased Equipment Cost**	**Bare Module Cost**	**Base Bare Module Cost**
Grinder	Grinder	1	1			$ 556,713	$ 556,713	

4.2. Cost Estimate for Grinder

The cost estimate for the grinder is based on research by Sayadi et al. (2014) who developed a parametric cost model for six common mill types. Of all the functions tested, a power function showed the most consistency with the cost data for stirred mills. The cost of the stirred mill can be estimated by:

$$C_{mill} = a(kW)^b \quad \text{Eq 98}$$

where a=9031 and b=0.798 are constants determined by regression analysis specific to stirred mills. The cost estimate is based on 2010 USD, so the cost is adjusted using the chemical engineering plant cost index (CEPCI) for 2010 and 2023:

$$C_{mill,2023} = C_{mill,2010}\left(\frac{CEPCI_{2023}}{CEPCI_{2010}}\right) \quad \text{Eq 99}$$

where $CEPCI_{2010}$ is 551 and $CEPCI_{2023}$ is 798.

4.3. Uncertainties in Cost Estimation

The most significant uncertainty in the cost estimation of the carbon purification plant is the cost of the lift spray apparatus. Due to the novel design and application of this equipment, no basis of cost estimation is known to the authors of this work. Similarly, further studies on the PSD of cemented copper produced by the methods proposed in this paper are required in order to estimate the size and cost of the dryer. Since the cost of the carbon dryer is significant to the overall grassroots cost (see Table 17), it is expected that the cost of the copper dryer may be comparable.

Additionally, the size and cost of the granulation and dewatering processes is uncertain. However, the cost of the granulation tank is not expected to be significant and can be accounted for by the contingencies

included in the cost estimation. Similarly, the cost of the hydrocyclones is expected to be negligible and should be covered by the contingencies associated with the RDVF's.

4.4. Cost Estimation Results

The grassroots cost of the plant is estimated to be 5.98 MM$.[1] Table 17 provides a breakdown of C_{GR} by equipment type. The most costly items are the rotary drum vacuum filters (RDVF's 1 & 2), which account for 35% of the total grassroots cost. The second largest contributor to the grassroots cost is the auxiliary fees, which is just 50% of the base bare module cost of the equipment. Interestingly, other significant parts of the process such as the reactors and the grinder combined contribute less to the overall grassroots cost than the auxiliary fees. It is worth repeating that the cost of the lift spray apparatus and copper product dryer are not included in the breakdown and are expected to contribute significantly to the grassroots cost of the plant.

Table 17: Breakdown of grassroots cost by equipment type

Equipment Type	Contribution to C_{GR} MM$	Percent of CGR
Reactors (Leaching/Cementation)	0.839	0.140
Grinder	0.740	0.124
Pumps	0.264	0.044
Filters	2.120	0.354
Carbon Dryer	0.394	0.066
Auxiliary Facilities	1.628	0.272
Total	**5.98**	**1.00**

The price of carbon processing equipment per tonne of H_2 produced $C_{\frac{CProc}{tH2}}$ can be calculated to compare it with the price of hydrogen in order to get a relative sense of how much the price of carbon processing equipment will affect the economics of hydrogen production. The cost of carbon processing equipment at

[1] All costs are in USD.

the end of each year per year for a 5-year period $C_{C,year} = 2.00\ MM\$$ is calculated using the Capital Recovery Factor equation (Turton et al, 2018). This equation converts the present value (C_{Gr}) into equal annual payments, or annuities, while adjusting for the time value of money and an interest rate of *i*=20%.

$$C_{C,year} = C_{Gr}\frac{i(1+i)^5}{(1+i)^5-1} = 2.00\frac{MM\$}{year} \quad \text{Eq 100}$$

The cost of carbon processing equipment per tonne of H_2 produced $C_{\frac{CProc}{tH2}} = 257\frac{\$}{tonne\ H2}$ is calculated by:

$$C_{\frac{CProc}{tH2}} = \frac{C_{C,year}}{m_{H2/year}} \quad \text{Eq 101}$$

where $m_{H2/year} = 7782\frac{tonne}{year}$ is the mass flow rate of H_2 produced per year by the catalytic methane decomposition reactor in the design by Catalan and Rezaei (2022). The price of carbon processing equipment per tonne of H_2 produced, 257 \$/tonne H_2, is low compared to the price of hydrogen produced from natural gas which ranged from 1500 USD/tonne H_2 to 8000 USD/tonne H_2 in 2024 (International Energy Agency, 2024). This tells us that the hydrogen produced by methane pyrolysis in a liquid metal bubble column with a carbon purification process may be sold at a competitive price when compared to hydrogen produced by conventional methods.

5. Conclusions

Catalytic methane pyrolysis using molten alloys in a liquid metal bubble reactor has demonstrated potential to significantly lower the CO_2 emissions associated with industrial hydrogen production. One remaining caveat to unlocking its potential is the need for a way to recover metal alloys lost in the process of removing carbon from the methane pyrolysis reactor. For a Cu-Bi alloy, different methods are required to recover each metal from the carbon.

Bismuth has a relatively high vapor pressure so it can be sufficiently removed using vacuum distillation. Vacuum distillation is advantageous from an environmental perspective because it does not produce any wastewater. The rate of bismuth removal increases with the temperature, available surface area, and with decreasing pressure. The temperature and pressure are limited by the available materials of construction and ejector stages, respectively. The available surface area can be increased by adapting a lift-spray apparatus to spray the molten solids mixture into a vacuum chamber. In this work, the bismuth content of the final carbon product was reduced to 0.31 wt% by processing the solids at 1500 K, 30 Pa, and with 14 risers in the lift-spray apparatus.

Copper can be removed sufficiently by leaching in aqueous sulfuric acid solution. The rate of carbon leaching increases with temperature and pressure and with decreasing copper particle radius. In this work, the copper content of the final carbon product was reduced to 0.15 wt% by leaching 50 μm particles at atmospheric pressure in a 27.51 m^3 vessel with 4.16 MW of heat supplied by a jacketed reactor. The downside to copper leaching is the significant quantities of leaching solution produced that require processing to recover the copper as metal and treatment for the contaminated water to be recirculated in the process.

The final carbon product of this work is 98.9 wt% carbon on a dry basis, which meets the specifications for rubber-grade carbon black, which is typically >97 wt% carbon on a dry basis. The moisture content of the carbon product is 1.28 wt% H_2O, which is less than the maximum moisture content listed in carbon black datasheets of 1.5 wt%.

When comparing the cost of carbon processing equipment per tonne of H_2 produced ($C_{\frac{CProc}{tH2}} = 257 \frac{\$}{tonne\ H2}$) to the price at which hydrogen is typically sold, 1500-8000 USD/tonne H_2, the cost of carbon processing is relatively small. This allows for the hydrogen produced by methane pyrolysis to be sold at a

competitive price in comparison to hydrogen produced by conventional methods, or other low-carbon hydrogen technologies such as electrolysis.

These results show that the $Cu_{0.45}Bi_{0.55}$ catalyst lost when removing carbon from liquid metal bubble reactors for methane pyrolysis can be recovered in a carbon purification process. Based on the information provided, the additional costs associated with carbon processing are not expected to significantly impact the economic performance of catalytic methane pyrolysis. However, there are some additional challenges requiring further research:

- Development of a liquid phase mass transport model for droplets sprayed into a vacuum distillation chamber.
- Research the drying rates of carbon produced by methane pyrolysis to develop drying curves.
- Testing of different carbon removal methods and carbon product characterization for a liquid metal bubble reactor of industrial scale.
- Development and testing of a lift-spray apparatus for the application of removing bismuth from carbon contaminated with Cu and Bi. Additionally, testing the purity of the bismuth recovered.
- Formulation of a methodology to estimate the capital cost of a lift-spray apparatus for the removal of bismuth from the carbon product.

6. References

Copper, Cu; Annealed. (2024). Matweb. https://www.matweb.com/search/datasheet_print.aspx?matguid=9aebe83845c04c1db5126fada6f76f7e

Abánades, A., Ruiz, E., Ferruelo, E. M., Hernández, F., Cabanillas, A., Martínez-Val, J. M., Rubio, J. A., López, C., Gavela, R., Barrera, G., Rubbia, C., Salmieri, D., Rodilla, E., & Gutiérrez, D. (2011). Experimental analysis of direct thermal methane cracking. *International Journal of Hydrogen Energy*, *36*(20), 12877–12886. https://doi.org/10.1016/j.ijhydene.2011.07.081

Abbas, H. F., & Wan Daud, W. M. A. (2010). Hydrogen production by methane decomposition: A review. In *International Journal of Hydrogen Energy* (Vol. 35, Issue 3, pp. 1160–1190). https://doi.org/10.1016/j.ijhydene.2009.11.036

Allaire, A. (1991). *Copper Matte Vacuum Purification*. McGill University.

Allaire, A., & Harris, R. (1989a). *Vacuum Distillation of Copper Matte to Remove Lead, Arsenic, Bismuth, and Antimony*.

Allaire, A., & Harris, R. (1989b). Vacuum Distillation of Copper Matte to Remove Lead, Arsenic, Bismuth, and Antimony. *Metallurgical Transactions B*, *20B*. https://doi.org/654

Angikath, F., Abdulrahman, F., Yousry, A., Das, R., Saxena, S., Behar, O., Alhamed, H., Altmann, T., Dally, B., & Sarathy, S. M. (2024). Technoeconomic assessment of hydrogen production from natural gas pyrolysis in molten bubble column reactors. *International Journal of Hydrogen Energy*, *49*, 246–262. https://doi.org/10.1016/j.ijhydene.2023.07.308

Aspen Technology, Inc. (2023). *Aspen Plus V14 help documentation* (14).

BOKELA. (2025). *Vacuum Filtration With a Drum Filter*. BOKELA. https://www.bokela.com/en/bovac-drum

Boo, J., Ko, E. H., Park, N. K., Ryu, C., Kim, Y. H., Park, J., & Kang, D. (2021). Methane pyrolysis in molten potassium chloride: An experimental and economic analysis. *Energies*, *14*(23). https://doi.org/10.3390/en14238182

Butler, J. A. V. (1932). *The Thermodynamics of the Surfaces of Solutions*. *135*(827), 348–375. https://doi.org/https://doi.org/10.1098/rspa.1932.0040

Catalan, L. J. J., & Rezaei, E. (2022). Modelling the hydrodynamics and kinetics of methane decomposition in catalytic liquid metal bubble reactors for hydrogen production. *International Journal of Hydrogen Energy*, *47*(12), 7547–7568. https://doi.org/10.1016/j.ijhydene.2021.12.089

Catalan, L. J. J., Roberts, B., & Rezaei, E. (2023). A low carbon methanol process using natural gas pyrolysis in a catalytic molten metal bubble reactor. *Chemical Engineering Journal*, *462*. https://doi.org/10.1016/j.cej.2023.142230

Chen, Y., Yang, B., Xu, B., & Yang, H. W. (2019). Experimental investigation and modeling of phase equilibria for Cu-Bi and Cu-Bi-Sb alloys in vacuum distillation. *Fluid Phase Equilibria*, *490*, 86–91. https://doi.org/10.1016/j.fluid.2019.03.003

Copper_Cementation_in_a_Revolving_drum_R. (n.d.).

Couper, J. R., Penney, W. R., Fair, J. R., & Walas, S. M. (2005). *Chemical Process Equipment: Selection and Design* (2nd ed.). Elsevier Inc.

Database of thermophysical properties of liquid metal coolants for GEN-IV. (2024). http://www.sckcen.be

DCL Corporation. (2020). *410 Carbon Black TDS (Technical Data Sheet)*. https://www.pigments.com/wp-content/uploads/410_CARBON_BLACK_EN_TDS.pdf

Dean, K. C., Groves, R. D., & May, S. L. (1968). *Copper Cementation using Automobile Scrap in a Rotating Drum*. https://doi.org/123456

Dewey, C. S., Lefforge, P. K., & Cabot, G. L. (1932). Moisture Sorption by Carbon Black. *Industrial and Engineering Chemistry*, *24*, 1045–1050.

Dutta, B. K. (2009). *Principles of Mass Transfer and Separation Processes*. Asoke K. Ghosh.

Fisher, W. W., & Groves, R. D. (1976). *Copper Cementation in a Revolving-Drum Reactor, A Kinetic Study*.

Geißler, T., Abánades, A., Heinzel, A., Mehravaran, K., Müller, G., Rathnam, R. K., Rubbia, C., Salmieri, D., Stoppel, L., Stückrad, S., Weisenburger, A., Wenninger, H., & Wetzel, T. (2016). Hydrogen production via methane pyrolysis in a liquid metal bubble column reactor with a packed bed. *Chemical Engineering Journal*, *299*, 192–200. https://doi.org/10.1016/j.cej.2016.04.066

Geißler, T., Plevan, M., Abánades, A., Heinzel, A., Mehravaran, K., Rathnam, R. K., Rubbia, C., Salmieri, D., Stoppel, L., Stückrad, S., Weisenburger, A., Wenninger, H., & Wetzel, T. (2015). Experimental investigation and thermo-chemical modeling of methane pyrolysis in a liquid metal bubble column reactor with a packed bed. *International Journal of Hydrogen Energy*, *40*(41), 14134–14146. https://doi.org/10.1016/j.ijhydene.2015.08.102

Granulated blast slag (GBS). (2024). Mineral Products Association (MPA). https://www.mineralproducts.org/Mineral-Products/Slag/Granulated-blast-slag.aspx#:~:text=Large%20volumes%20of%20water%20are,water%20for%20cooling%20and%20reuse.

Haffez, G. S. A. (2012). CORRELATION BETWEEN BOND WORK INDEX AND MECHANICAL PROPERTIES OF SOME SAUDI ORES. In *Journal of Engineering Sciences* (Vol. 40, Issue 1).

Harris, R. (1984). Vacuum Refining Copper Melts to Remove Bismuth, Arsenic, and Antimony. *Metallurgical Transactions B*, *15B*.

Harris, R., & Davenport, W. G. (1982). Vacuum Distillation of Liquid Metals: Part I. Theory and Experimental Study. *Metallurgical Transactions B*, *13B*.

Harris, R., & Davenport, W. G. (1984). Vacuum Purification of Liquid Metals (Patent 4456479). In *J.Vac.Sci.Technol* (4456479).

Herbertson, J., & Harris, R. (1985). Kinetics of Electron-Beam Refining of Liquid Metals. *8th Ann. IVCM*, 273–282.

Huang, Q., Noble, A., & Talan, D. (2022). Exploratory investigation on the use of low-cost alternative media for ultrafine grinding of coal. *International Journal of Coal Preparation and Utilization*, *42*(7), 2127–2144. https://doi.org/10.1080/19392699.2020.1809387

INBA System Slag Granulation with Continuous Dewatering and Pollution Control. (2015). In *Ironmaking*. Paul Wurth SMS group.

International Energy Agency. (2024). *Global Hydrogen Review 2024*. www.iea.org

Jhajharia, R., Jain, D., Sengar, A., Goyal, A., & Soni, P. R. (2016). Synthesis of copper powder by mechanically activated cementation. *Powder Technology*, *301*, 10–15. https://doi.org/10.1016/j.powtec.2016.05.031

Kang, D., Palmer, C., Mannini, D., Rahimi, N., Gordon, M. J., Metiu, H., & McFarland, E. W. (2020). Catalytic Methane Pyrolysis in Molten Alkali Chloride Salts Containing Iron. *ACS Catalysis*, *10*(13), 7032–7042. https://doi.org/10.1021/acscatal.0c01262

Kang, D., Rahimi, N., Gordon, M. J., Metiu, H., & McFarland, E. W. (2019). Catalytic methane pyrolysis in molten MnCl2-KCl. *Applied Catalysis B: Environmental*, *254*, 659–666. https://doi.org/10.1016/j.apcatb.2019.05.026

Kim, T., Lee, J., Ko, Y., Chong, G. H., Kang, D., & Kwon, H. (2025). Catalytic molten Zn-Bi alloys for methane pyrolysis. *Chemical Engineering Journal*, *509*. https://doi.org/10.1016/j.cej.2025.161304

Leal Pérez, B. J., Medrano Jiménez, J. A., Bhardwaj, R., Goetheer, E., van Sint Annaland, M., & Gallucci, F. (2021). Methane pyrolysis in a molten gallium bubble column reactor for sustainable hydrogen production: Proof of concept & techno-economic assessment. *International Journal of Hydrogen Energy*, *46*(7), 4917–4935. https://doi.org/10.1016/j.ijhydene.2020.11.079

Lee, H. S. (1988). *SPRAY GENERATION BY GAS-LIFT PUMPS*. McGill University.

Leyser, P., & Cortina, C. (2006). INBA® slag granulation system with environmental control of water and emissions. In *Millennium Steel*. Paul WURTH S.A.

Lu, B., & Graydon, W. F. (1953). The Rate of Dissolution of Copper. *Canadian Journal Of Chemistry*, *32*.

Matsumoto, T., Fujii, H., Ueda, T., Kamai, M., & Nogi, K. (2005). Measurement of surface tension of molten copper using the free-fall oscillating drop method. *Measurement Science and Technology*, *16*(2), 432–437. https://doi.org/10.1088/0957-0233/16/2/014

McCabe, W. L., Smith, J. C., & Harriott, P. (2004). *Unit Operations of Chemical Engineering* (7th ed.). McGraw Hill.

Mcdonald, I. J., & Werner, A. (2015, August). DRY SLAG GRANULATION WITH HEAT RECOVERY. *Seminário de Redução de Minério de Ferro e Matérias-Primas*.

Metso Outotec. (2021). *Basics in Minerals Processing* (12th ed.).

Micronics Engineered Filtration Group, Inc. (2025). *Rotary Drum Vacuum Filters*. https://www.micronicsinc.com/vacuum-filtration/filtration-equipment/rotary-drum-vacuum-filters/

M.J. Assael, A.E. Kalyva, K.D. Antoniadis, R. Michael Banish, I. Egry, J. Wu, E. Kaschnitz, & W.A. Wakeham. (2010). Reference data for the density and viscosity of liquid copper and liquid tin. *J. Phys. Chem. Ref. Data.*, *39*.

Mordor Intelligence. (2025). *Carbon Black Market Report - Industry Growth, Size & Forecast Analysis (2025 - 2030)* . Mordor Intelligence. https://www.mordorintelligence.com/industry-reports/carbon-black-market

Mujumdar, A. S. (2006). *Handbook of Industrial Drying* (3rd ed.). Taylor & Francis Group, LLC.

Muradov, N. (2017). Low to near-zero CO2 production of hydrogen from fossil fuels: Status and perspectives. In *International Journal of Hydrogen Energy* (Vol. 42, Issue 20, pp. 14058–14088). Elsevier Ltd. https://doi.org/10.1016/j.ijhydene.2017.04.101

Nagamori, M., Mackey, P. J., & Tarassoff, P. (n.d.). *Copper Solubility in FeO-Fe203-SiO2-AI203 Slag and Distribution Equilibria of Pb, Bi, Sb and As Between Slag and Metallic Copper*.

Nagata, K. et al. (1979). *Producing gypsum and magnetite from ferrous sulfate and separating* (Patent 4137293).

Neikov, O. D., Naboychenko, S. S., & Dowson, G. (2009). *Handbook of non-ferrous metal powders: Technologies and Applications*. Elesvier.

Ozberk, E. (1980). *VACUUM REFINING OF COPPER*. McGill University.

Ozberk, E., & Guthrie, R. I. L. (1986). A Kinetic Model for the Vacuum Refining of Inductively Stirred Copper Melts. *Metallurgical Transactions B*, *17B*.

Palmer, C., Bunyan, E., Gelinas, J., Gordon, M. J., Metiu, H., & McFarland, E. W. (2020). CO2-free hydrogen production by catalytic pyrolysis of hydrocarbon feedstocks in molten Ni-Bi. *Energy and Fuels*, *34*(12), 16073–16080. https://doi.org/10.1021/acs.energyfuels.0c03080

Palmer, C., Tarazkar, M., Gordon, M. J., Metiu, H., & Mcfarland, E. W. (2021). Methane pyrolysis in low-cost, alkali-halide molten salts at high temperatures. *Sustainable Energy and Fuels*, *5*(23), 6107–6123. https://doi.org/10.1039/d1se01408k

Palmer, C., Tarazkar, M., Kristoffersen, H. H., Gelinas, J., Gordon, M. J., McFarland, E. W., & Metiu, H. (2019). Methane Pyrolysis with a Molten Cu-Bi Alloy Catalyst. *ACS Catalysis*, *9*(9), 8337–8345. https://doi.org/10.1021/acscatal.9b01833

Parkinson, B., Balcombe, P., Speirs, J. F., Hawkes, A. D., & Hellgardt, K. (2019). Levelized cost of CO 2 mitigation from hydrogen production routes. *Energy and Environmental Science*, *12*(1), 19–40. https://doi.org/10.1039/c8ee02079e

Parkinson, B., Matthews, J. W., McConnaughy, T. B., Upham, D. C., & McFarland, E. W. (2017). Techno-Economic Analysis of Methane Pyrolysis in Molten Metals: Decarbonizing Natural Gas. *Chemical Engineering and Technology*, *40*(6), 1022–1030. https://doi.org/10.1002/ceat.201600414

Parkinson, B., Patzschke, C. F., Nikolis, D., Raman, S., Dankworth, D. C., & Hellgardt, K. (2021). Methane pyrolysis in monovalent alkali halide salts: Kinetics and pyrolytic carbon properties. *International Journal of Hydrogen Energy*, *46*(9), 6225–6238. https://doi.org/10.1016/j.ijhydene.2020.11.150

Parkinson, B., Tabatabaei, M., Upham, D. C., Ballinger, B., Greig, C., Smart, S., & McFarland, E. (2018). Hydrogen production using methane: Techno-economics of decarbonizing fuels and chemicals. *International Journal of Hydrogen Energy*, *43*(5), 2540–2555. https://doi.org/10.1016/j.ijhydene.2017.12.081

Patnaik, T., & Brown, B. (2010). *Carbon black: why quality matters Executive summary*. www.rubbernews.com

Poço, J. G. R., Guardani, R., Shimmi, C. S., & Giulietti, M. (2006). Production of metallic copper powder by autocatalytic reaction in suspension. *Materials Research*, *9*(2), 131–135. https://doi.org/10.1590/S1516-14392006000200004

Pruvost, F., Cloete, S., Hendrik Cloete, J., Dhoke, C., & Zaabout, A. (2022). Techno-Economic assessment of natural gas pyrolysis in molten salts. *Energy Conversion and Management*, *253*. https://doi.org/10.1016/j.enconman.2021.115187

Rahimi, N., Kang, D., Gelinas, J., Menon, A., Gordon, M. J., Metiu, H., & McFarland, E. W. (2019). Solid carbon production and recovery from high temperature methane pyrolysis in bubble columns containing molten metals and molten salts. *Carbon*, *151*, 181–191. https://doi.org/10.1016/j.carbon.2019.05.041

Rostrup-Nielsen, J., & Christiansen, L. J. (2011). *Concepts in Syngas Manufacture* (G. J. Hutchings, Ed.; Vol. 10). Imperial College Press.

Sayadi, A. R., Khalesi, M. R., & Khosfarman, M. (2014). A parametric cost model for mineral grinding mills. *Minerals Engineering*, *55*, 96–102. https://doi.org/10.1016/j.mineng.2013.09.013

Scheiblehner, D., Neuschitzer, D., Wibner, S., Sprung, A., & Antrekowitsch, H. (2023). 2023_-_Scheiblehner et al. Hydrogen production by methane pyrolysis in molten binary copper alloys. *International Journal of Hydrogen Energy*, *48*, 6233–6243.

Schlesinger, M. E., King, M. J., Sole, K. C., & Davenport, W. G. (2011). *Extractive Metallurgy of Copper* (Fifth). Elsevier.

Schlesinger, & Mark E. (2011). *Extractive Metallurgy of Copper* (Fifth).

Serban, M., Lewis, M. A., Marshall, C. L., & Doctor, R. D. (2003). Hydrogen production by direct contact pyrolysis of natural gas. *Energy and Fuels*, *17*(3), 705–713. https://doi.org/10.1021/ef020271q

Speiser, R., Poirer, D. R., & Yeum, K. (1987). Surface Tension of Binary Liquid Alloys. *Script. Met.* , *21*, 687.

Steinberg, M. (1999). Fossil fuel decarbonization technology for mitigating global warming. *International Journal of Hydrogen Energy*, *24*(8), 771–777. https://doi.org/10.1016/S0360-3199(98)00128-1

Stirred Mills . (2024). Metso: Outotec. https://www.metso.com/globalassets/pdfs-and-other-downloads/stirred-mills-brochure_lowres.pdf

Tanaka, T., & Hack, K. (2001). Calculation of Surface Tension of Liquid Bi-Sn Alloy using Thermochemical Application Library ChemApp. *Calphad*, *24*, 465–474.

Tighzert, H., Brahimi, M., Kechroud, N., & Benabbas, F. (2013). Effect of submergence ratio on the liquid phase velocity, efficiency and void fraction in an air-lift pump. *Journal of Petroleum Science and Engineering*, *110*, 155–161. https://doi.org/10.1016/j.petrol.2013.08.047

Treybal, R. E. (1981). *Mass-Transfer Operations* (Third). McGraw-Hill.

Turton et al. (2018). *Analysis, Synthesis, and Design of Chemical Processes* (Fifth). Pearson Education, Inc.

Upham, D. C., Agarwal, V., Khechfe, A., Snodgrass, Z. R., Gordon, M. J., Metiu, H., & McFarland, E. W. (2017). Catalytic molten metals for the direct conversion of methane to hydrogen and separable carbon. *Science*, *358*(6365), 917–921. https://doi.org/10.1126/science.aao5023

Upham, D. C., Agarwal, V., Khechfe, A., Snodgrass, Z. R., Gordon, M. J., Metiu, H., & Mcfarland, E. W. (2017). *Catalytic molten metals for the direct conversion of methane to hydrogen and separable carbon*. *358*(6365), 917–921. https://doi.org/10.2307/26400857

U.S. EPA. (2023). *Water Treatment Chemical Supply Chain Profile - Ferrous Sulfate*. https://www.epa.gov/system/files/documents/2023-03/Ferrous%20Sulfate%20Supply%20Chain%20Profile_0.pdf

Vacuum and pressure drum filters, YU and PYU. (2024). Andritz. https://www.andritz.com/products-en/group/separation/disc-drum-filters/vacuum-drum-filter-yu

Van Stein Callenfels, E., & Van Ikelen, J. (2003). *SLAG GRANULATION SYSTEMS FOR BLAST FURNACES*.

Vertimill. (2024). Metso. https://www.metso.com/portfolio/vertimill/

Von Wald, G. A., Masnadi, M. S., Upham, D. C., & Brandt, A. R. (2020). Optimization-based technoeconomic analysis of molten-media methane pyrolysis for reducing industrial sector CO2emissions. *Sustainable Energy and Fuels*, *4*(9), 4598–4613. https://doi.org/10.1039/d0se00427h

Walker, A. (2017). *Data Requirement for a Rotary Drum Vacuum Filter*. www.filtrationservices.co.uk

Y. Wang, M.J., R., S.A., M., & K., K. (2001). *Kirk-Othmer Encyclopedia of Chemical Technology: Vol. Volume 4*. Wiley.

Yeum, D. R., Speiser, R., & Poirier. (1989). Estimations of the Surface Tensions of Binary Liquid Alloys. *Met. Trans. B.*, *20B*, 693.

Appendix A

Correlations for φ_{Bi}°, P_{Bi}°, and P_{Cu}°

$$log\varphi_{Bi}^{\circ} = 1900T^{-1}(K) - 0.885 \quad \text{(Nagamori et al., n.d.)}$$

$$logP_{Bi}^{\circ} = -10400T^{-1}(K) - 1.26logT(K) + 12.35\ mmHg \quad \text{(Ozberk, 1980)}$$

$$logP_{Cu}^{\circ} = -17520T^{-1}(K) - 1.21logT(K) + 13.21\ mmHg \quad \text{(Ozberk, 1980)}$$

Appendix B

Predicted K_U values by Equation 11

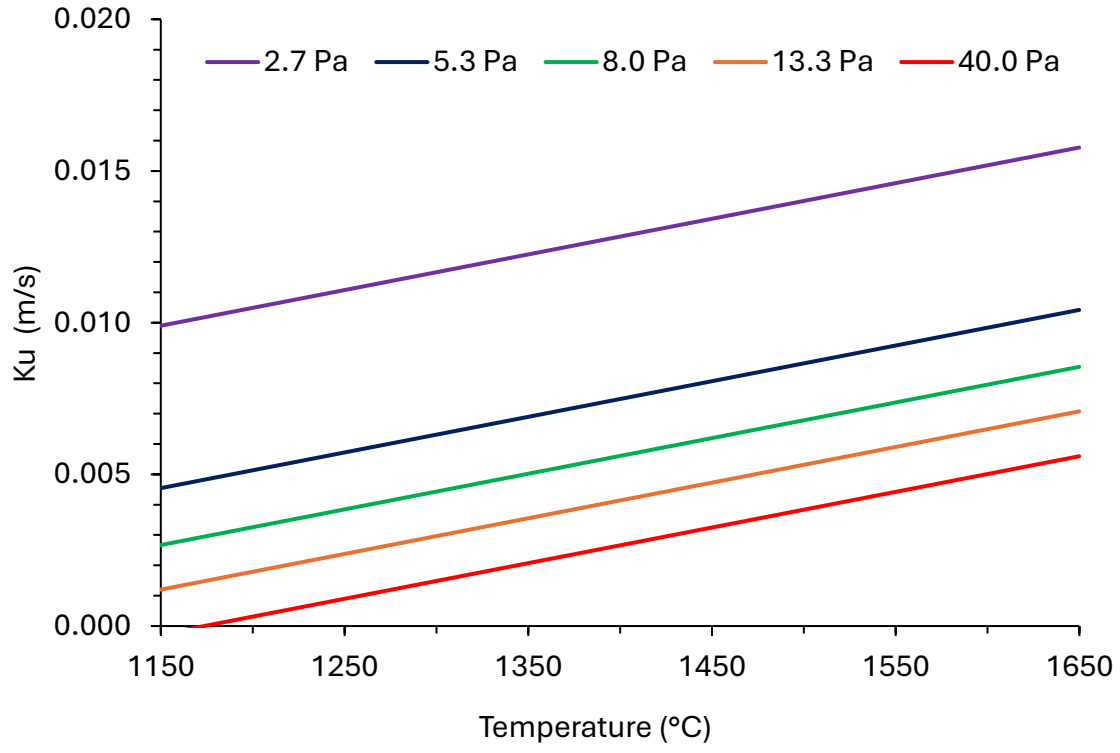

Figure B1: Ku (m/s) versus temperature (°C) for varied pressures as predicted by Equation 11.

Validation of bismuth overall mass transfer rate calculations (K)

Ozberk & Guthrie (Ozberk & Guthrie, 1986) conducted experiments to develop a kinetic model for the vacuum refining of inductively stirred copper melts. The overall mass transfer rate constant, K was obtained from experiments conducted at various temperatures and pressures. Figure B2 illustrates the calculated values for K using the model presented in section 2.1.2 at the experimental conditions selected by Ozberk & Guthrie. As explained in section 2.1.2, K is a function of K_L, K_E, and K_U, calculated using Equations 3 through 7 in this work. Figure B2 shows an acceptable fit between the calculated values of K and those obtained experimentally.

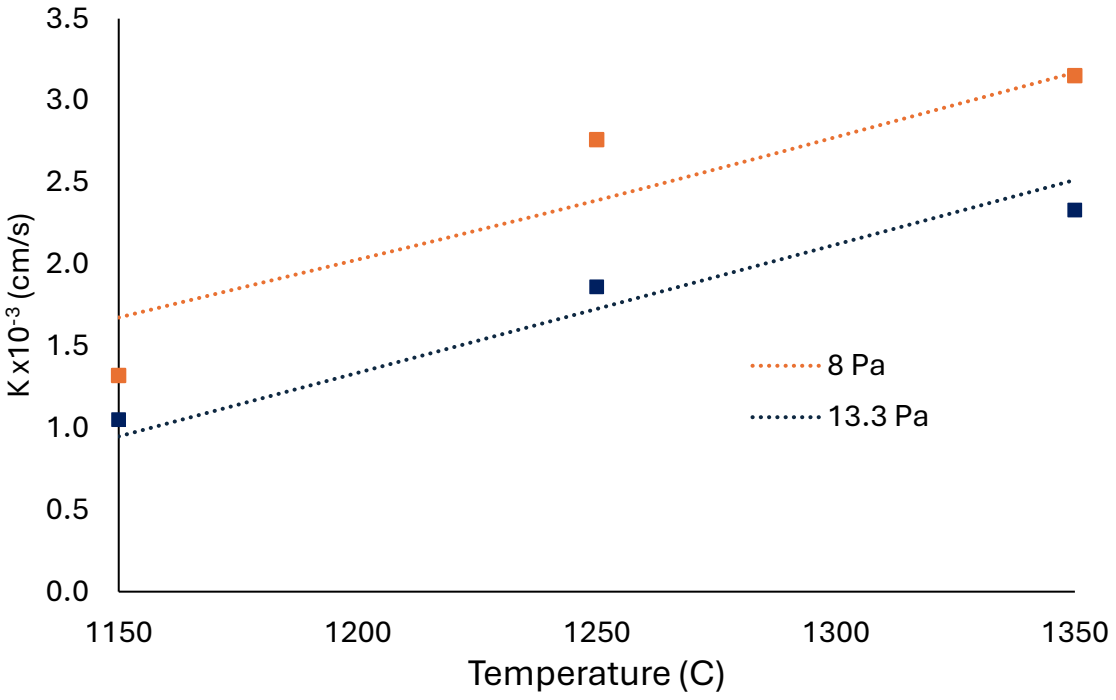

Figure B2: Calculated versus experimental values of the overall bismuth mass transfer rate (K) at 8 and 13.3 Pa.

Appendix C

Rate of Bismuth Removal

Equation 17, the rate of bismuth removal ($kg_{Bi}s^{-1}$) contains a term for C_{Bi}^{B}, the concentration of bismuth in the melt ($kg_{Bi}m^{-3}_{melt}$), which can be written in terms of m_{Bi} and V_{melt}, as shown below in Equation C1.

$$r_{Bi} = KA_{droplets}C_{Bi}^{B} \quad \text{Eq 17}$$

$$r_{Bi} = KA_{droplets}\frac{m_{Bi}}{V_{melt}} \quad \text{Eq C1}$$

Equation C1 can be substituted into the batch reactor mass balance equation as shown below. Where m_{Bi} is the mass of bismuth in the melt and t is the vacuum distillation time.

$$\frac{dm_{Bi}}{dt} = -r_{Bi} = -KA_{droplets}\frac{m_{Bi}}{V_{melt}} \quad \text{Eq C2}$$

V_{melt} (Equation 39) accounts for the change in melt volume that occurs as bismuth is removed, especially for melts with a high bismuth content. Equation 36 can be substituted into Equation C2 to obtain Equation 37.

$$V_{melt} = V_0 - \left[\frac{m_{Bi,0} - m_{Bi,t}}{\rho_{Bi}}\right] \quad \text{Eq 36}$$

$$\frac{dm_{Bi}}{dt} = -\mathrm{KA_{droplets}m_{Bi}}\left[V_0 - \frac{m_{Bi,0} - m_{Bi,t}}{\rho_{Bi}}\right]^{-1} \quad \text{Eq 37}$$

Appendix D

Concentration of sulfuric acid solution

Sulfuric acid in aqueous form dissociates into its ions by:

$$H_2SO_4 \leftrightarrow 2H^+ + SO_4^{2-} \quad \text{Eq D1}$$

Copper leaching occurs when the H^+ ions react with $Cu_{(s)}$ and O_2 by:

$$Cu_{(s)} + 2H^+ + 0.5O_2 \rightarrow Cu^{2+} + H_2O \quad \text{Eq 43}$$

However, H^+ can also react by complexation to form bisulfate ions:

$$H^+ + SO_4^{2-} \leftrightarrow HSO_4^- \quad \text{Eq D2}$$

thus affecting the amount of sulfuric acid to be added to the system to maintain a pH of 1. Figure D1 illustrates the species entering and exiting the leaching vessel.

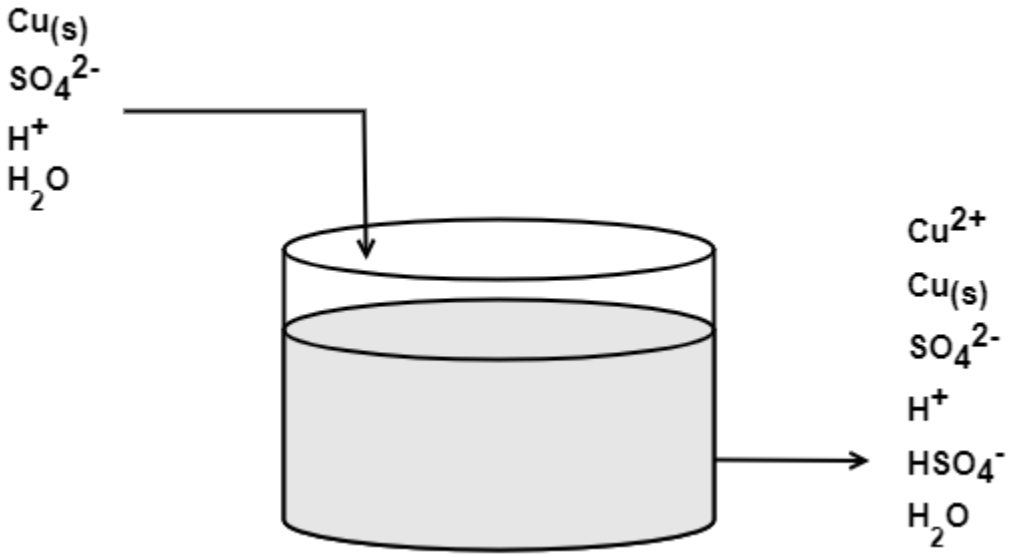

Figure D1: Leaching Vessel Species and Reactions

Because H^+ can react by both Equations 43 and D2, Aspen Plus is used in this work to predict the speciation in the reactor. A mole balance on the components $H^+_{comp\ out}$, $SO^{2-}_{4,comp\ out}$, and $H_2O_{comp\ out}$ is used to predict their molar flows at the outlet of the reactor. The number of moles of each component is equal to the sum of moles of its species as follows:

$$H^+_{comp\ out} = H^+ + HSO_4^- + 2H_2SO_4 \quad \text{Eq D3}$$

$$SO^{2-}_{4,comp\ out} = SO_4^{2-} + HSO_4^- + H_2SO_4 \quad \text{Eq D4}$$

$$H_2O_{comp\ out} = H_2O_{comp\ in} + Cu^{2+}_{comp\ out} \quad \text{Eq D5}$$

After calculating the mole flows of each component at the outlet, they are specified as the inputs to a stream in Aspen Plus, which uses an electrolyte fluid package to predict the speciation of the components in the stream, thereby providing a more accurate prediction of the pH inside the reactor.

For example, the methane decomposition reactor in Catalan & Rezaei (2022) produces 122.4 mol s^{-1} of H_2. Based on the stoichiometry of methane decomposition, this results in a carbon flow rate of 61.2 mol s^{-1} or 0.735 kg s^{-1}. The mass flow rate of solids, $\dot{m}_s$, to the copper leaching reactor can be calculated by:

$$\dot{m}_s = \frac{\dot{m}_c}{(1 - Y_{Cu})} \quad \text{Eq D6}$$

The mass fraction of copper in the solids, $Y_{Cu} = 0.428$, is estimated based on Rahimi et al.'s analysis of copper produced from methane pyrolysis using a Ni-Bi molten metal catalyst in a bubble column (Rahimi et al., 2019). It is assumed that the Ni content of the carbon in Rahimi's samples is comparable to the copper content of the carbon in this work. The molar flow rate of copper in the feed is therefore:

$$Cu_{(s)_{in}} = \frac{\dot{m}_S Y_{Cu}}{MW_{Cu}} \quad \text{Eq D7}$$

The molar flow of Cu^{2+} at the outlet can be determined using the solid copper conversion, X_{Cu}, and the molar flow of metallic copper in the reactor inlet, $Cu_{(s)}$, by:

$$Cu^{2+}_{comp\ out} = X_{Cu} Cu_{(s)_{in}} \quad \text{Eq D8}$$

An initial estimate for the molar flow rate of $H^+_{comp\ out}$ is made. Based on this value, $SO^{2-}_{4,comp\ out}$ at the outlet is calculated by:

$$SO^{2-}_{4,comp\ out} = 0.5H^+_{comp\ out} + Cu^{2+}_{comp\ out} \quad \text{Eq D9}$$

The $SO_{4,comp\ out}^{2-} = SO_{4,comp\ in}^{2-}$, and the stoichiometric relationships in Equation D1 are used to calculate the molar flow of H_2SO_4 at the inlet. Next, the water flow rates at the inlet and outlet are calculated. The molar flow rate of water in the feed is calculated by:

$$H_2O_{in} = \frac{\left(\frac{\dot{m}_s}{x_{s,i}}\right) - \dot{m}_{H2SO4}}{MW_{H2O}} \quad \text{Eq D10}$$

where $\dot{m}_{H2SO4}$ is the mass flow rate of H_2SO_4 at the inlet, and the solids-to-liquid mass ratio at the inlet, $x_{s,i} = 0.15$, is based on typical feed slurry compositions to flotation cells used in the mineral processing industry (Schlesinger et al., 2011). Water is produced by Equation 43, so the moles of H_2O_{comp} produced are equal to the moles of $Cu_{comp\ out}^{2+}$. The molar flow rate of water at the outlet is the sum of $Cu_{comp\ out}^{2+}$ from equation D8 and H_2O_{in} from equation D10:

$$H_2O_{comp\ out} = X_{Cu}Cu_{(s)_{in}} + \frac{\left(\frac{\dot{m}_s}{x_{s,i}}\right) - \dot{m}_{H2SO4}}{MW_{H2O}} \quad \text{Eq D11}$$

The mole flows of $Cu_{comp\ out}^{2+}$, $SO_{4,comp\ out}^{2-}$, and $H_2O_{comp\ out}$ at the outlet can be calculated for a specified $x_{s,i}$, $Cu_{(s)}$, X_{Cu}, and mole flow of $H_{comp\ out}^{+}$ at the outlet. The simulation specifications and stream inputs for the example based on Catalan & Rezaei (2022) are summarized in Table D1.

Table D1: Reactor and Outlet Stream Specifications for Copper Leaching Vessel

Stream Specification	**Value**	**Units**
$\dot{m}_c$	0.735	kg/s
Y_{Cu}	0.428	kg_{Cu}/kg_S
$\dot{m}_s$	1.282	kg_s/s
$Cu_{(s)}$	8.61	mol/s
$x_{s,i}$	0.15	kg_s/kg_{liq}
X_{Cu}	0.998	-
$H^+_{comp\ out}$	16.2	mol/s
Component Mole Flows		
$Cu^{2+}_{comp\ out}$	8.6	mol/s
$H^+_{comp\ out}$	16.2	mol/s
$SO^{2-}_{4,comp\ out}$	16.7	mol/s
$H_2O_{comp\ out}$	392.4	mol/s

Aspen Plus then calculates the molar flows of each species at the outlet, summarized below in Table D2. Using trial and error, $H^+_{comp\ out}$ is adjusted until the simulation calculates a pH of 1 in the outlet stream. The simulation results predict 14.17 mol/s of HSO_4^- at the outlet. In order to maintain a pH of 1, $H^+_{comp\ out}$ was increased to overcome the effect of HSO_4^- formation in the system. Based on these results, the required flow rate of H_2SO_4 in the feed is determined to be 16.7 mol/s.

Table D2: Aspen Plus Simulation Results

Component	Mole Flow (mol/s)
H_2O	392.7
$CuSO_4$	0
H_2SO_4	9.85×10^{-8}
Cu^{2+}	8.60
H^+	2.03
OH^-	5.55×10^{-11}
HSO_4^-	14.17
SO_4^{2-}	2.53

Appendix E

Validation of Lu & Graydon (1953) kinetic model in SI units

Experimental data from Lu & Graydon's experiments was converted to SI units and plotted alongside the predictions of the kinetic model (Eq-40). Parameters studied were the effect of O_2 concentration, effect of temperature, and the effect of sample area and solution volume. The article also discusses the negligible effects of agitator speed, and of increasing the solution pH below 1. Recall that the kinetic model is applicable for a pH value of 1.

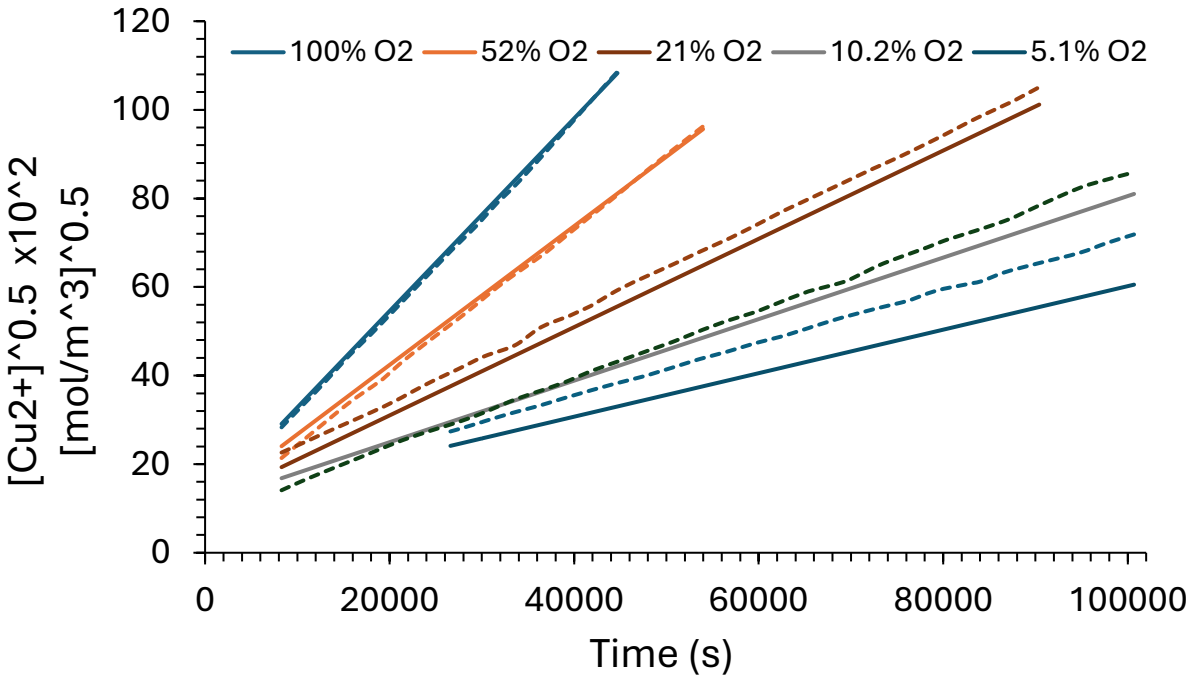

Figure E1: Effect of O_2 concentration on $Cu_{(s)}$ dissolution. The square of Cu^{2+} concentration $(mol/m^3)^{0.5}$ $x10^2$ versus time (s) for varying O_2 concentrations (%). Solid lines represent kinetic model predictions, dashed lines represent experimental data.

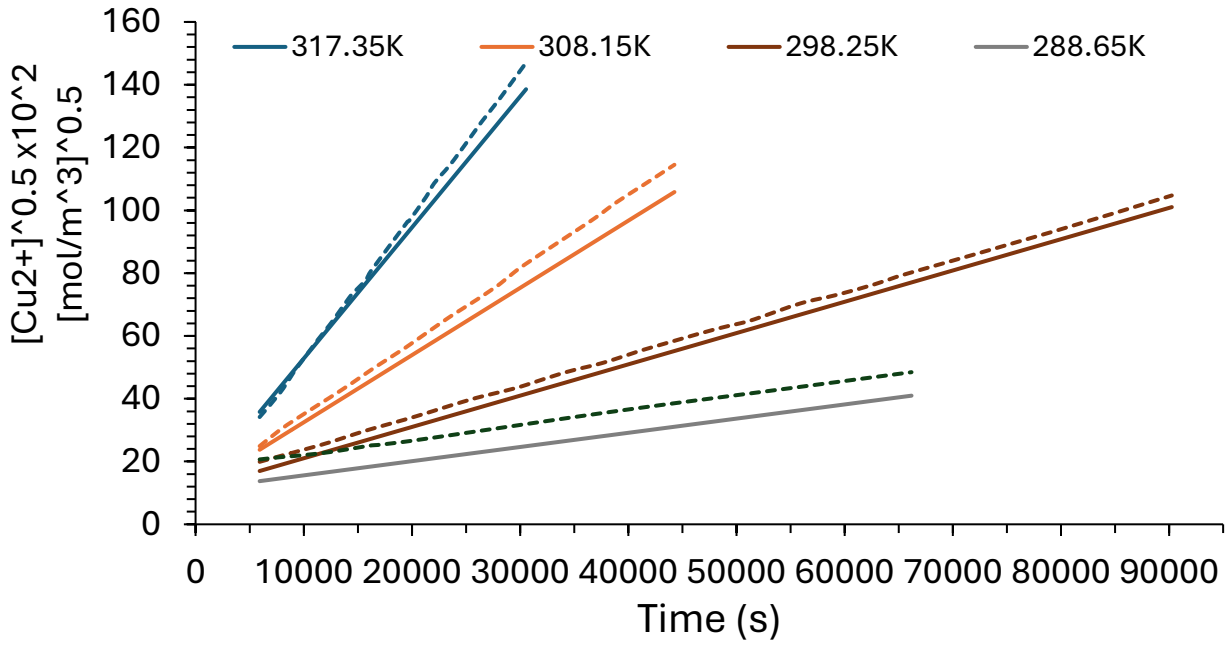

Figure E2: Effect of temperature on $Cu_{(s)}$ dissolution. The square of Cu^{2+} concentration $(mol/m^3)^{0.5}$ $x10^2$ versus time (s) for varying temperatures (K). Solid lines represent kinetic model predictions, dashed lines represent experimental data.

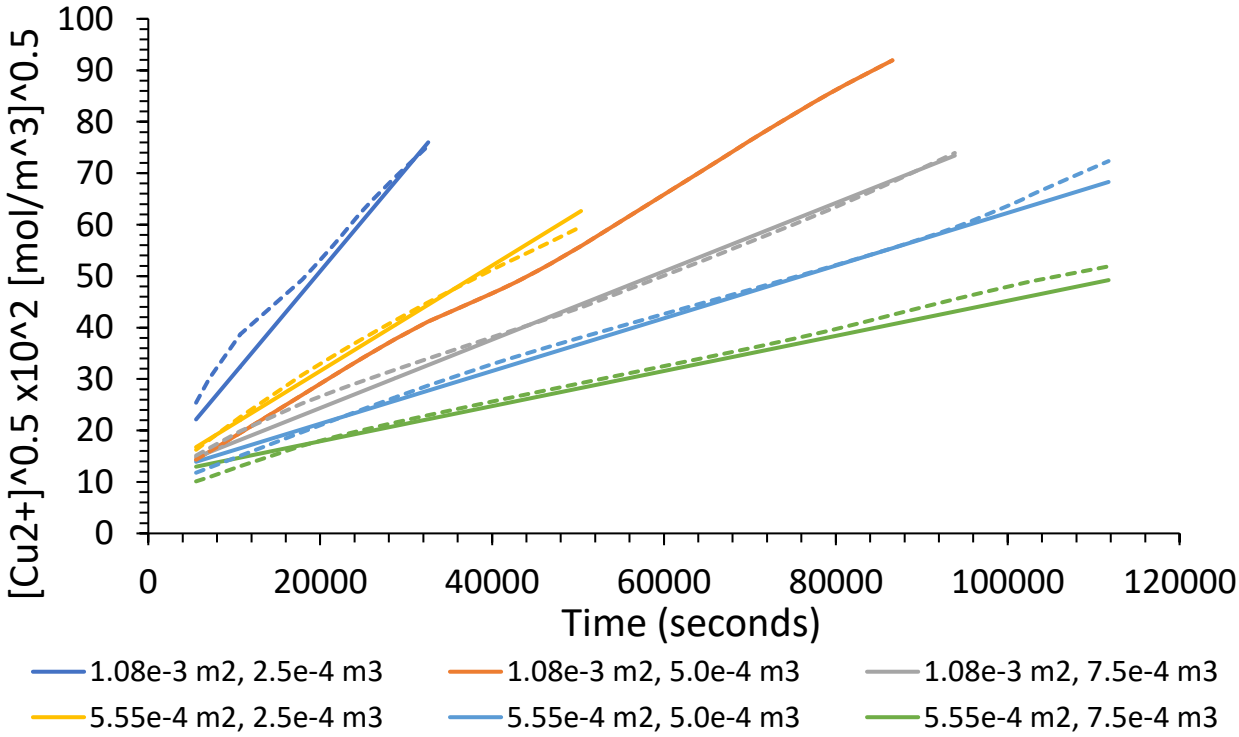

Figure E3: Effect of sample area (m^2) and solution volume (m^3) on $Cu_{(s)}$ dissolution. The square of Cu^{2+} concentration $(mol/m^3)^{0.5}$ $x10^2$ versus time (s). Solid lines represent kinetic model predictions, dashed lines represent experimental data.

Appendix F

Sizing of the copper leaching reactor

Sizing of the copper leaching reactor will be carried out using the kinetics of copper dissolution reported by Lu & Graydon (1953):

$$r_{Cu^{2+}} = \frac{d[Cu^{2+}]}{dt} = 1.36 \times 10^3 e^{-(58994/RT)} (P_{O_2})^{0.5} \left(\frac{A_{Cu}}{V_L}\right) [Cu^{2+}]^{0.5} \qquad \text{Eq F1}$$

To evaluate A_{Cu}, the total surface area of copper in the leaching reactor, the following simplifying assumptions are made:

1) Copper and carbon are present as separate particles in the slurry fed to the leaching reactor.
2) The liquid density stays nearly constant between the inlet and outlet of the reactor.
3) During leaching, each copper particles shrinks but does not completely disappear.
4) Copper particles are spherical, of uniform size, and leach at the same rate.
5) The reactor is well mixed.

The validity of the first assumption depends on the spatial distribution of copper in the solid formed by the wet granulation process and on the particle size reduction in the grinder. The second assumption relies on the leachate solution remaining sufficiently dilute in cupric ions and will be tested in Appendix G. The combination of the second and third assumption implies that the number density of copper particles, n_{Cu}, defined as the number of copper particles per unit volume of liquid, is the same in the inlet, outlet, and interior of the reactor, as shown in Figure F1.

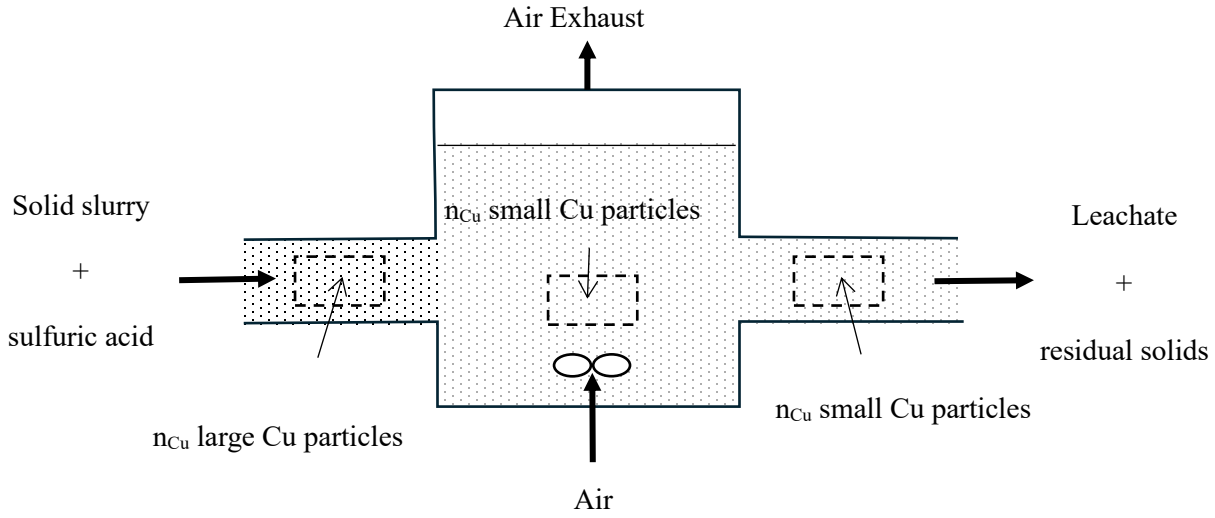

Figure F1: Schematic representation of the leaching vessel

The total number of particles in the reactor, N_{Cu}, is given by:

$$N_{Cu} = n_{Cu} V_L \qquad \text{Eq F2}$$

where V_L (m^3) is the liquid volume in the reactor. Moreover, the surface area of each copper particle in the reactor can be calculated as:

$$a_{Cu} = 4\pi r^2 \qquad \text{Eq F3}$$

where r is the copper particle radius in the reactor. Multiplying Eq. F1 and F2 yields the total surface area of copper in the reactor:

$$A_{Cu} = a_{Cu} N_{Cu} = 4\pi r^2 n_{Cu} V_L \quad \text{Eq F4}$$

The partial dissolution of copper particles can be modelled as a shrinking sphere. Hence, the fractional conversion of solid copper to cupric ions, X_{Cu}, is given by:

$$X_{Cu} = \frac{\frac{4}{3}\pi r_i^3 - \frac{4}{3}\pi r^3}{\frac{4}{3}\pi r_i^3} = \frac{r_i^3 - r^3}{r_i^3} \quad \text{Eq F5}$$

where r_i is the radius of particles at the inlet. Note that the radius of copper particles in the outlet of the reactor is the same as inside the reactor since the reactor is assumed to be well mixed. Eliminating r between Equations F4 and F5 yields:

$$A_{Cu} = 4\pi {r_i}^2 (1 - X_{Cu})^{2/3} n_{Cu} V_L \quad \text{Eq F6}$$

Since the number density of copper particles, n_{Cu}, is the same inside the reactor and at the inlet, it is convenient to evaluate it at the inlet where conditions are known. To this end, consider a volume element in the reactor inlet containing 1 m^3 of liquid and n_{Cu} copper particles (Figure F1). Therefore,

$$n_{Cu} = \frac{m_{Cu,i}}{m_{Cu,i,p}} = \frac{m_{Cu,i}}{\frac{4}{3}\rho_{Cu}\pi r_i^3} \quad \text{Eq F7}$$

where $m_{Cu,i}$ (kg) and $m_{Cu,i,p}$ (kg) are the mass of copper in the volume element and the mass of a copper particle at the inlet, respectively. Moreover, the mass of solids $m_{s,i}$ (kg) in this volume element is:

$$m_{s,i} = \rho_L x_{s,i} \quad \text{Eq F8}$$

where ρ_L is the liquid density (kg/m^3) and $x_{s,i}$ is the solid-to-liquid mass ratio at the inlet. Hence,

$$m_{Cu,i} = y_{Cu,i} m_{s,i} = y_{Cu,i} \rho_L x_{s,i} \quad \text{Eq F9}$$

where $y_{Cu,i}$ is the mass fraction of copper in the inlet solids. Inserting Eq F9 in F7 gives:

$$n_{Cu} = \frac{3}{4}\frac{y_{Cu,i}\rho_L x_{s,i}}{\rho_{Cu}\pi r_i^3} \qquad \text{Eq F10}$$

Next, substitute Eq F10 in F4:

$$A_{Cu} = 3(1 - X_{Cu})^{2/3}\ \frac{y_{Cu,i}\rho_L x_{s,i}}{\rho_{Cu} r_i} V_L \qquad \text{Eq F11}$$

Note that Eq. F11 relates the total surface area of copper in the reactor to the fractional copper conversion and known operating conditions. The concentration of cupric ions in the reactor $[Cu^{2+}]$ can be expressed in a similar manner by performing a material balance between the inlet and outlet of the reactor:

$$F_{Cu^{2+}_{out}} = X_{Cu} F_{Cu,i} \qquad \text{Eq F12}$$

where $F_{Cu,i}$ (mol/s) is the molar flow rate of solid copper entering the reactor. The concentration of cupric ions inside the reactor is the same as in the outlet liquid since the reactor is well mixed, hence:

$$[Cu^{2+}] = [Cu^{2+}]_{out} = \frac{F_{Cu^{2+}_{out}}}{Q_L} = \frac{X_{Cu} F_{Cu,i}}{Q_L} \qquad \text{Eq F13}$$

where Q_L (m^3/s) is the volumetric flow rate of liquid flowing through the reactor. Moreover, the molar flow rate of solid copper entering the reactor is given by:

$$F_{Cu,i} = \frac{m_{Cu,i}}{M_{Cu}} Q_L \qquad \text{Eq F14}$$

where M_{Cu} (0.06355 kg/mol) is the molar weight of copper. Substituting Eq. F9 in F14 yields:

$$F_{Cu,i} = \frac{y_{Cu,i}\rho_L x_{s,i}}{M_{Cu}} Q_L \qquad \text{Eq F15}$$

By combination of Eq. F15 and F13, we can write $[Cu^{2+}]$ as a function of the copper conversion and operating conditions:

$$[Cu^{2+}] = \frac{X_{Cu} y_{Cu,i} \rho_L x_{s,i}}{M_{Cu}} \qquad \text{Eq F16}$$

Next, we insert Eq. G-16 for $[Cu^{2+}]$ and Eq. F11 for A_{Cu} in the rate equation for copper dissolution (Eq. F1) to yield:

$$r_{Cu^{2+}} = \frac{d[Cu^{2+}]}{dt} = 4.08 \times 10^3 e^{-(58994/RT)} \left(\frac{P_{O_2} X_{Cu}}{M_{Cu}}\right)^{\frac{1}{2}} \frac{(1 - X_{Cu})^{\frac{2}{3}} \left(y_{Cu,i} \rho_L x_{s,i}\right)^{\frac{3}{2}}}{\rho_{Cu} r_i} \qquad \text{Eq F17}$$

The volume of liquid in the reactor is obtained from the mole balance on the cupric ions:

$$V_L = \frac{F_{Cu^{2+}_{out}}}{r_{Cu^{2+}}} \qquad \text{Eq F18}$$

Moreover, substitution of Eq. F15 into F12 gives:

$$F_{Cu^{2+}_{out}} = \frac{X_{Cu} y_{Cu,i} \rho_L x_{s,i} Q_L}{M_{Cu}} \qquad \text{Eq F19}$$

Finally, we insert Eq F17 and F19 into F18 to yield:

$$V_L = \frac{2.45 \times 10^{-4} e^{(58994/RT)} \rho_{Cu} r_i Q_L}{(1 - X_{Cu})^{\frac{2}{3}}} \left(\frac{X_{Cu}}{P_{O_2} M_{Cu} y_{Cu,i} \rho_L x_{s,i}}\right)^{\frac{1}{2}} \qquad \text{Eq F20}$$

Eq F20 provides V_L as a function of the liquid flow rate Q_L. Alternatively, an expression of V_L versus the solids mass flow rate $\dot{m}_{s,i}$ (kg/s) entering the reactor can be obtained by writing

$$Q_L = \frac{\dot{m}_{s,i}}{\rho_L x_{s,i}} \qquad \text{Eq F21}$$

and substituting Eq F21 in F20 to give:

$$V_L = \frac{2.45 \times 10^{-4} e^{(58994/RT)} \rho_{Cu} r_i \dot{m}_{s,i}}{(\rho_L x_{s,i})^{\frac{3}{2}} (1 - X_{Cu})^{\frac{2}{3}}} \left(\frac{X_{Cu}}{P_{O_2} M_{Cu} y_{Cu,i}} \right)^{\frac{1}{2}} \quad \text{Eq F22}$$

Moreover,

$$\dot{m}_{s,i} = \frac{\dot{m}_c}{(1 - y_{Cu,i})} \quad \text{Eq F23}$$

Where $\dot{m}_c$ is the mass flow rate of carbon (kg_c/s).

Substitution of Eq F23 in F22 yields:

$$V_L = \frac{2.45 \times 10^{-4} e^{(58994/RT)} \rho_{Cu} r_i \dot{m}_c}{(\rho_L x_{s,i})^{\frac{3}{2}} (1 - X_{Cu})^{\frac{2}{3}} (1 - y_{Cu,i})} \left(\frac{X_{Cu}}{P_{O_2} M_{Cu} y_{Cu,i}} \right)^{\frac{1}{2}} \quad \text{Eq F24}$$

Appendix G

Density and volumetric flow rate of liquid entering and leaving the leaching vessel

One underlying assumption of the leaching vessel model is that the volumetric flow rate of liquid in and out of the vessel remains constant. Similar to the procedure described in Appendix D, Aspen Plus is used to evaluate this assumption. The outlet stream mole flows are calculated based on stoichiometric relationships and a given set of design specifications as summarized in Table G1. Table G2 outlines the Aspen Plus results for the outlet stream, identical to the simulation results in Table D2 of Appendix D. Then, the molar flows of H_2SO_4 and H_2O at the inlet are calculated by:

$$H_2SO_{4,in} = SO^{2-}_{4,comp\ out} = 0.5H^{+}_{comp\ out} + Cu^{2+}_{comp\ out} \quad \text{Eq G1}$$

$$H_2O_{in} = \frac{\dot{m}_{H_2O}}{M_{H_2O}} = \frac{\left(\frac{\dot{m}_s}{x_{s,i}}\right) - \dot{m}_{H_2SO_4}}{M_{H_2O}}$$ Eq G2

where $\dot{m}_{H_2SO_4}$ is the mass flow rate of pure sulfuric acid at the inlet of the reactor and M_{H_2O} is the molar mass of water. The mass flow rate of sulfuric acid at the inlet is calculated by:

$$\dot{m}_{H_2SO_4} = H_2SO_{4,in} * M_{H_2SO_4}$$ Eq G3

where $M_{H_2SO_4}$ is the molar mass of sulfuric acid.

The inlet and outlet streams are modeled in Aspen Plus so that the volumetric flow rates and mass densities can be compared. The inlet stream results are summarized in Table G3. The results in Table G1 show a slight increase in the volumetric flow rate, from 29.34 m^3/h to 30.44 m^3/h at the outlet due to the increase in mass density from 1049.46 kg/m^3 to 1092.85 kg/m^3. Although the discrepancy is significant, the model can be used for preliminary design estimates because the degree of uncertainty is matched by other estimations needed to develop the overall carbon purification process.

Table G1: Design Specifications

Design Specifications	**Symbol**	**Units**	**Inlet Stream**
Temperature	T	°C	100
Pressure	P	kPa	101.325
Mass flow rate of carbon	$\dot{m}_C$	kg_C/s	0.735
Mass fraction of copper in solids at the inlet	$y_{Cu,i}$	kg_{Cu}/kg_{Solid}	0.427
Mass flow rate of solids at the inlet	$\dot{m}_{S,i}$	kg_{Solid}/s	1.283
Ratio of solid to liquid in feed slurry	$x_{s,i}$	kg_{Solid}/kg_{Liquid}	0.15
Mass flow rate of liquid at the inlet	$\dot{m}_L$	kg_{Liquid}/s	8.55
Radius of particles in feed	r_i	m	$2.5x10^{-5}$
Fractional Conversion of copper	X_{Cu}	-	0.998

Table G2: Outlet Stream Results

Liquid Phase Mole Flows		**Units**	**Outlet Stream**
H_2O		mol/s	372.7
$CuSO_4$		mol/s	0
H_2SO_4		mol/s	$9.85x10^{-8}$
Cu^{2+}		mol/s	8.60
H^+		mol/s	2.03
OH^-		mol/s	$5.55x10^{-11}$
HSO_4^-		mol/s	14.17
SO_4^{2-}		mol/s	2.53
Results		**Units**	**Outlet Stream**
Volumetric Flow Rate	Q	m^3/h	30.44
Mass density	ρ	kg/m^3	1092.85
pH			1.00

Table G3: Inlet Stream Results

Liquid Phase Mole Flows		**Units**	**Inlet Stream**
H_2O		mol/s	383.84
$CuSO_4$		mol/s	0
H_2SO_4		mol/s	$2.13x10^{-6}$
Cu^{2+}		mol/s	0
HSO_4^-		mol/s	16.50
SO_4^{2-}		mol/s	0.202
Results		**Units**	**Inlet Stream**
Volumetric Flow Rate	Q	m^3/h	29.34
Mass density	ρ	kg/m^3	1049.46
pH			-0.1724

Appendix H

Cementation Reactor

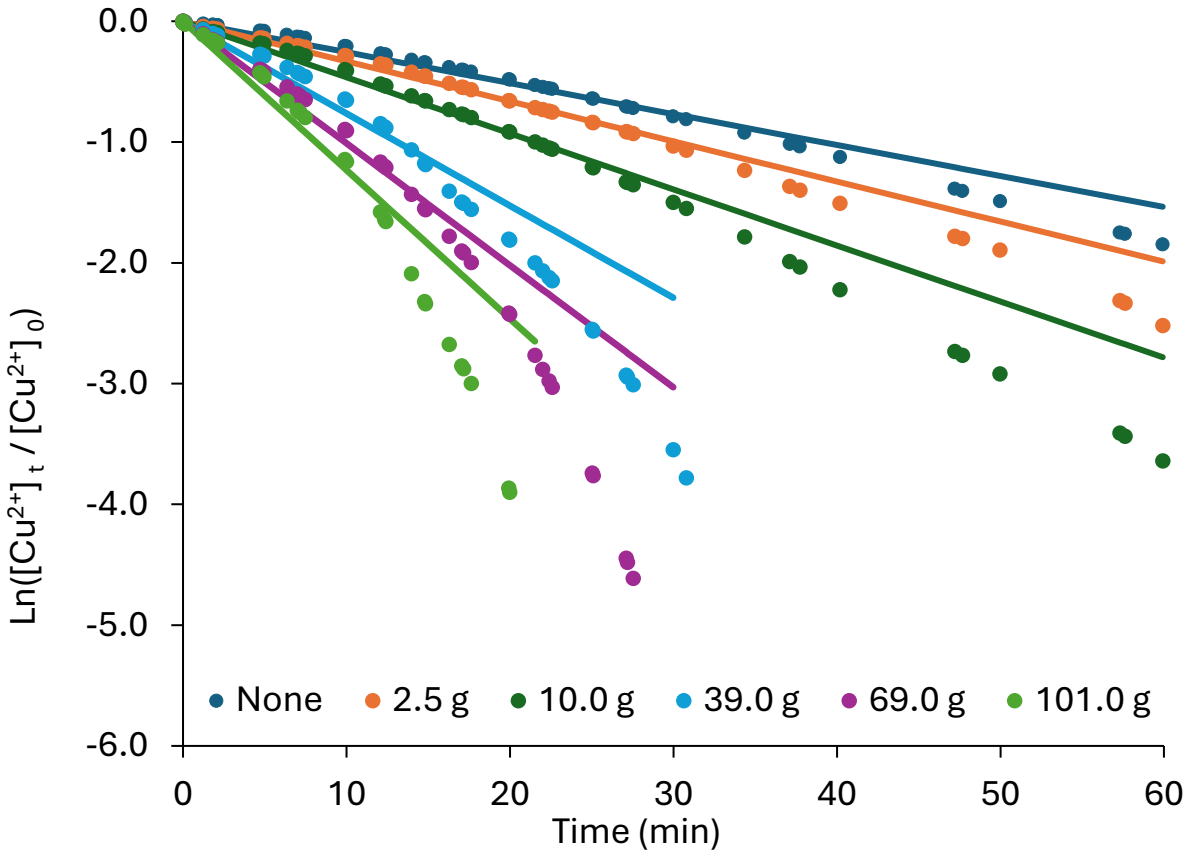

Figure H1: Ln($[Cu^{2+}]_t/[Cu^{2+}]_0$) versus time for different initial concentrations of copper metal. Experimental data points from Dean and Groves and lines from Equation 57 model.

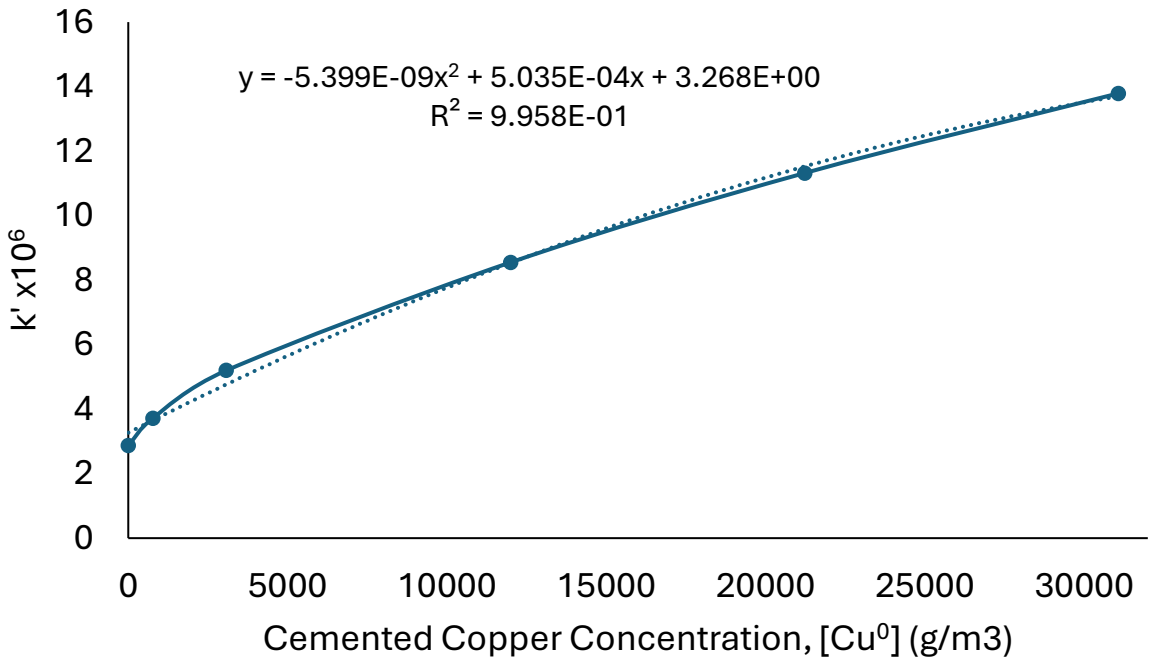

Figure H2: Apparent rate constant (k' x10^6) calculated for each experiment of Dean and Groves versus the cemented copper concentration [Cu^0]

Appendix I

	Units	1	2	3	4	5	6	7	8	9	10
Temperature	**C**	28.2	90.0	80.0	2.7	4.5	4.5	14.9	7.1	13.4	13.4
Pressure	**bar**	1.0	1.0	1.0	3.0	2.0	2.0	1.5	1.5	1.0	5.0
Mass Liquid Fraction		0.8796	0.8281	0.9300	0.9300	1.0000	0.7497	1.0000	1.0000	0.9488	0.9488
Mass Solid Fraction		0.1204	0.0650	0.0700	0.0700	0.0000	0.2503	0.0000	0.0000	0.0512	0.0512
Mole Flows	**kmol/hr**	**1940.3**	**1983.7**	**1858.5**	**1870.0**	**1271.7**	**597.9**	**322.3**	**1687.3**	**1716.4**	**1716.4**
Mole Fractions											
H_2O		0.8033	0.8015	0.8251	0.8200	0.9296	0.5874	0.9301	0.9325	0.9167	0.9167
Cu		0.0162	0.0000	0.0000	0.0000	0.0000	0.0001	0.0000	0.0000	0.0179	0.0179
H_2SO_4		0.0000	0.0000	0.0000	0.0000	0.0000	0.0000	0.0000	0.0000	0.0000	0.0000
O_2		0.0000	0.0012	0.0000	0.0000	0.0000	0.0000	0.0000	0.0000	0.0000	0.0000
H^+		0.0339	0.0039	0.0048	0.0109	0.0124	0.0071	0.0111	0.0118	0.0107	0.0107
OH^-		0.0000	0.0000	0.0000	0.0000	0.0000	0.0000	0.0000	0.0000	0.0000	0.0000
HSO_4^-		0.0301	0.0270	0.0282	0.0219	0.0256	0.0147	0.0268	0.0245	0.0250	0.0250
SO_4^{--}		0.0019	0.0043	0.0052	0.0113	0.0128	0.0074	0.0116	0.0122	0.0111	0.0111
Cu^{2+}		0.0000	0.0158	0.0169	0.0168	0.0194	0.0112	0.0194	0.0186	0.0004	0.0004
C		0.1146	0.1121	0.1197	0.1189	0.0000	0.3719	0.0000	0.0000	0.0000	0.0000
Fe		0.0000	0.0000	0.0000	0.0000	0.0000	0.0000	0.0000	0.0000	0.0000	0.0000
Fe^{2+}		0.0000	0.0000	0.0000	0.0000	0.0000	0.0000	0.0000	0.0000	0.0179	0.0179
$FEOH^+$		0.0000	0.0000	0.0000	0.0000	0.0000	0.0000	0.0000	0.0000	0.0000	0.0000
AIR		0.0000	0.0000	0.0000	0.0000	0.0000	0.0000	0.0008	0.0003	0.0003	0.0003
Bi		0.0000	0.0000	0.0000	0.0000	0.0000	0.0001	0.0000	0.0000	0.0000	0.0000
N_2		0.0000	0.0341	0.0002	0.0002	0.0002	0.0001	0.0001	0.0002	0.0002	0.0002
Mass Flows	**kg/hr**	**38840.4**	**41312.8**	**38330.6**	**38330.6**	**27611.1**	**10719.5**	**7009.0**	**36367.0**	**38081.0**	**38081.0**
Mass Fractions											
H_2O		0.7230	0.6934	0.7207	0.7207	0.7713	0.5903	0.7705	0.7794	0.7443	0.7443
Cu		0.0514	0.0001	0.0001	0.0001	0.0000	0.0004	0.0000	0.0000	0.0512	0.0512
H_2SO_4		0.0000	0.0000	0.0000	0.0000	0.0000	0.0000	0.0000	0.0000	0.0000	0.0000
O_2		0.0000	0.0018	0.0000	0.0000	0.0000	0.0000	0.0000	0.0000	0.0000	0.0000
H^+		0.0017	0.0002	0.0002	0.0005	0.0006	0.0004	0.0005	0.0006	0.0005	0.0005
OH^-		0.0000	0.0000	0.0000	0.0000	0.0000	0.0000	0.0000	0.0000	0.0000	0.0000
HSO_4^-		0.1458	0.1258	0.1329	0.1038	0.1143	0.0797	0.1198	0.1103	0.1094	0.1094
SO_4^{--}		0.0091	0.0197	0.0240	0.0528	0.0567	0.0395	0.0512	0.0544	0.0479	0.0479
Cu^{2+}		0.0000	0.0482	0.0520	0.0520	0.0568	0.0396	0.0568	0.0547	0.0010	0.0010
C		0.0688	0.0647	0.0697	0.0697	0.0000	0.2492	0.0000	0.0000	0.0000	0.0000
Fe		0.0000	0.0000	0.0000	0.0000	0.0000	0.0000	0.0000	0.0000	0.0000	0.0000
Fe^{2+}		0.0000	0.0000	0.0000	0.0000	0.0000	0.0000	0.0000	0.0000	0.0450	0.0450
$FEOH^+$		0.0000	0.0000	0.0000	0.0000	0.0000	0.0000	0.0000	0.0000	0.0000	0.0000
AIR		0.0000	0.0000	0.0000	0.0000	0.0000	0.0000	0.0011	0.0004	0.0004	0.0004
Bi		0.0002	0.0002	0.0002	0.0002	0.0000	0.0008	0.0000	0.0000	0.0000	0.0000
N_2		0.0000	0.0459	0.0002	0.0002	0.0002	0.0002	0.0002	0.0002	0.0002	0.0002

	Units	11	12	DRYAIR	DRYC	FE	FILTRAT2	GASI2	GASIN	GASO2	GASOUT
Temperature	**C**	13.5	13.5	250.0	90.2	25.0	14.9	25.0	25.0	25.0	25.0
Pressure	**bar**	2.0	2.0	1.0	1.0	1.0	1.5	1.0	1.5	0.5	0.9
Mass Liquid Fraction		1.0000	0.6667	0.0000	0.0180	0.0000	1.0000	0.0000	0.0000	0.0000	0.0001
Mass Solid Fraction		0.0000	0.3333	0.0000	0.9820	1.0000	0.0000	0.0000	0.0000	0.0000	0.0000
Mole Flows	**kmol/hr**	**1503.7**	**212.7**	**570.6**	**224.6**	**30.7**	**179.3**	**209.5**	**344.5**	**212.0**	**348.9**
Mole Fractions											
H_2O		0.9334	0.7987	0.0032	0.0086	0.0000	0.9331	0.0000	0.0000	0.0120	0.0144
Cu		0.0000	0.1443	0.0000	0.0003	0.0000	0.0000	0.0000	0.0000	0.0000	0.0000
H_2SO_4		0.0000	0.0000	0.0000	0.0000	0.0000	0.0000	0.0000	0.0000	0.0000	0.0000
O_2		0.0000	0.0000	0.0000	0.0000	0.0000	0.0000	0.0000	0.0000	0.0000	0.0000
H^+		0.0108	0.0093	0.0000	0.0000	0.0000	0.0107	0.0000	0.0000	0.0000	0.0000
OH^-		0.0000	0.0000	0.0000	0.0000	0.0000	0.0000	0.0000	0.0000	0.0000	0.0000
HSO_4^-		0.0255	0.0218	0.0000	0.0005	0.0000	0.0258	0.0000	0.0000	0.0000	0.0000
SO_4^{--}		0.0113	0.0096	0.0000	0.0000	0.0000	0.0111	0.0000	0.0000	0.0000	0.0000
Cu^{2+}		0.0004	0.0003	0.0000	0.0002	0.0000	0.0004	0.0000	0.0000	0.0000	0.0000
C		0.0000	0.0000	0.0000	0.9902	0.0000	0.0000	0.0000	0.0000	0.0000	0.0000
Fe		0.0000	0.0001	0.0000	0.0000	1.0000	0.0000	0.0000	0.0000	0.0000	0.0000
Fe^{2+}		0.0182	0.0156	0.0000	0.0000	0.0000	0.0183	0.0000	0.0000	0.0000	0.0000
$FEOH^+$		0.0000	0.0000	0.0000	0.0000	0.0000	0.0000	0.0000	0.0000	0.0000	0.0000
AIR		0.0003	0.0003	0.9968	0.0000	0.0000	0.0005	1.0000	1.0000	0.9880	0.9855
Bi		0.0000	0.0000	0.0000	0.0002	0.0000	0.0000	0.0000	0.0000	0.0000	0.0000
N_2		0.0002	0.0001	0.0000	0.0000	0.0000	0.0002	0.0000	0.0000	0.0000	0.0000
Mass Flows	**kg/hr**	**32230.4**	**5850.6**	**16500.0**	**2732.9**	**1714.0**	**3847.9**	**6066.4**	**9973.7**	**6110.7**	**10047.1**
Mass Fractions											
H_2O		0.7845	0.5230	0.0020	0.0128	0.0000	0.7835	0.0000	0.0000	0.0075	0.0090
Cu		0.0000	0.3332	0.0000	0.0015	0.0000	0.0000	0.0000	0.0000	0.0000	0.0000
H_2SO_4		0.0000	0.0000	0.0000	0.0000	0.0000	0.0000	0.0000	0.0000	0.0000	0.0000
O_2		0.0000	0.0000	0.0000	0.0000	0.0000	0.0000	0.0000	0.0000	0.0000	0.0000
H^+		0.0005	0.0003	0.0000	0.0000	0.0000	0.0005	0.0000	0.0000	0.0000	0.0000
OH^-		0.0000	0.0000	0.0000	0.0000	0.0000	0.0000	0.0000	0.0000	0.0000	0.0000
HSO_4^-		0.1154	0.0769	0.0000	0.0040	0.0000	0.1166	0.0000	0.0000	0.0000	0.0000
SO_4^{--}		0.0504	0.0336	0.0000	0.0000	0.0000	0.0498	0.0000	0.0000	0.0000	0.0000
Cu^{2+}		0.0011	0.0007	0.0000	0.0013	0.0000	0.0011	0.0000	0.0000	0.0000	0.0000
C		0.0000	0.0000	0.0000	0.9773	0.0000	0.0000	0.0000	0.0000	0.0000	0.0000
Fe		0.0000	0.0001	0.0000	0.0000	1.0000	0.0000	0.0000	0.0000	0.0000	0.0000
Fe^{2+}		0.0474	0.0316	0.0000	0.0000	0.0000	0.0476	0.0000	0.0000	0.0000	0.0000
$FEOH^+$		0.0000	0.0000	0.0000	0.0000	0.0000	0.0000	0.0000	0.0000	0.0000	0.0000
AIR		0.0004	0.0003	0.9980	0.0000	0.0000	0.0006	1.0000	1.0000	0.9925	0.9909
Bi		0.0000	0.0000	0.0000	0.0031	0.0000	0.0000	0.0000	0.0000	0.0000	0.0000
N_2		0.0002	0.0001	0.0000	0.0000	0.0000	0.0002	0.0000	0.0000	0.0000	0.0000

	Units	H2O	H2SO4	N2	O2	SOLIDS	VENTGAS	WASH1	WASH2	WASHO2	WASHOUT
Temperature	C	25.0	25.0	25.0	25.0	80.0	80.0	25.0	25.0	14.9	14.9
Pressure	bar	1.0	1.0	1.0	1.0	1.0	1.0	6.1	6.0	5.5	5.8
Mass Liquid Fraction		1.0000	1.0000	0.0000	0.0000	0.0000	0.0000	1.0000	1.0000	1.0000	1.0000
Mass Solid Fraction		0.0000	0.0000	0.0000	0.0000	1.0000	0.0000	0.0000	0.0000	0.0000	0.0000
Mole Flows	**kmol/hr**	**1558.7**	**124.1**	**67.7**	**18.0**	**253.8**	**126.3**	**95.9**	**22.0**	**20.3**	**93.1**
Mole Fractions											
H_2O		1.0000	0.0000	0.0000	0.0000	0.0000	0.4480	1.0000	1.0000	0.9927	0.9824
Cu		0.0000	0.0000	0.0000	0.0000	0.1238	0.0000	0.0000	0.0000	0.0000	0.0000
H_2SO_4		0.0000	0.0000	0.0000	0.0000	0.0000	0.0000	0.0000	0.0000	0.0000	0.0000
O_2		0.0000	0.0000	0.0000	1.0000	0.0000	0.0183	0.0000	0.0000	0.0000	0.0000
H^+		0.0000	0.5002	0.0000	0.0000	0.0000	0.0000	0.0000	0.0000	0.0014	0.0031
OH^-		0.0000	0.0000	0.0000	0.0000	0.0000	0.0000	0.0000	0.0000	0.0000	0.0000
HSO_4^-		0.0000	0.4993	0.0000	0.0000	0.0000	0.0000	0.0000	0.0000	0.0016	0.0044
SO_4^{--}		0.0000	0.0005	0.0000	0.0000	0.0000	0.0000	0.0000	0.0000	0.0015	0.0032
Cu^{2+}		0.0000	0.0000	0.0000	0.0000	0.0000	0.0000	0.0000	0.0000	0.0000	0.0038
C		0.0000	0.0000	0.0000	0.0000	0.8760	0.0000	0.0000	0.0000	0.0000	0.0000
Fe		0.0000	0.0000	0.0000	0.0000	0.0000	0.0000	0.0000	0.0000	0.0000	0.0000
Fe^{2+}		0.0000	0.0000	0.0000	0.0000	0.0000	0.0000	0.0000	0.0000	0.0015	0.0000
$FEOH^+$		0.0000	0.0000	0.0000	0.0000	0.0000	0.0000	0.0000	0.0000	0.0000	0.0000
AIR		0.0000	0.0000	0.0000	0.0000	0.0000	0.0000	0.0000	0.0000	0.0012	0.0031
Bi		0.0000	0.0000	0.0000	0.0000	0.0002	0.0000	0.0000	0.0000	0.0000	0.0000
N_2		0.0000	0.0000	1.0000	0.0000	0.0000	0.5336	0.0000	0.0000	0.0000	0.0000
Mass Flows	**kg/hr**	**28080.0**	**6084.0**	**1896.5**	**576.0**	**4676.4**	**2982.2**	**1728.0**	**396.0**	**372.2**	**1746.9**
Mass Fractions											
H_2O		1.0000	0.0000	0.0000	0.0000	0.0000	0.3419	1.0000	1.0000	0.9772	0.9430
Cu		0.0000	0.0000	0.0000	0.0000	0.4271	0.0000	0.0000	0.0000	0.0000	0.0000
H_2SO_4		0.0000	0.0000	0.0000	0.0000	0.0000	0.0000	0.0000	0.0000	0.0000	0.0000
O_2		0.0000	0.0000	0.0000	1.0000	0.0000	0.0249	0.0000	0.0000	0.0000	0.0000
H^+		0.0000	0.0103	0.0000	0.0000	0.0000	0.0000	0.0000	0.0000	0.0001	0.0002
OH^-		0.0000	0.0000	0.0000	0.0000	0.0000	0.0000	0.0000	0.0000	0.0000	0.0000
HSO_4^-		0.0000	0.9888	0.0000	0.0000	0.0000	0.0000	0.0000	0.0000	0.0083	0.0229
SO_4^{--}		0.0000	0.0010	0.0000	0.0000	0.0000	0.0000	0.0000	0.0000	0.0078	0.0162
Cu^{2+}		0.0000	0.0000	0.0000	0.0000	0.0000	0.0000	0.0000	0.0000	0.0001	0.0130
C		0.0000	0.0000	0.0000	0.0000	0.5711	0.0000	0.0000	0.0000	0.0000	0.0000
Fe		0.0000	0.0000	0.0000	0.0000	0.0000	0.0000	0.0000	0.0000	0.0000	0.0000
Fe^{2+}		0.0000	0.0000	0.0000	0.0000	0.0000	0.0000	0.0000	0.0000	0.0046	0.0000
$FEOH^+$		0.0000	0.0000	0.0000	0.0000	0.0000	0.0000	0.0000	0.0000	0.0000	0.0000
AIR		0.0000	0.0000	0.0000	0.0000	0.0000	0.0000	0.0000	0.0000	0.0020	0.0047
Bi		0.0000	0.0000	0.0000	0.0000	0.0018	0.0000	0.0000	0.0000	0.0000	0.0000
N_2		0.0000	0.0000	1.0000	0.0000	0.0000	0.6332	0.0000	0.0000	0.0000	0.0000

	Units	WASTEWAT	WETAIR	WETC	WETCU+FE
Temperature	**C**	13.7	103.6	14.9	14.9
Pressure	**bar**	1.5	1.0	1.0	1.0
Mass Liquid Fraction		1.0000	0.0000	0.2584	0.0161
Mass Solid Fraction		0.0000	0.0000	0.7416	0.9839
Mole Flows	**kmol/hr**	**1703.5**	**619.7**	**273.7**	**32.5**
Mole Fractions					
H_2O		0.9340	0.0820	0.1861	0.0540
Cu		0.0000	0.0000	0.0002	0.9454
H_2SO_4		0.0000	0.0000	0.0000	0.0000
O_2		0.0000	0.0000	0.0000	0.0000
H^+		0.0107	0.0000	0.0002	0.0000
OH^-		0.0000	0.0000	0.0000	0.0000
HSO_4^-		0.0252	0.0000	0.0002	0.0000
SO_4^{--}		0.0112	0.0000	0.0002	0.0000
Cu^{2+}		0.0004	0.0000	0.0002	0.0000
C		0.0000	0.0000	0.8124	0.0000
Fe		0.0000	0.0000	0.0000	0.0004
Fe^{2+}		0.0180	0.0000	0.0000	0.0000
$FEOH^+$		0.0000	0.0000	0.0000	0.0000
AIR		0.0003	0.9180	0.0003	0.0001
Bi		0.0000	0.0000	0.0001	0.0000
N_2		0.0002	0.0000	0.0000	0.0000
Mass Flows	**kg/hr**	**36450.5**	**17385.4**	**3618.3**	**1982.1**
Mass Fractions					
H_2O		0.7864	0.0527	0.2537	0.0159
Cu		0.0000	0.0000	0.0011	0.9835
H_2SO_4		0.0000	0.0000	0.0000	0.0000
O_2		0.0000	0.0000	0.0000	0.0000
H^+		0.0005	0.0000	0.0000	0.0000
OH^-		0.0000	0.0000	0.0000	0.0000
HSO_4^-		0.1143	0.0000	0.0017	0.0000
SO_4^{--}		0.0501	0.0000	0.0013	0.0001
Cu^{2+}		0.0011	0.0000	0.0010	0.0000
C		0.0000	0.0000	0.7382	0.0000
Fe		0.0000	0.0000	0.0000	0.0003
Fe^{2+}		0.0470	0.0000	0.0000	0.0000
$FEOH^+$		0.0000	0.0000	0.0000	0.0000
AIR		0.0005	0.9473	0.0007	0.0001
Bi		0.0000	0.0000	0.0023	0.0000
N_2		0.0002	0.0000	0.0000	0.0000